

AD-A164 271

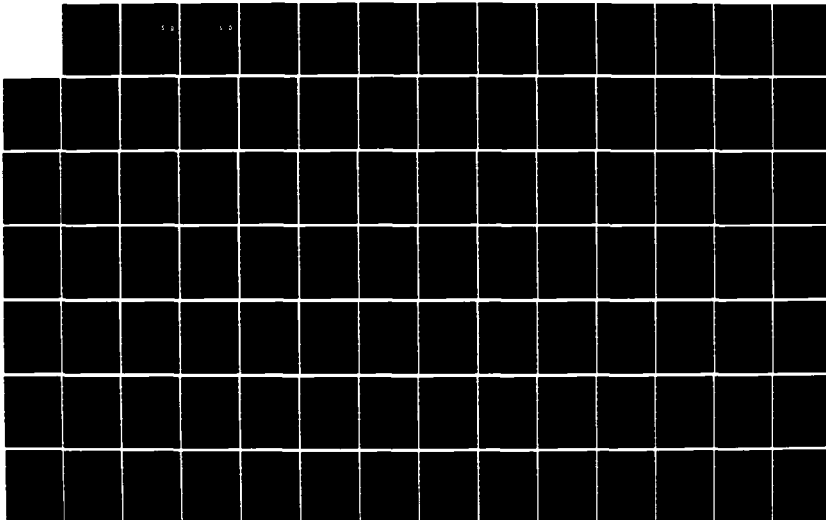
DETECTION OF ATMOSPHERIC CARBON MONOXIDE FROM A
SHUTTLE-BORNE LIDAR(U) AIR FORCE INST OF TECH
WRIGHT-PATTERSON AFB OH SCHOOL OF ENGINEERING
M R HERTEL DEC 83 AFIT/GEP/PH-83D-4

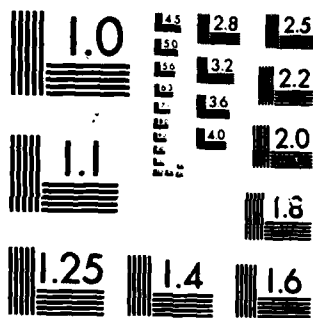
1/2

UNCLASSIFIED

F/G 4/1

NL

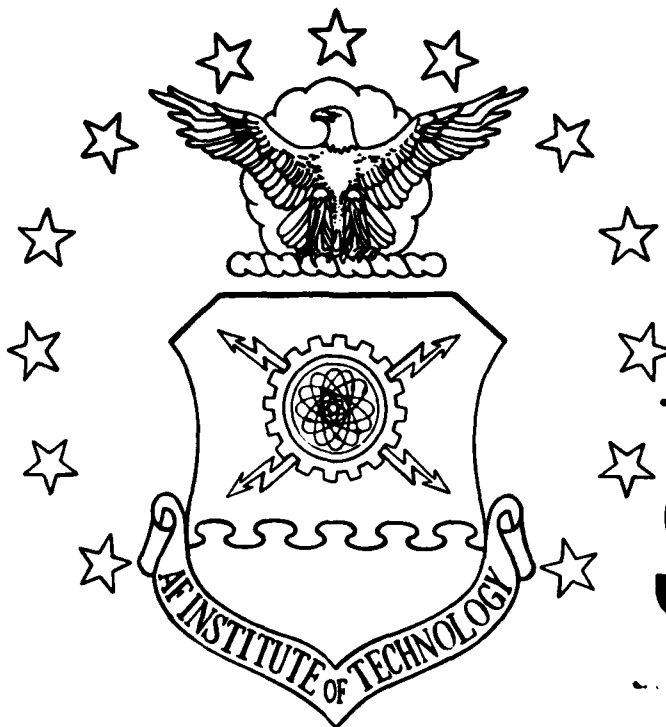




MICROCOPY RESOLUTION TEST CHART
NATIONAL BUREAU OF STANDARDS-1963-A

AD-A164 271

DTIC FILE COPY



DTIC
ELECTE
FEB 14 1986
S D

DETECTION OF ATMOSPHERIC
CARBON MONOXIDE FROM A
SHUTTLE-BORNE LIDAR

THESIS

AFIT/GEP/PH-83D-4 Wesley R. Hertel
Civ. GS-12

DISTRIBUTION STATEMENT A

Approved for public release;
Distribution Unlimited

DEPARTMENT OF THE AIR FORCE
AIR UNIVERSITY

AIR FORCE INSTITUTE OF TECHNOLOGY

Wright-Patterson Air Force Base, Ohio

86 2 14 016

1

DTIC
ELECTE
FEB 14 1986
S D D

DETECTION OF ATMOSPHERIC
CARBON MONOXIDE FROM A
SHUTTLE-BORNE LIDAR

THESIS

AFIT/GEP/PH-83D-4 Wesley R. Hertel
Civ. GS-12

DISTRIBUTION STATEMENT A

Approved for public release;
Distribution Unlimited

DETECTION OF ATMOSPHERIC
CARBON MONOXIDE FROM A
SHUTTLE-BORNE LIDAR

THESIS

Presented to the Faculty of the School of Engineering
of the Air Force Institute of Technology

Air University

in Partial Fulfillment of the
Requirements for the Degree of
Master of Science

by

Wesley R. Hertel, B.S.
Civ. GS-12

Graduate Physics

December 1983

| | |
|--------------------|--|
| Accession For | |
| NTIS CRA&I | <input checked="checked" type="checkbox"/> |
| DTIC TAB | <input type="checkbox"/> |
| Unannounced | <input type="checkbox"/> |
| Justification | |
| By | |
| Distribution | |
| Availability Codes | |
| Dist | Avail and/or Special |
| A-1 | |

Approved for public release; distribution unlimited



PREFACE

This thesis is concerned with the detection of carbon monoxide in the atmosphere at various altitudes and temperatures from a shuttle-borne differential absorption lidar. It parallels an earlier study by Robert H. Wank, which focused on carbon dioxide, and is intended to be a companion volume to his study.

I would like to thank my advisor, Maj. James J. Lange, for his guidance and help in the completion of this thesis. I would also like to thank Dr. W.B. Roh and Dr. E.A. Dorko for their input in resolving various difficulties encountered along the way. Also, a note of thanks is in order for my sponsoring organization, Foreign Technology Division, to whom I am grateful for the opportunity to complete my degree program.

Finally, a very special thanks to my lovely wife, Maggie, whose encouragement and interest are a continuing source of pleasure and motivation for me.

Contents

| | Page |
|--|------|
| Preface | 11 |
| List of Figures | vi |
| List of Tables | vii |
| Abstract | viii |
| I. Introduction | 1 |
| Problem | 3 |
| General Approach | 3 |
| Assumptions | 4 |
| II. Lidar Detection of Carbon Monoxide | 5 |
| System Definition | 7 |
| The Lidar Equation | 12 |
| III. Molecular Structure of Carbon Monoxide | 17 |
| Distribution of CO Molecules in Vibrational States | 18 |
| Absorption Line Positions for the CO 1-0 Band | 19 |
| Calculation of Line-Strength for the CO 1-0 Band | 20 |
| IV. Atmospheric Transmission | 25 |
| Atmosphere Model | 28 |
| Absorption and Scattering in the Atmosphere | 30 |
| Rayleigh Scattering Extinction Coefficient | 32 |
| Rayleigh Volumetric Backscattering Coefficient | 33 |
| Aerosol Extinction Coefficients | 34 |
| Aerosol Volumetric Backscattering Coefficient | 36 |

| | Page |
|--|------|
| Molecular Extinction Coefficients | 36 |
| Extinction Coefficients for CO | 39 |
| CO ₂ Absorption Near 2154 cm ⁻¹ | 40 |
| N ₂ O Absorption Near 2154 cm ⁻¹ | 41 |
| Ozone Absorption Near 2154 cm ⁻¹ | 41 |
| Extinction Coefficients for Water-Vapor | 42 |
| Calculation of T_A^4 | 43 |
| Calculation of T_{co}^2 | 44 |
| V. Minimum Signal-to-Noise Requirements | 52 |
| VI. Detection of Lidar Return Signal | 57 |
| Direct Detection | 58 |
| Background Noise Power | 60 |
| Noise Equivalent Power | 63 |
| Required Laser Power | 66 |
| Heterodyne Detection | 68 |
| Noise Equivalent Power | 71 |
| Heterodyne Signal-to-Noise Considerations | 73 |
| Required Laser Power | 75 |
| Error Analysis | 76 |
| VII. Performance Analysis / 1 Joule Laser with Heterodyne Detection | 81 |
| Return Signal Power | 82 |
| Signal-to-Noise Ratio / Multiple Shots | 82 |
| Performance Envelope | 84 |

| | Page |
|--|------|
| Detection of "Hot" CO | 88 |
| VIII. Conclusions and Recommendations | 94 |
| Conclusions | 94 |
| Recommendations | 95 |
| Bibliography | 96 |
| Appendix A: CO Line Positions and Line-Strengths | 100 |
| Appendix B: Atmospheric Parameters | 103 |
| Appendix C: Aerosol Extinction Coefficients for Clear Atmosphere | 105 |
| Appendix D: Rayleigh Atmospheric Extinction Coefficient . . . | 107 |
| Appendix E: Volumetric Scattering Coefficients | 108 |
| Appendix F: Absorption Cross-Section of CO Lines at Sea-Level | 110 |
| Appendix G: Absorption Cross-Section and Atmospheric Extinction Coefficient of CO | 112 |
| Appendix H: Absorption Cross-Section of Water-Vapor at Sea-Level | 114 |
| Appendix I: Atmospheric Extinction Coefficient of Water-Vapor | 117 |
| Appendix J: Atmospheric Transmission at 2154.6050 cm^{-1} . . . | 119 |
| Appendix K: Absorption Cross-Section of CO R(2) Line at 2154.6050 cm^{-1} | 121 |
| Appendix L: Atmospheric Transmission at 2154.6050 cm^{-1} Due to R(2) Line of CO | 123 |
| Appendix M: Atmospheric Transmission Averaged Over the Laser Line-Width | 125 |
| Vita | 127 |

List of Figures

| Figure | Page |
|--|------|
| 1. DIAL Lidar System Block Diagram | 11 |
| 2. Atmospheric Transmission Averaged Over Laser Line-Width at Sea Level | 50 |
| 3. Atmospheric Transmission Averaged Over Laser Line-Width at 30 km | 51 |
| 4. Minimum Signal-to-Noise Ratio Required | 55 |
| 5. Laser Power Required - Direct Detection | 67 |
| 6. The Heterodyne Process | 69 |
| 7. Laser Power Required - Heterodyne Detection | 77 |
| 8. Return Signal Power - 1 Joule System | 83 |
| 9. Measurement Error - 1 Joule System / 100 Shots | 85 |
| 10. Performance Envelope - 1 Joule System | 89 |

List of Tables

| Table | Page |
|--|------|
| I. Lidar System Parameters | 10 |
| II. Molecular Constants for $^{12}\text{C}^{16}\text{O}$ | 17 |
| III. Dunham Coefficients for CO | 21 |
| IV. InSb ISC-368 Infrared Detector | 58 |
| V. Lidar System Parameters | 81 |
| VI. Heterodyne Detection of "Hot" CO | 93 |

Abstract

Remote sensing of carbon monoxide from a shuttle-borne differential absorption lidar (DIAL) was investigated. The primary lidar wavelength is in the infrared at 4.64μ and takes advantage of a spectral coincidence between the R(2) line in the fundamental absorption band of CO and the frequency-doubled R(18) emission line of the CO₂ laser. Extinction coefficients for CO, H₂O, Rayleigh, and Mie scattering were determined in order to compute the return signal strength from various altitudes. Direct detection was found to be unsatisfactory, but heterodyne detection was found to be suitable if shot-averaging is used. With heterodyne detection the system was determined to be capable of making accurate measurements of CO in the troposphere, but performance in the stratosphere was found to be marginal.

DETECTION OF ATMOSPHERIC CARBON MONOXIDE FROM A SHUTTLE-BORNE LIDAR

I. Introduction

A shuttle-based lidar system offers unique advantages. From its vantage point in orbit, the system would have access to a large percentage of the earth's atmosphere and be able to make global measurements with a spatial resolution and sensitivity that could be equalled only by a large network of stations on the ground or an extensive airborne program. In recognition of this fact, the National Aeronautics and Space Administration (NASA) produced in 1973 a report detailing shuttle payload requirements for AMPS (Atmospherics, Magnetospherics, and Plasmas in Space), a scientific payload to be flown in conjunction with the European Spacelab. Included in this study was the scientific rationale for a spaceborne atmospheric lidar.

In 1977, the NASA Atmospheric Lidar Working Group was convened. One of the purposes of the group was to assist NASA in defining a program that would eventually lead to the development of the necessary flight systems (Ref 1). Also in 1977, the European Space Agency released a report detailing the technical aspects of a multidisciplinary lidar system suitable for shuttle flight in the Spacelab payload (Ref 2). This report was used extensively by Kweder in an evaluation of remote sensing of gases using lidar techniques (Ref 3), and later by Wank in his study on the detection of carbon dioxide from a shuttle-based lidar (Ref 4). The current work is also based partially on the results of the

European Space Agency report, and should be viewed as a companion volume to the studies by Kweder and Wank.

This report addresses the feasibility of a shuttle-borne lidar system designed to measure atmospheric carbon monoxide. Carbon monoxide (CO) is a toxic pollutant and its effects on urban areas where the automobile density is high have been studied extensively. Less well known, however, are its effects on the earth's atmosphere taken as a whole. For instance, CO is known to figure prominently in the production and transport of other pollutants, such as NO, O₃, and NO₂ (Ref 5:855). Also of interest are the atmospheric sources and sinks of CO. Direct air sample measurements indicate that the primary sources of CO are the combustion of fossil fuels and the ocean, where bacterial decomposition of plankton is suspected (Ref 6:2217). The manner in which CO is destroyed is not well understood. Oxidation by OH, H₂O₂, and HO₂ radicals in the stratosphere accounts for part of the process, but there is also a tropospheric sink whose nature is unknown (Ref 7:2866).

There is also evidence to suggest that trace gases in the atmosphere may have profound long term effects on the earth's weather patterns. For example, an increase in carbon dioxide levels could lead to a dramatic increase in the average global temperature because of what has been termed the "greenhouse" effect. The manner in which CO might effect changes in weather patterns is not clear and more data are necessary if accurate predictions are to be made of the long term effects of the burning of fossil fuels as a primary source of energy.

In order to understand the way in which CO interacts with the

earth's atmosphere, global measurements of the CO number density as a function of altitude above the earth's surface are necessary. A shuttle-based lidar system is ideally suited for this task.

Also addressed in this study is the feasibility of a shuttle-borne lidar system to detect and measure hot CO concentrations near the surface of the earth. Such a capability could be used to analyze the emissions from factory stacks or perhaps to locate and characterize the exhaust plumes from gas turbine or rocket engines.

Problem

The problem of this thesis is to investigate the feasibility of a shuttle-borne lidar system designed to detect and accurately measure atmospheric carbon monoxide concentrations at all altitudes. The basic parameters of the system are those recommended in the European Space Agency study (Ref 2). The primary wavelength selected for the system utilizes a laser/absorption line coincidence reported by Killinger et al (Ref 8:403).

General Approach

The investigation is initially driven by the choice of primary wavelength. Possible candidate lidar systems that can be used to provide the required data are analyzed, and a primary candidate is selected. The number of variables in the analysis is reduced by assuming that the basic telescope and associated optics are fixed. The system variables then are those of the type of laser used and the

technique used to detect and process the received signal. A final system configuration is selected on the basis of the analysis results and its performance is assessed.

Assumptions

The atmospheric carbon monoxide is assumed to be uniformly mixed at 0.075 ppmv (parts per million by volume), that is this relative concentration at sea-level is the same at all altitudes up to 30 km.

The atmosphere is considered to be nonturbulent and without cloud cover. The temperatures, pressures, and total molecular number densities are those given in the U.S. Standard Atmosphere, 1976 (Ref 9). The water-vapor profile is also taken from this reference.

Aerosol concentrations are from the model by McClatchey (Ref 10). Visibility is assumed to be 25 km at 0.55 microns.

II. Lidar Detection of Carbon Monoxide

Lidar techniques have been used to monitor the earth's atmosphere since the early 1960's. The technology has progressed to the point where high-performance systems can now be contained in a relatively compact, light-weight structure suitable for use on a space vehicle. The purpose of this study is to assess the feasibility of one such system, designed to measure atmospheric carbon monoxide from the payload bay of the space shuttle.

The acronym "lidar" stands for light detection and ranging. Lidar systems are also sometimes called laser radars. They function very much like their microwave counterparts: electromagnetic radiation is transmitted into the atmosphere by a pulsed or continuous-wave (CW) laser source, the laser energy is absorbed and scattered by gas molecules and aerosols in its path, and a portion of the scattered radiation is then detected and measured. The amplitude and other characteristics of the scattered radiation that enters the receiver can be used to infer various facts about the volume of atmosphere under consideration. For instance, lidar systems can determine absorption, aerosol content, and also number density of the various constituents along the laser path.

Various lidar techniques and system configurations are used to make atmospheric measurements. If the laser transmitter is colocated with the receiver, the system is referred to as single-ended. If the transmitter and receiver are separated, the system is termed double-ended. The techniques currently in use can be separated into three main groups: Raman, resonance emission (fluorescence), and differential

absorption (DIAL). As one might expect, Raman lidar attempts to detect molecular Raman frequency shifts in the returned signal. Each gas molecule has its own unique Raman spectrum. Therefore, in principle, such a system could use a single excitation frequency to obtain information about all the different gas molecules along the laser path. The biggest disadvantage to Raman lidar is the extremely small scattering cross-section for the molecules of interest (typically $10^{-31} \text{ cm}^2 \text{ sr}^{-1}$). This limits the useful range of the Raman technique to a few km (Ref 11: 1644).

Resonance emission, or fluorescence, lidar techniques make use of a tunable laser source to excite selectively the various molecules of interest. An infrared laser can be used to excite vibrational-rotational transitions of the molecule, or a laser operating in the UV or visible can be used to directly excite atomic transitions. The molecule or atom subsequently fluoresces and the resulting radiation is detected and analyzed. The technique is simple and more sensitive than Raman, since the required cross-sections are much larger. The only real problem with this technique in the infrared is what is known as quenching. That is, non-radiative decay processes such as frequent collisions occur more quickly than radiative decays. As a result, the number of radiative emissions becomes uncertain and the accuracy of the measurement is called into question (Ref 4:15).

The last technique to be discussed is differential absorption lidar, or DIAL. In this technique, radiation is transmitted into the atmosphere at two distinct wavelengths: one of which is tuned to a particular absorption line of the molecule of interest, while the other is

slightly offset from the absorption line to provide a reference signal. The backscattered return signals at the two wavelengths are then compared and analyzed. The amplitude difference between the two is a direct indication of how much laser energy was absorbed by the gas molecules of interest, and hence, their number density can be determined. If a pulsed laser transmitter is used, then the resulting return signals can be compared as a function of time, and range-resolved measurement data then become available. The differential absorption technique is very sensitive and can be used over long ranges, provided sufficient laser power is available.

Of the three lidar techniques just discussed, only resonance emission and differential absorption appear suitable for use in this study. The resonance technique suffers from the quenching problem at IR wavelengths, and therefore should be used only at very high altitudes where the collision probability is lower. Thus, differential absorption lidar appears to be the only technique available to measure the atmospheric content of trace gases such, as carbon monoxide, over the broad range of altitudes required for a shuttle-based system (Ref 12: 624).

System Definition

The lidar system that will be considered in this study is single-ended and utilizes the differential absorption measurement technique. The primary wavelength that will be used is recommended by Killinger et al (Ref 8:403). The wavelength is at 4.64μ in the infrared and utilizes a spectral coincidence between the R(2) transition in the fundamental

absorption band of the CO molecule at 2154.5960 cm^{-1} , and the frequency-doubled R(18) laser line in the $00^{\circ}1-02^{\circ}0$ band of CO_2 at 2154.6050 cm^{-1} . The reference wavelength must be outside the R(2) line of CO, but close enough to the primary so that the difference in absorption experienced at the two wavelengths can be directly attributed to the R(2) line. The wavelength selected for this study uses the frequency-doubled R(10) line of the CO_2 laser at 2143.7674 cm^{-1} (Ref 13).

The spectral coincidence involving a frequency-doubled transition of the CO_2 laser is fortunate. Carbon dioxide laser transitions are very accurately known and CO_2 laser system technology is well advanced. In addition, their efficiency is typically 10-20 percent, which is well above average.

For a pulsed, high peak power application such as that required in this study, a transversely excited atmospheric pressure (TEA) CO_2 laser should be used. Because of the transverse excitation scheme, TEA lasers automatically emit giant, Q-switched like, pulses due to a gain switching action in the lasing medium. The pulses are nominally 100 ns long, and their repetition frequency can be controlled by the excitation process. Pulse energies of up to 20 joules per 100 ns pulse, at a repetition rate of up to 1200 Hz are reported (Ref 14:110).

Carbon dioxide TEA lasers have other advantages as well. They operate at room temperature and usually at atmospheric pressure. They are also self-contained and do not require venting of exhaust gases. Finally, they are line-tunable over a range of about 80 or so rotational-vibrational transitions.

They do have some problem areas that should be noted. The short duration, high energy pulses will cause electromagnetic interference (EMI) problems on the shuttle, if not properly shielded. The normal operating voltage for a typical installation is about 40 kV. This can be extremely dangerous to operating personnel. The last problem area is one that will affect the performance of the system. The output spectral linewidth of the CO₂ TEA laser is about 2-3 GHz (Ref 2:78 and Ref 14:110). This is about the same order of magnitude as the width of a typical CO absorption line at sea-level. It is disadvantageous because it implies that a detailed absorption cross-section as a function of wavelength must be known if accurate measurements of number density are to be extracted from the data. This point will be fully addressed later in the study. For now, it is convenient to state that the CO₂ TEA laser output linewidth assumed in this study is 3 GHz (0.10 cm^{-1}).

In order to achieve the output wavelength specified for the system, the emissions from the primary and reference CO₂ TEA lasers must be frequency-doubled. This can be accomplished through the use of a crystal of CdGeAs₂. Kildal has irradiated this material with 150 ns CO₂ laser pulses and obtained 200 mJ of doubled radiation with a conversion efficiency of 10%. Hinkley states that this crystal should be capable of providing several Watts of average power and hundreds of millijoules of pulsed power (Ref 15:251).

The transmit/receive optics that will be used in this study are those recommended in the European Space Agency study (Ref 2:28). A single telescope will be used for both functions. The telescope has a diameter of 100 cm, and therefore a transmit/receive aperture area of

0.7854 m². It has a radian field-of-view (FOV) of 10⁻⁴, which equates to a solid-angle FOV of 7.854 x 10⁻⁹ sr. The efficiency of the receive optics is assumed to be 0.3, which includes all optical components prior to the detector.

A block diagram of the system is shown in Figure 1, and the basic parameters selected for the study are summarized in Table I below.

Table I
Lidar System Parameters

| | |
|--------------------------------|-----------------------------|
| Primary wavelength | 2154.5060 cm ⁻¹ |
| Reference wavelength | 2143.7674 cm ⁻¹ |
| Laser pulsewidth | 100 ns |
| Laser spectral linewidth | 3 GHz |
| Laser overall efficiency | 20% |
| Diameter of optics | 100 cm |
| Area of optics | 0.7854 m ² |
| Efficiency of receive optics | 0.3 |
| Efficiency of doubling crystal | 0.1 |
| Radian FOV (full angle) | 10 ⁻⁴ radians |
| Steradian FOV | 7.854 x 10 ⁻⁹ sr |

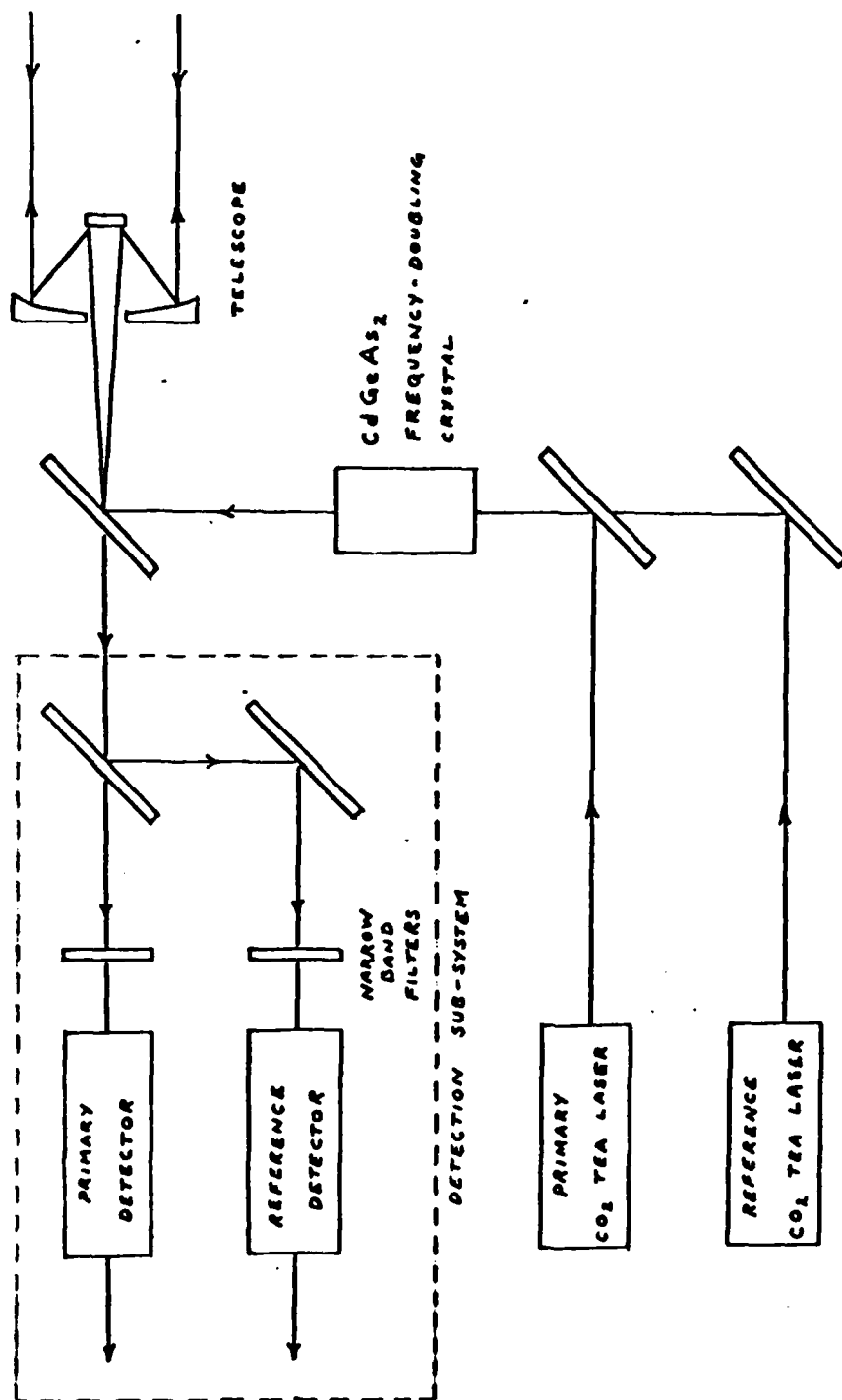


Figure 1. DIAL Lidar System Block Diagram.

The Lidar Equation

The primary equation that will be used to evaluate system performance is known as the "lidar equation". It relates the received signal power from a scattering cell to that initially transmitted by the laser. For the single-ended DIAL system used in this study, it may be written in the following form (Ref 15:76):

$$P_i(R) = P_o \epsilon \kappa \left(\frac{c \tau_a}{2} \right) \beta_i(R) \left(\frac{A_r}{R^2} \right) T_i^2 / R \quad (1)$$

where

| | |
|------------|--|
| $P(R)$ | is the received power from the scatter cell at range R, in Watts |
| i | has value 1 or 2, and refers to the primary and reference wavelengths, respectively. |
| P_o | is the transmitted laser power in Watts |
| ϵ | is the efficiency of the doubling crystal |
| κ | is the efficiency of the receiver optics |
| τ_a | is the receiver integration time in seconds |
| c | is the speed of light in km/sec |
| $\beta(R)$ | is the atmospheric volumetric backscattering coefficient in $\text{km}^{-1}\text{sr}^{-1}$ |
| A_r | is the effective area of the receive optics in m^2 |
| R | is the distance from the lidar to the scatter cell in m |
| T^2 / R | is the two-way atmospheric transmittance along the path from the lidar to the scatter cell |

The coordinate system that will be used in this study has its origin at the lidar system on board the space shuttle, which is assumed to be in a 200 km circular orbit. The system is pointed directly downward so that the range is measured along a line from the shuttle through the earth's center. Thus, sea-level on the earth's surface corresponds to a lidar system range of 200 km, while the range to a scatter cell at an altitude of 30 km above the surface would be 170 km. In this study the results will generally be presented as a function of altitude above the earth's surface, rather than as a function of range from the lidar.

The term $(c \tau_a / 2)$ in equation (1) has dimensions of length and defines the range resolution of the system, ΔR . During the receiver integration time τ_a , the laser pulse illuminates a geometrical length $c \tau_a$ of the atmosphere. However, since the received signal must travel a two-way path, the atmospheric length from which signals are received during this time is just half this value. In this study ΔR is taken to be 1 km, which corresponds to a receiver integration time of 6.67 microseconds.

The volumetric backscatter coefficient in equation (1) has dimensions $\text{km}^{-1} \text{sr}^{-1}$. This term quantifies the fraction of transmitted power that is scattered back to the receiver per unit scatter-cell length per unit solid angle. Here the solid angle is given by the $A_p R^{-2}$ term which is now recognized as the solid angle subtended by the detection system from the scatter cell at range R .

The lidar equation will be more convenient to work with if it is written in a form that isolates any term that is highly sensitive to wavelength. To this end, the atmospheric transmission term in equation

(1) can be written as:

$$T^2|_R = T_A^2|_R \cdot T_{CO}^2|_R \quad (2)$$

where $T_{CO}^2|_R$ is the two-way atmospheric transmission due to the R(2) absorption line of CO

$T_A^2|_R$ is the two-way atmospheric transmission due to all other factors

Then, the received power at the primary wavelength can be written:

$$P_1(R) = P_o \epsilon K \left(\frac{c\tau_0}{2} \right) \beta_1(R) \left(\frac{A_r}{R^2} \right) T_A^2|_R \cdot T_{CO}^2|_R \quad (3)$$

and the received power at the reference wavelength becomes:

$$P_2(R) = P_o \epsilon K \left(\frac{c\tau_0}{2} \right) \beta_2(R) \left(\frac{A_r}{R^2} \right) T_A^2|_R \quad (4)$$

where it has been assumed that the atmospheric transmittance due to all other factors except the R(2) line of CO is the same at both wavelengths. This is reasonable, since the reference wavelength was chosen specifically to make this assumption valid.

It can also be assumed that the atmospheric backscatter coefficients at both wavelengths are approximately equal to one another, since β is a slowly varying function of wavelength (Ref 2:58).

Then, if the laser output power is the same for both the primary and reference systems, it can be seen that the returned power levels

for the two will be related by:

$$P_1(R) = P_2(R) T_{co}^2 \Big|_R \quad (5)$$

This equation just expresses the fact that P_1 suffers selective absorption due to the R(2) line of CO while P_2 does not.

In a range-resolved DIAL system, the above relation can be used to obtain an equation for the average number of CO molecules in a range cell ΔR , extending from a range R_1 to R_2 . The ratios of power received at the primary wavelength to that at the reference at R_1 and R_2 are:

$$\frac{P_1(R_1)}{P_2(R_1)} = T_{co}^2 \Big|_{R_1} \quad (6)$$

and:

$$\frac{P_1(R_2)}{P_2(R_2)} = T_{co}^2 \Big|_{R_2} \quad (7)$$

Now, the atmospheric transmittance can be expressed, using Bouguer's (Beer's) Law, as (Ref 15:49):

$$T_{co}^2 \Big|_R = \exp \left\{ -2 \int_0^R N_{co}(r) \nabla_{co}(r) dr \right\} \quad (8)$$

where N_{co} is the CO number density
 ∇_{co} is the absorption cross-section due to the R(2) line of CO at the primary wavelength

Then, it can be shown that:

$$\frac{P_1(R_2)}{P_2(R_2)} \cdot \frac{P_2(R_1)}{P_1(R_1)} = \exp \left\{ -2 \int_0^{R_2} N_{CO}(r) \sigma_{CO}(r) dr + 2 \int_0^{R_1} N_{CO}(r) \sigma_{CO}(r) dr \right\} \quad (9)$$

or:

$$\frac{P_1(R_2)}{P_2(R_2)} \cdot \frac{P_2(R_1)}{P_1(R_1)} = \exp \left[-2 \int_{R_1}^{R_2} N_{CO}(r) \sigma_{CO}(r) dr \right] \quad (10)$$

Now if the number density and cross-section of CO are assumed constant and equal to their average values over the range cell, then:

$$\frac{P_1(R_2)}{P_2(R_2)} \cdot \frac{P_2(R_1)}{P_1(R_1)} = \exp \left[-2 (R_2 - R_1) \overline{N_{CO}} \overline{\sigma_{CO}} \right] \quad (11)$$

and the average number density can be found from:

$$\overline{N_{CO}} = - \frac{1}{2 \Delta R \overline{\sigma_{CO}}} \ln \left[\frac{P_1(R_2)}{P_2(R_2)} \cdot \frac{P_2(R_1)}{P_1(R_1)} \right] \quad (12)$$

where $\Delta R = R_2 - R_1$

Since the pulsed lidar return signal is range resolved, the above relation can be used to calculate the CO number density for each range cell of interest.

III. Molecular Structure of Carbon Monoxide

The evaluation of the lidar equation requires a precise knowledge of atmospheric transmission at the wavelength of interest. The purpose of this and the following section is to lay the groundwork for these calculations, as well as gain a firm understanding of the manner in which the CO molecule interacts with the transmitted laser radiation.

The Carbon Monoxide Molecule

Carbon monoxide is a heteronuclear diatomic molecule whose characteristics are well known. Atmospheric CO contains four principle isotopic species: $^{12}\text{C}^{16}\text{O}$, $^{13}\text{C}^{16}\text{O}$, $^{12}\text{C}^{18}\text{O}$, and $^{12}\text{C}^{17}\text{O}$. The most abundant is $^{12}\text{C}^{16}\text{O}$, which comprises 98.652 percent of atmospheric CO (Ref 16:6). Table II lists the molecular constants for this particular isotope. Since it is principally $^{12}\text{C}^{16}\text{O}$ that will be detected, the remainder of the study assumes that the term "CO" refers to this isotope.

Table II
Molecular Constants for $^{12}\text{C}^{16}\text{O}$

| | |
|----------------|-------------------------|
| ω_e | 2169.8196 |
| $\omega_e x_e$ | 13.2918 |
| $\omega_e y_e$ | 1.1229×10^{-2} |
| $\omega_e z_e$ | -4.7×10^{-7} |
| B_e | 1.931265 |
| D_e | 6.1025×10^{-6} |

All values in cm^{-1} (Ref 17:327)

This study is concerned with the CO molecule's interaction with electromagnetic radiation in the infrared region of the spectrum. The interaction is one between the incident photon and the molecule's changing dipole moment. Heteronuclear molecules have a permanent dipole moment associated with them. Rotation or vibration of the molecule causes shifts in the dipole moment which allow the molecule to absorb radiation. Classical electrodynamics predicts that such an interaction can occur for any frequency that matches that of the rotating or vibrating molecular system. However, the quantum theory gives the correct result that such an interaction can occur only for certain discrete frequencies associated with transitions between the various energy levels of the system. These energy levels are characterized by the rotational quantum number J, and the vibrational quantum number v.

Distribution of CO Molecules in Vibrational States

The energy difference between a molecule in the first vibrational state and one in the ground vibrational state is given approximately by (Ref 18:95):

$$\Delta E_{1-0} = \omega_e - 2 \omega_e x_e \quad (13)$$

where the needed values can be obtained from Table II, resulting in an energy difference of about 2143.2 cm^{-1} .

This energy difference can be used to calculate the ratio of molecules in the first vibrational state to those in the ground vibrational

state. According to the Maxwell-Boltzmann distribution law, the ratio is given by:

$$\frac{N_i}{N_0} = \exp \left[- \frac{\Delta E_{i,0}}{k T} \right] \quad (14)$$

where k is the Boltzmann constant and T is the absolute temperature. For a sea-level temperature of 296°K , the ratio is about 3.0×10^{-5} . Therefore, to a good approximation, all of the CO molecules are in the ground vibrational state at this temperature. In addition, the mean atmospheric temperatures at the altitudes considered in this report are equal to or less than 296°K , so the above statement can be extended to encompass all atmospheric CO molecules as well.

"Hot" CO in the atmosphere, such as that emanating from a factory stack or a rocket engine exhaust plume, might have molecular temperatures ranging from 400°K to 1000°K . As an upper limit, consider the N_i/N_0 ratio at 1000°K :

$$\left. \frac{N_i}{N_0} \right|_{1000^\circ\text{K}} = 4.58 \times 10^{-2} \quad (15)$$

Even at high temperatures, most of the molecules are in the ground vibrational state.

Absorption Line Positions for the 1-0 Band of CO

The fundamental absorption band for CO is characterized by transitions where the initial vibrational state is the ground state $v=0$, and the final state is the $v=1$ state. The transitions are further

characterized by the value of the rotational quantum number J .

To a first approximation, the molecular energy levels associated with the transitions can be represented by two additive components associated with (1) the rotation of the molecule, and (2) its vibrational state. A very careful study of the vibrational-rotational interaction was made by J.L. Dunham. He expressed the energy levels of the various states as a double power series in J and v (Ref 18:109):

$$T(v, J) = \sum_{i,j} Y_{ij} (v + \frac{1}{2})^i [J(J+1)]^j \quad (16)$$

where the Y_{ij} coefficients in the series are known as the Dunham coefficients. This series is similar to the usual spectroscopic representation in that $Y_{10} \sim \omega_e$, $Y_{20} \sim -\omega_e x_e$, $Y_{01} \sim B_e$, etc.

This study will use the Dunham coefficients for CO tabulated by Todd et al (Ref 19:224) to calculate the absorption line positions for the 1-0 band of the CO molecule. The coefficients used in the energy level calculations are given in Table III. The line positions calculated from these energy levels are listed in Appendix A. These positions are stated in the Todd study to be accurate to $\pm 0.0005 \text{ cm}^{-1}$. The P,R branch terminology is standard and refers to a $\Delta J = -1$ transition for the P branch, and a $\Delta J = 1$ transition for the R branch.

Calculation of Line Strength for the CO 1-0 Band

The line strength, or integrated intensity, for an individual line in the CO absorption spectrum is defined according to the following

Table III
Dunham Coefficients for CO

| | |
|----------|------------------------------|
| Y_{10} | 2169.813844 |
| Y_{20} | -13.2884214 |
| Y_{30} | 10.52536×10^{-3} |
| Y_{40} | 5.6644×10^{-5} |
| Y_{50} | 10.0327×10^{-7} |
| Y_{60} | -3.18476×10^{-8} |
| Y_{01} | 1.931280880 |
| Y_{11} | $-1.75043079 \times 10^{-2}$ |
| Y_{21} | 5.6767×10^{-7} |
| Y_{31} | 2.3691×10^{-8} |
| Y_{02} | -6.120712×10^{-6} |
| Y_{12} | 10.6399×10^{-10} |
| Y_{22} | -1.78578×10^{-10} |
| Y_{03} | 5.6676×10^{-12} |
| Y_{13} | -1.62587×10^{-13} |

All values in cm^{-1} (Ref 19:224)

relation (Ref 15:240):

$$S_m = \int_{-\infty}^{\infty} \nu(\nu) d\nu \quad (17)$$

where S_m is the line strength in $\text{cm}^2 \text{mol}^{-1} \text{cm}^{-1}$, and $\nu(\nu)$ is the absorption cross-section of the molecule at wavenumber ν .

The intensity variation of line strength as a function of the rotational quantum number J depends on the relative fraction of the total number of molecules in that particular J state. This suggests that the individual line strength can be calculated from:

$$S_m = \frac{N_J}{N_{\text{TOT}}} \left[\sum S_m \right] \quad (18)$$

where N_J/N_{TOT} is the fractional number of molecules in state J , and $\sum S_m$ is the sum of all line strengths in the band, or the "band sum". The band sum for the CO 1-0 band is reported to be $981.3 \times 10^{-20} \text{ cm}^2 \text{mol}^{-1} \text{cm}^{-1}$, at an absolute temperature of 296°K (Ref 20:793). The ratio N_J/N_{TOT} is given by (Ref 18:125):

$$\frac{N_J}{N_{\text{TOT}}} = \frac{(2J+1)}{Q_r} \exp \left\{ - \frac{hc B J(J+1)}{k T} \right\} \quad (19)$$

where Q_r is the rotational partition function; and B is the ground state rotational constant, which has the value 1.9225 cm^{-1} (Ref 19:207). The rotational partition function takes the form:

$$Q_r = \sum_{J=1}^{\infty} (2J+1) \exp \left\{ - \frac{hc B J(J+1)}{k T} \right\} \quad (20)$$

For small values of B, Q_r may be approximated by the integral (Ref 18:125):

$$Q_r \approx \int_0^{\infty} (2J+1) \exp \left\{ - \frac{hcB J(J+1)}{kT} \right\} dJ \quad (21)$$

or:

$$Q_r \approx \frac{kT}{hcB} \quad (22)$$

The expression for N_J/N_{TOT} then becomes:

$$\frac{N_J}{N_{TOT}} = \frac{hcB}{kT} (2J+1) \exp \left\{ - \frac{hcB J(J+1)}{kT} \right\} \quad (23)$$

In equation (23) it is assumed that the transition probabilities for the band are the same for all lines. Actually, the probability is weakly dependent on J, in that a particular line intensity depends on the average value of J for the upper and lower states involved in the transition. Taking this into account, the equation becomes (Ref 18:126):

$$\frac{N_J}{N_{TOT}} = \frac{hcB}{kT} (J' + J'' + 1) \exp \left\{ - \frac{hcB J''(J''+1)}{kT} \right\} \quad (24)$$

where J' refers to the upper state and J'' to the lower.

The equation for the line strength can now be written:

$$S_m = \left[\sum S_m \right] \cdot \left[\frac{hcB}{kT} (J' + J'' + 1) \exp \left\{ - \frac{hcB J''(J''+1)}{kT} \right\} \right] \quad (25)$$

Line strengths for the CO 1-0 band calculated from this expression are tabulated in Appendix A.

These line strengths were calculated at the reference temperature 296°K. Line strengths at other temperatures can be calculated from these reference values from the following (Ref 16:3):

$$S_m(T) = \frac{S_m(T_s) Q_v(T_s) Q_r(T_s)}{Q_v(T) Q_r(T)} \exp \left\{ \frac{1.439 E''(T-T_s)}{T T_s} \right\} \quad (26)$$

where Q_v, Q_r are the vibrational and rotational partition functions, respectively, $S_m(T_s)$ is the line strength at 296°K, and E'' is the energy of the lower state of the transition in cm^{-1} . For CO, the vibrational partition function is independent of temperature (for the range considered in this study), and the ratio $Q_v(T_s)/Q_v(T)$ is equal to one (Ref 16:4). Using the approximation for Q_r given in equation (22), the ratio $Q_r(T_s)/Q_r(T)$ becomes T_s/T . Therefore, equation (26) can now be written as:

$$S_m(T) = S_m(T_s) \left[\frac{T_s}{T} \right] \exp \left\{ \frac{1.439 E''(T-T_s)}{T T_s} \right\} \quad (27)$$

IV. Atmospheric Transmission

Solution of the lidar equation requires accurate knowledge of atmospheric transmission at the wavelength of interest, in this case the lidar primary wavelength at $2154.6050 \text{ cm}^{-1}$. Recall that the atmospheric transmission term in the lidar equation was separated into two factors. One was the transmission due solely to the R(2) absorption line, which can be written (from equation (8)):

$$T_{co}^2 \Big|_R = \exp \left\{ -2 \int_0^R N_{co}(r) \tau_{co}(r) dr \right\} \quad (8)$$

It is clear from this equation that in order to calculate the transmission, the number density of CO and the absorption cross-section of the R(2) line at the primary wavelength must be known as a function of range. The approach taken in this study is to break the atmospheric path into R range-cells, each of length $\Delta R = 1 \text{ km}$, which is the vertical resolution of the system. The number density and absorption cross-section are then assumed constant over the range-cell. The transmission can then be calculated for each range-cell and the total transmission obtained from a product of the constituent range-cell transmissions in the path under consideration. Therefore:

$$T_{co}^2 \Big|_R = \prod_{i=0}^R T_{co}^2 (R_i) \quad (28)$$

where T_{CO}^2/R is the total two-way atmospheric transmission due to the R(2) line of CO to a range R

$T_{CO}^2(R_i)$ is the two-way atmospheric transmission along a 1 km vertical path at a range R_i

$T_{CO}^2(R)$ can be written more explicitly as:

$$T_{CO}^2(R) = \exp \left\{ -2 (N_{CO} \sigma_{CO}) \Delta R \right\} \quad (29)$$

where the number density and cross-section are understood to be evaluated in the range-cell of interest. The atmospheric transmission data can then be presented in tabular form for each range-cell or, by using the conversion noted earlier, for each atmospheric layer. In this study, it is assumed that any atmospheric absorption effects above an altitude of 30 km can be neglected. Therefore, the transmission must be calculated for each of 30 range-cells extending from sea-level to an altitude of 30 km.

The second atmospheric transmission term in the lidar equation T_A^2/R , was stated to be the two-way transmission due to all other species except the R(2) line of CO. Using Beer's law, this term can be written:

$$T_A^2/R = \exp \left\{ -2 \int_0^R \mathcal{E}(r) dr \right\} \quad (30)$$

where $\mathcal{E}(r)$ is the extinction coefficient for all atmospheric species except the R(2) line of CO. More explicitly, $\mathcal{E}(r)$ can be written:

$$\mathcal{E}(\nu) = \mathcal{E}_R + \mathcal{E}_M + \mathcal{E}_{\text{CO}_2} + \mathcal{E}_{\text{N}_2\text{O}} + \mathcal{E}_{\text{O}_3} + \mathcal{E}_{\text{H}_2\text{O}} + \mathcal{E}_{\text{CO-}} \quad (31)$$

| | | |
|-------|------------------------------------|--|
| where | \mathcal{E}_R | is the extinction coefficient due to Rayleigh scattering |
| | \mathcal{E}_M | is the extinction coefficient due to Mie (aerosol) scattering |
| | $\mathcal{E}_{\text{CO}_2}$ | is the molecular extinction coefficient due to CO ₂ absorption |
| | $\mathcal{E}_{\text{N}_2\text{O}}$ | is the molecular extinction coefficient due to N ₂ O absorption |
| | \mathcal{E}_{O_3} | is the molecular extinction coefficient due to ozone absorption |
| | $\mathcal{E}_{\text{H}_2\text{O}}$ | is the molecular extinction coefficient due to water-vapor absorption |
| | $\mathcal{E}_{\text{CO-}}$ | is the molecular extinction coefficient due to nearby CO absorption lines |

The five molecules listed are the primary constituents of the atmosphere thought to be responsible for attenuation of electromagnetic radiation in the wavelength band considered in this report (Ref 15:36). Not all of them have a significant impact on the calculation at 2154.6050 cm⁻¹, as will be seen.

Accordingly, T_A^2 / R can also be written as a product of transmissions over individual range-cells. Therefore, let:

$$T_A^2 / R = \prod_{i=0}^R T_A^2(R_i) \quad (32)$$

where $T_A^2(R_i)$ is the two-way atmospheric transmission along a 1 km vertical path at range R_i

$T_A^2(R)$ can be written more explicitly as:

$$T_A^2(R) = \exp \left\{ -2 \left[\epsilon_R + \epsilon_M + \epsilon_{CO_2} + \epsilon_{N_2O} + \epsilon_{O_3} + \epsilon_{H_2O} + \epsilon_{CO} \right] \Delta R \right\} \quad (33)$$

where the extinction coefficients are understood to be evaluated in the range-cell under consideration.

The remainder of this section will develop the theory and calculations necessary to evaluate equations (29) and (33), which can then be used to calculate the atmospheric transmission for the lidar equation over any path of interest.

Atmosphere Model

The earth's atmosphere is generally regarded as being composed of layers, each of which is characterized by its temperature profile. The lowest layer is characterized by a temperature that decreases linearly from sea-level to an altitude of about 12 km. Above this altitude the temperature starts to increase once again. This point is called the tropopause. It divides the atmosphere into two regions: the atmosphere below the tropopause, called the troposphere; and that above the tropopause, called the stratosphere.

The range of altitudes that will be considered in this study is from sea-level to 30 km. Above this altitude the particle and molecular number densities are so low that any absorption that occurs is

negligible.

The basic atmosphere model used in this study is from the 1976 version of the U.S. Standard Atmosphere (Ref 9). The temperature, pressure, and total number density profiles extracted from this reference are reproduced as Appendix B.

Carbon monoxide is assumed to be a uniformly mixed gas throughout the altitude range considered in this study (Ref 16:2). The mixing ratio is variously reported, depending on time and place, as between 0.05 and 0.25 ppmv (Ref 21:1-2). In this study, a mixing ratio of 0.075 ppmv is assumed, which should produce conservative results (Ref 16:2). Using this mixing ratio, the total atmospheric molecular number density, and the fact that 0.98652 of atmospheric CO is the isotope $^{12}\text{C}^{16}\text{O}$; the number densities for this isotope can be calculated as a function of altitude. The results are tabulated in Appendix B.

The water-vapor profile assumed in this study is also from the 1976 U.S. Standard Atmosphere. The mixing ratio for water-vapor is not constant and is tabulated in the reference in 2 km altitude increments. The values given are average mid-latitude concentrations and they include average contributions from thunderstorms and other stratospheric sources above 16 km (see Ref 9:44 for additional detail). The water-vapor number densities used in this study are given in Appendix I.

In the infrared wavelength band considered in this study, most of the atmospheric scattering of electromagnetic radiation is caused by particulates rather than by gas molecules. Thus, the aerosol model used is of particular importance. Three different models, from which the aerosol absorption and scattering coefficients can be calculated, were

examined for this study. The model by Shettle and Fenn (Ref 22) was used by Wank in his study. An earlier (1964) model by Elterman (Ref 23) was also considered, as well as a model by McClatchey et al. published in 1972 (Ref 10).

The model by McClatchey was chosen for use in this study. Like the Shettle and Fenn model, it is based on recent experimental measurements; but it has the added benefit that it presents the aerosol extinction coefficients in tabular form, as a function of altitude, and at selected wavelengths that span the visible and the IR. Coefficient values at other wavelengths can be linearly interpolated between tabulated values with a stated error of less than ± 8 percent. The interpolated values at $2154.6050 \text{ cm}^{-1}$ are given in Appendix C. The values listed are for a clear atmosphere, visibility 23 km at 0.55 microns.

Absorption and Scattering in the Atmosphere

When electromagnetic radiation propagates through the atmosphere, two main processes are in action, absorption and scattering. These two processes must be considered (1) at the molecular level, where the wavelength of the incident IR radiation is much larger than the molecular diameter, and (2) at the aerosol level, where the incident wavelength and particle diameter are roughly equivalent.

Absorption and scattering enter into the lidar equation at two points. First, the atmospheric transmission term quantitatively describes the attenuation of the propagating signal using Beer's law:

$$T = e^{-\epsilon R} \quad (34)$$

where R is the distance propagated, and ϵ is referred to as the extinction coefficient, which can be explicitly written as:

$$\epsilon = \epsilon_{\text{AEROSOL ABSORPTION}} + \epsilon_{\text{AEROSOL SCATTER}} + \epsilon_{\text{MOLECULAR ABSORPTION}} + \epsilon_{\text{MOLECULAR SCATTER}} \quad (35)$$

where the individual contribution of each process has been recognized.

The two aerosol extinction coefficients are usually summed and referred to as the Mie extinction coefficient, ϵ_M .

The molecular scattering extinction coefficient is generally referred to as the Rayleigh scattering extinction coefficient and notated ϵ_R .

The molecular absorption extinction coefficient is dependent upon the specific absorption effects of all the molecules in the path, and is therefore extremely wavelength sensitive. In this study the line-by-line contribution of five molecular species are considered, and the extinction coefficient is written as the sum of five terms (see equation 31).

The second term in the lidar equation that depends on the absorption and scattering processes is the volumetric backscattering coefficient, β . It is this term that determines how much incident energy is scattered back toward the lidar receiver. It is usually written as the sum of two terms:

$$\beta = \beta_R + \beta_M \quad (36)$$

β_R is due to the Rayleigh, or molecular scattering process; and β_M is due to Mie or aerosol scattering. As one might expect, β_R can be related to ϵ_R ; and β_M can be related to ϵ_M through the use of an angular distribution function.

Rayleigh Scattering Extinction Coefficient

The extinction coefficient due to Rayleigh scattering can be calculated from:

$$\epsilon_R = N_{TOT} \sigma_R \quad (37)$$

where N_{TOT} is the total number density of molecules, and σ_R is the Rayleigh scattering cross-section.

There is a quasi-empirical equation for the Rayleigh scattering cross-section that yields accurate results up to an altitude of 100 km (Ref 15:98):

$$\sigma_R(\lambda) = 4.56 (\lambda / 0.55)^{-4} \times 10^{-27} \text{ [cm}^2\text{]} \quad (38)$$

where λ is the wavelength in microns.

Using equation (38) and the total atmospheric molecular number density from Appendix B, the Rayleigh scattering extinction coefficient can be calculated as a function of altitude for a wavelength of 2154.6050

cm⁻¹ (4.64122 microns). The results are given in Appendix D.

Rayleigh Volumetric Backscattering Coefficient

The volumetric backscatter coefficient due to Rayleigh scattering can be calculated from (Ref 2:22):

$$\beta_R = \left. \frac{d\sigma}{d\Omega} \right)_{180} N_{TOT} \quad (39)$$

where $\left. \frac{d\sigma}{d\Omega} \right)_{180}$ is the differential scattering cross-section in the $\theta = 180^\circ$ direction, which has dimensions cm² sr⁻¹, and N_{TOT} is the total number density of all molecules in cm⁻³.

The differential scattering cross-section is given by (Ref 2:23):

$$\frac{d\sigma}{d\Omega} = \frac{3 \sigma_R}{16 \pi} (1 + \cos^2 \theta) \quad (40)$$

where σ_R is the Rayleigh scattering cross-section and θ is the scatter angle ($\theta = 0$ is in the forward direction). Therefore:

$$\left. \frac{d\sigma}{d\Omega} \right)_{180} = \frac{3 \sigma_R}{8 \pi} \quad (41)$$

Then, combining equations (37), (39), and (41):

$$\beta_R = \frac{3}{8 \pi} \mathcal{E}_R \quad (42)$$

where the factor $3/8\pi$ is recognized as the angular distribution term noted earlier.

The Rayleigh volumetric backscattering coefficients calculated from

equation (42) and the values in Appendix D, are given in Appendix E.

Aerosol Extinction Coefficients

Atmospheric attenuation due to absorption and scattering by particulates can be derived theoretically for spherical particles from a theory developed by Mie (1908). Thus aerosol scattering is referred to as Mie scattering. In contrast to the Rayleigh scattering phenomenon, Mie scattering is a great deal more complex. The Mie absorption and scattering extinction coefficient depends on the number density and size distribution of the aerosols, as well as on their complex indices of refraction. Whereas, the Rayleigh extinction coefficient could be calculated from a simple empirical expression, the Mie extinction coefficient is usually tabulated as a function of wavelength and altitude for any of several meteorological conditions.

The Mie extinction coefficients used in this study are given in Appendix C. As stated earlier, ϵ_M is the sum of an absorption component and a scattering component. These components are also given in Appendix C.

Aerosol Volumetric Backscattering Coefficient

The aerosol volumetric backscattering coefficient is given by (Ref 2:16):

$$\beta_M = \left(\frac{d\sigma}{d\Omega} \right)_{180} N_{TOT} \quad (43)$$

where $\frac{d\sigma}{d\Omega}\bigg|_{180}$ is the differential backscattering cross-section, this time due to Mie scattering; and N_{TOT} is the total particle number density.

In the section on the Rayleigh backscattering coefficient, it was shown that β_R and ϵ_R are related through an angular distribution function. In analogous fashion, it can be shown that (Ref 2:16):

$$\beta_M = \rho(\theta) \epsilon_{\text{AEROSOL SCATTER}} \quad (44)$$

where ρ is the distribution function of interest and $\epsilon_{\text{AEROSOL SCATTER}}$ is the scattering component of ϵ_M . Certainly the temptation here is to assume an isotropic distribution and set $\rho(\theta) = 1/4\pi$, since the actual distribution function is not analytically known for particles of arbitrary size and surface shape. As it turns out, the distribution function is not isotropic, but experimental measurements indicate that the ratio β_M/ϵ_M is about 0.01-0.04 (Ref 15:96). If $\rho(\theta)$ is assumed to be $1/4\pi$ at $\theta = 180^\circ$, a sample calculation using the data in Appendix C and equation (44) yields a β_M/ϵ_M ratio of 0.04 at sea-level. Therefore, using an angular distribution factor of $1/4\pi$ produces results that are in agreement with experimental measurements.

The final equation for β_M can then be written as:

$$\beta_M = \epsilon_M / 4\pi \quad (44a)$$

The aerosol volumetric backscattering coefficients calculated from equation (44) and the data in Appendix C, are listed in Appendix E. Also listed in this appendix are the values for the total volumetric backscattering coefficient calculated from equation (36).

Molecular Extinction Coefficients

The atmospheric extinction coefficient for a given molecular species is given by (Ref 15:103):

$$\mathcal{E}_i = N_i \sigma_i \quad (45)$$

where N_i is the number density of the absorbing species, and σ_i is its absorption cross-section. The absorption cross-section in this equation is dependent upon the line-strength of the of the particular absorption line of interest, and also its line-width. These two parameters can be used to define a line-shape function which gives the absorption cross-section as a function of wavenumber.

In the lower atmosphere, the line-shape function is Lorentzian and takes the form (Ref 10:12):

$$\sigma(\nu) = \left(\frac{S}{\pi} \right) \frac{\alpha}{(\nu - \nu_0)^2 + \alpha^2} \quad (46)$$

| | | |
|-------|----------|---|
| where | S | is the line strength |
| | α | is the line half-width at half-maximum |
| | ν | is the wavenumber of the incident radiation |
| | ν_0 | is the wavenumber of the absorption line center |

The Lorentzian line-shape is a product of collision broadening, and is valid to an altitude of perhaps 20 km. Very high in the atmosphere (above 30 km) the line-shape is Gaussian, which is an indication that

only Doppler broadening effects are present. In the region between, at 20-30 km altitude, the line-shape function is a convolution of the Lorentzian and Gaussian functions, known as a Voight profile.

This study assumes that the absorption line-shape can be represented, throughout the altitudes of interest, by a simple Lorentzian, as given in equation (46). The cross-section so derived is approximately correct and will not affect the accuracy of the results, since absorption effects above 20 km will be small in any case (Ref 10:12).

The line-strength and line-width parameters used to calculate the absorption cross-section are both functions of altitude. An equation giving the temperature dependence of line-strength has already been developed and was stated earlier as equation (26). Using this equation and the temperature data in Appendix B, the line-strength as a function of altitude can be calculated from its sea-level value.

The pressure and temperature dependence of the absorption line-width is given by (Ref 10:12):

$$\alpha(T, P) = \alpha_s \frac{P}{P_s} \sqrt{\frac{T_s}{T}} \quad (47)$$

| | | |
|-------|------------|---|
| where | α_s | is the line half-width at half-maximum at sea-level |
| | T_s | is the sea-level temperature |
| | P/P_s | is the atmospheric pressure ratio |

From this equation and the data in Appendix B, the absorption line-width as a function of altitude can be calculated from its sea-level value.

Once line-strength and line-width are known, it becomes a simple matter of using equation (46) to calculate the absorption cross-section for a single line at the wavenumber of interest. This approach is adequate if only one or a small number of lines contribute to the total absorption cross-section, but for a large number of lines the number of calculations becomes prohibitive.

The absorption cross-section at altitude can be approximated from its sea-level value if the wavenumber at which the cross-section is to be calculated is not in the central peak of any absorption line. If this condition holds, then the equation for absorption cross-section becomes:

$$\tau(\nu) = \left(\frac{S}{\pi} \right) \frac{\alpha}{(\nu - \nu_0)^2} \quad (48)$$

since the $(\nu - \nu_0)^2$ term is much greater than α^2 for wavenumbers far from ν_0 . Thus, if the sea-level value of τ is given by:

$$\tau_s = \left(\frac{S_s}{\pi} \right) \frac{\alpha_s}{(\nu - \nu_0)^2} \quad (49)$$

and its value at altitude by:

$$\tau_h = \left(\frac{S_h}{\pi} \right) \frac{\alpha_h}{(\nu - \nu_0)^2} \quad (50)$$

Then:

$$\tau_h = \tau_s \frac{S_h}{S_s} \cdot \frac{\alpha_h}{\alpha_s} \quad (51)$$

and finally, using equations (26) and (47):

$$\tau_h = \tau_s \left[\frac{T_s}{T} \exp \left\{ \frac{1.439 E'' (T - T_s)}{T T_s} \right\} \right] \cdot \left[\frac{P}{P_s} \sqrt{\frac{T_s}{T}} \right] \quad (52)$$

The value of E'' used in the approximation should be associated with the absorption line that contributes most to the total cross-section.

Using the equations developed above, the required molecular extinction coefficients can now be calculated.

Extinction Coefficients for CO. The molecular extinction coefficient at $2154.6050 \text{ cm}^{-1}$ due to nearby CO lines (not to include the R(2) line) can be calculated at sea-level using equation (45). The total absorption cross-section will just be the sum of the individual cross-sections for each line calculated from equation (46).

The only parameter that is needed to complete these calculations is the CO line half-width at half-maximum. For this study, the experimental measurements by Bouanich and Haeusler will be used (Ref 24:695). They report a CO absorption line half-width of about $0.07 \text{ cm}^{-1} \text{ atm}^{-1}$ for the lower J numbered transitions.

The calculated sea-level absorption cross-section values for the nearest 25 CO lines are given in Appendix F. The total absorption cross-section $\tau_{\text{CO-}}$, is calculated to be $2.595 \times 10^{-21} \text{ cm}^2$ at sea-level.

The value of $\tau_{\text{CO-}}$ as a function of altitude can now be calculated from equation (52) and the data in Appendix B. The value for E'' used should be the one associated with the R(3) transition, since it

contributes most to the total sea-level cross-section. The lower state energy for this transition is calculated from the Dunham coefficients as $1104.65560 \text{ cm}^{-1}$. The cross-section values as a function of altitude are given in Appendix G.

Finally, the atmospheric extinction coefficient ϵ_{CO_2} can be calculated from the CO number density data in Appendix B, and the cross-section data just determined. These results are also given in Appendix G.

CO₂ Absorption Near 2154 cm⁻¹. Carbon dioxide is a linear triatomic molecule whose vibration-rotation bands span the range between approximately 500 cm⁻¹ and 12,820 cm⁻¹ (Ref 15:37). The CO₂ molecule has three main vibrational frequencies: ν_1 , ν_2 , and ν_3 . Of these, ν_1 is optically inactive because of the symmetry of its dipole moment during vibration. The remaining two vibration bands, ν_2 and ν_3 , are centered near 667 cm⁻¹ and 2326 cm⁻¹, respectively. The main ν_3 band, along with the combination band $\nu_1 + \nu_2$ are close enough to the primary lidar wavelength to require further examination.

The ν_3 band of CO₂ absorbs very heavily in the wavelength region 2247 cm⁻¹ to 2387 cm⁻¹. The P(50) line for this band is located at about 2242 cm⁻¹, and the line structure is weak past this point (Ref 25: 5-95). From this it can be concluded that there are no strong lines from this band present at the primary wavelength.

The $\nu_1 + \nu_2$ combination band of CO₂ is centered at about 2079 cm⁻¹ and extends from about 2037 cm⁻¹ to 2114 cm⁻¹. The primary lidar wavelength at 2154 cm⁻¹ lies well beyond the R(40) line of this band

(Ref 25:5-95). Therefore it can be concluded that any absorption effects due to the CO₂ molecule at the primary wavelength considered in this study will be small and can be neglected.

N₂O Absorption Near 2154 cm⁻¹. Nitrous oxide is a linear asymmetric molecule with three main vibration frequencies: ν_1 at 1285.6 cm⁻¹, ν_2 at 588.8 cm⁻¹, and ν_3 at 2223.5 cm⁻¹. Even though N₂O has many combination bands and hot bands, they do not contribute much to atmospheric absorption.

There are two bands of N₂O near the primary wavelength: a weak, $(\nu_3 + \nu_2) - \nu_1$, band at about 2212 cm⁻¹ and the fundamental ν_3 band at 2223.5 cm⁻¹. The ν_3 band has strong lines extending from about 2163 cm⁻¹ to 2262 cm⁻¹ (Ref 25:5-95). The weaker band extends from about 2165 cm⁻¹ to 2242 cm⁻¹. Therefore, it can be concluded that any absorption effects from N₂O at 2154 cm⁻¹ will be small and can be neglected.

Ozone Absorption Near 2154 cm⁻¹. Ozone is an asymmetric-top molecule with three main vibration frequencies. All three are active in infrared absorption. Two combination bands are in the region of interest to this study: the strong $\nu_1 + \nu_3$ band centered at about 2105 cm⁻¹, and the weaker $2\nu_1$ band centered at about 2206 cm⁻¹.

The primary wavelength at 2154.6050 cm⁻¹ is situated between these two bands. The stronger of the two, $\nu_1 + \nu_3$, has been measured at high-resolution (Ref 26:416). The extent of the measured lines in the study ranged from 2065.1 cm⁻¹ to 2135.5 cm⁻¹. Here again, it can be concluded that any absorption effects due to O₃ will be small and can be

neglected.

Extinction Coefficients for H₂O. The wavelength region around 2154 cm⁻¹ contains numerous water-vapor absorption lines. Water-vapor has an asymmetric-top molecular structure. The absorption spectra of this molecule are extremely complex and difficult to calculate. Fortunately there is an excellent reference available by Flaud and Camy-Peyret (Ref 27) that gives the line-positions, line-intensities, and lower state energy levels for the water-vapor molecule in the wavelength region of interest to this study. These values were calculated at a pressure of 1 atm and a temperature of 296°K. Appendix H lists the position and line-strength for each of 58 water-vapor lines near the primary wavelength. They extend from about 2141 cm⁻¹ to 2168 cm⁻¹. Only absorption lines from the H₂¹⁶O isotope are included, since it comprises 0.99729 of atmospheric water-vapor (Ref 16:6).

The absorption cross-section at 2154.6050 cm⁻¹ for each individual line can be calculated from equation (46). The value for the H₂O line half-width is taken to be 0.032 cm⁻¹ (Ref 16:20). The results are tabulated in Appendix H.

The total absorption cross-section of H₂O at sea-level is the sum of the individual cross-sections. Its value is calculated to be 4.435×10^{-24} cm² at 2154.6050 cm⁻¹.

The total absorption cross-section as a function of altitude can be calculated from this sea-level value using equation (52). The H₂O line that contributes most to the total cross-section is the one at 2154.710 cm⁻¹. The lower state energy for this line is given as 1821.599 cm⁻¹

(Ref 27:150). Therefore, this value should be used for E'' in the calculations. The resulting total cross-sections are tabulated in Appendix I.

The atmospheric extinction coefficient ϵ_{H_2O} , can now be calculated from equation (45). The H_2O number density is given in Appendix I, as is the total absorption cross-section. The resulting extinction coefficients are also listed in this appendix.

Calculation of T_A^2

The atmospheric transmission term T_A^2 , can now be determined. The value of T_A^2 over a 1 km vertical path at a range R from the lidar system is given by equation (33); where the contributions due to CO_2 , N_2O , and O_3 have been shown to be negligible. Equation (33) then becomes:

$$T_A^2(R) = \exp \left\{ -2 \left[\epsilon_R + \epsilon_M + \epsilon_{H_2O} + \epsilon_{CO_2} \right] \Delta R \right\} \quad (53)$$

where the tabulated values of the extinction coefficients are available in the relevant appendices. The resulting values of $T_A^2(R)$ at a wavelength of $2154.6050 \text{ cm}^{-1}$ are given in Appendix J.

The value of T_A^2/R , that is the two-way transmission over a path from 0 to a range R , is then given by equation (32). The tabulated values for this quantity are also available in Appendix J. Thus, one can easily determine from the tables that, at a range of 200 km (sea-level), the value of T_A^2/R is 0.6322.

Calculation of T_{co}^2

The transmission term T_{co}^2 , which is due solely to the R(2) line of CO, will be the dominant transmission term in the lidar equation. As such, its value must be known precisely. Since only a single absorption line is involved, the absorption cross-section at the primary wavelength can be calculated directly at each altitude using equations (26), (46), and (47). The line-strength at each altitude can be calculated from its sea-level value and equation (26), where E'' is calculated from the Dunham coefficients as $1093.12109 \text{ cm}^{-1}$. Then the line-width as a function of altitude can be determined using equation (47). Finally, the cross-section can be calculated from equation (46).

The CO R(2) line half-width at half-maximum has an experimentally measured value of 0.07 cm^{-1} at 1 atm (Ref 24:701).

The line-strengths, line-widths, and absorption cross-sections determined from the above equations are given in Appendix K.

Once the absorption cross-section is known, the two-way atmospheric transmission through a 1 km vertical path at a range R can be calculated from equation (29). The results are given in Appendix L.

The transmission term T_{co}^L/R for the path from 0 to a range R can then be determined from equation (28). These results are also given in Appendix L.

The Effects of Finite Laser Bandwidth

The lidar equation implicitly assumes that the transmitted laser radiation is monochromatic. This assumption is widely used in the literature, and is approximately true for most low-power laser systems

whose line-widths are generally 100 MHz (0.003 cm^{-1}) or less. Thus, their spectral width is much less than the width of a typical absorption line at sea-level, which is about 0.10 cm^{-1} . However, Korb et al. has pointed out that the effects of finite laser bandwidth can cause very large errors in range-resolved DIAL systems, and therefore they must be accurately accounted for (Ref 28:78).

This study assumes the use of high-power, pulsed CO_2 TEA laser sources whose nominal linewidth is about 2-3 GHz ($0.07\text{-}0.10 \text{ cm}^{-1}$). Therefore, the laser linewidth is of the same order of magnitude as the width of the absorption line being measured. Clearly, an attempt should be made to take the finite bandwidth of the laser into account.

In the Korb study, a correction was applied to experimentally measured lidar data using an iterative procedure to calculate the atmospheric transmission averaged over the laser line-width. The average transmission was given as:

$$\overline{T(\nu, z)} = \frac{\int_{\nu_i}^{\nu_f} h(\nu) e^{-z \int_{z_0}^z \mathcal{E}(\nu, z) dz} d\nu}{\int_{\nu_i}^{\nu_f} h(\nu) d\nu} \quad (54)$$

where $h(\nu)$ is the known distribution of laser power
 $\mathcal{E}(\nu, z)$ is the atmospheric extinction coefficient
 ν_i, ν_f are the wavenumber limits of the integration
 z_0, z is the path over which the calculation is performed

Recall equation (3) for the received power at the primary wavelength:

$$P_r(R) = P_o \epsilon K \left(\frac{c T_o}{2} \right) \beta_r(R) \left(\frac{A_r}{R^2} \right) T_A^2 \Big|_R \cdot T_{co}^2 \Big|_R \quad (3)$$

The first atmospheric transmission term, $T_A^2 \Big|_R$, was chosen to be relatively insensitive to wavelength, that is it does not contain any contributions from the central peak of an absorption line. Indeed, the only term in this equation that is extremely sensitive to wavelength is the second atmospheric transmission term, $T_{co}^2 \Big|_R$, which is just due to the single R(2) absorption line of CO. This will be the dominant transmission term since most of the absorption will be due to this one line.

This suggests that the finite bandwidth of the laser can be taken into account by considering the laser interaction with this line. That is, instead of calculating the term $T_{co}^2 \Big|_R$ as in equation (8), use a value averaged over the spectral width of the laser line. Since the parameters of the absorption line are functions of altitude, the average transmission must be calculated for each range-cell. Then, the total transmission for the path of interest can be obtained by taking a product of individual transmissions, as before.

Consider the average transmission function for one range-cell:

$$\overline{T_{co}^2(R)} = \frac{\int_{r_i}^{r_f} h(r) e^{-2 \int_0^{\Delta R} \epsilon(r,r) dr} dv}{\int_{r_i}^{r_f} h(r) dv} \quad (55)$$

In order to accurately calculate the average transmission for the cell, two functions must be known: the spectral line function of the laser pulse, $h(\nu)$; and the shape of the absorption line, $\mathcal{E}(\nu)$. In this study, both will be approximated by Lorentzian functions. The absorption line shape is Lorentzian for altitudes below 20 km, which is where most of the attenuation takes place, so the approximation should be reasonable. The spectral line shape of a CO₂ TEA laser is also Lorentzian, at least theoretically, so the approximation should be valid here, also (Ref 29:17).

Therefore, let:

$$h(\nu) = \frac{a \alpha_{\text{LASER}}}{(\nu - \nu_0)^2 + \alpha_{\text{LASER}}^2} \quad (56)$$

where α_{LASER} is the half-width of the laser line
 ν_0 is the wavenumber of the laser source
 ν is the wavenumber of the calculation
 a is a normalization constant, such that

$$\int_{-\infty}^{\infty} h(\nu) d\nu = 1$$

Also, let:

$$\mathcal{E}(\nu) = \left(\frac{S}{\pi} \right) \frac{\alpha N_{\text{co}}}{(\nu - \nu_i)^2 + \alpha^2} \quad (57)$$

where $\mathcal{E}(\nu)$ is the extinction coefficient due to the R(2) line
 α is the half-width of the absorption line
 S is the line-strength

N_{co} is the CO number density
 ν_1 is the center wavenumber for the R(2) line
 ν is the wavenumber for the calculation

Then, the average transmission can be calculated for each cell by numerically integrating the following:

$$\overline{T_{co}^2(R)} = \int_{\nu_i}^{\nu_f} \left[\frac{a \alpha_{LASER}}{(\nu - \nu_0)^2 + \alpha_{LASER}^2} \right] \exp \left\{ -2 \left[\frac{(S/\pi) N_{co} \alpha}{(\nu - \nu_1)^2 + \alpha^2} \right] \Delta R \right\} d\nu \quad (58)$$

The path integral has been replaced by a simple multiplication because the extinction coefficient is assumed constant across the range cell.

The average transmission values calculated from equation (58) are tabulated as a function of altitude in Appendix M. The product over a total path 0 to range R is also presented in Appendix M.

Equation (58) was numerically integrated by Simpson's rule on a digital computer. The absorption line parameters used were as given in Appendix K for the CO R(2) line centered at $\nu_1 = 2154.5960 \text{ cm}^{-1}$. The laser line was assumed to be centered at $\nu_0 = 2154.6050 \text{ cm}^{-1}$, with a line half-width of 0.05 cm^{-1} , which corresponds to a 3 GHz bandwidth laser source. The integration limits were from 2154.1 cm^{-1} to 2155.1 cm^{-1} . These limits represent the points where the laser distribution function decreases to about 1% of its peak value. The normalization constant used had the value $a = 0.339877562$. The integration step-size was selected to ensure an accuracy of four significant figures. At the higher altitudes where the absorption line-width is small, the step-size used was $6.67 \times 10^{-4} \text{ cm}^{-1}$.

Figures 2 and 3 contrast the spectral transmission functions at the two altitude extremes, sea-level and 30 km, respectively. In each figure the solid line is the spectral distribution function for the laser, $h(\nu)$; and the dashed line is the integrand in equation (58), which is just the differential transmission $\partial T / \partial \nu$. The dashed line may therefore be taken as an indication of the distribution of transmitted energy after it has twice traversed a 1 km path at that altitude. Note that at an altitude of 30 km, the separation between the absorption line center frequency and the laser center frequency is noticeable due to the narrow absorption line-width.

As stated earlier, this technique is not usually used when addressing problems of this type. Usually, a monochromatic source is assumed. Therefore, in the remainder of the report, the results will be given in terms of (1) a monochromatic source assumption, and (2) a finite bandwidth laser source assumption. In this way the results obtained using the two methods can be easily compared.

In this regard, it is convenient to introduce at this point an effective cross-section for the CO R(2) line that will preserve the integrity of the equations. Therefore, let σ_{eff} be defined such that the following equation is true:

$$\overline{T_{co}^2(R)} = \exp \left\{ -2 \left[N_{co}(R) \sigma_{eff}(R) \right] \Delta R \right\} \quad (59)$$

The effective cross-sections so defined are tabulated as a function of altitude in Appendix M.

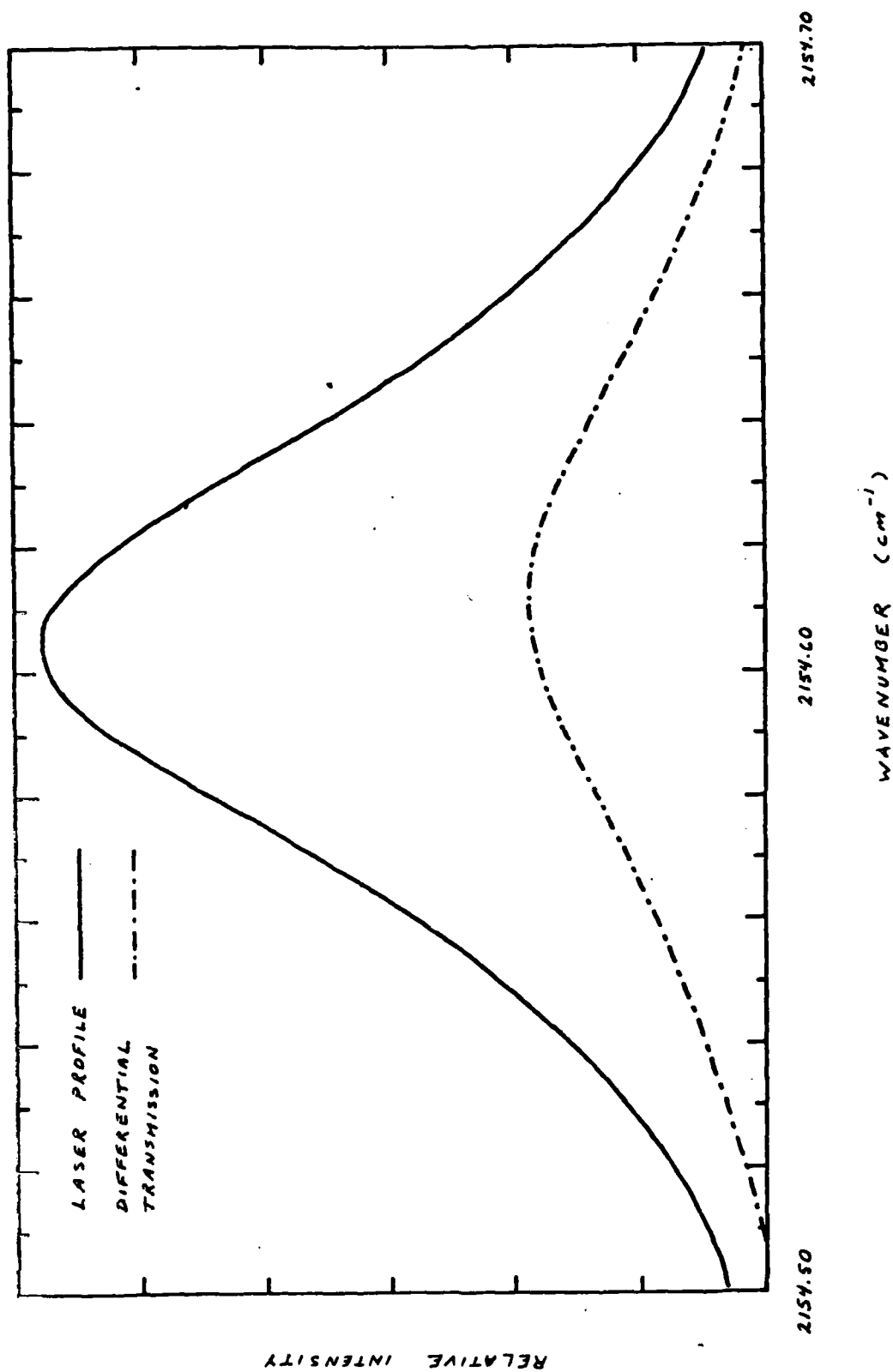


Figure 2. Atmospheric Transmission Averaged Over Laser Line-Width at Sea-Level.

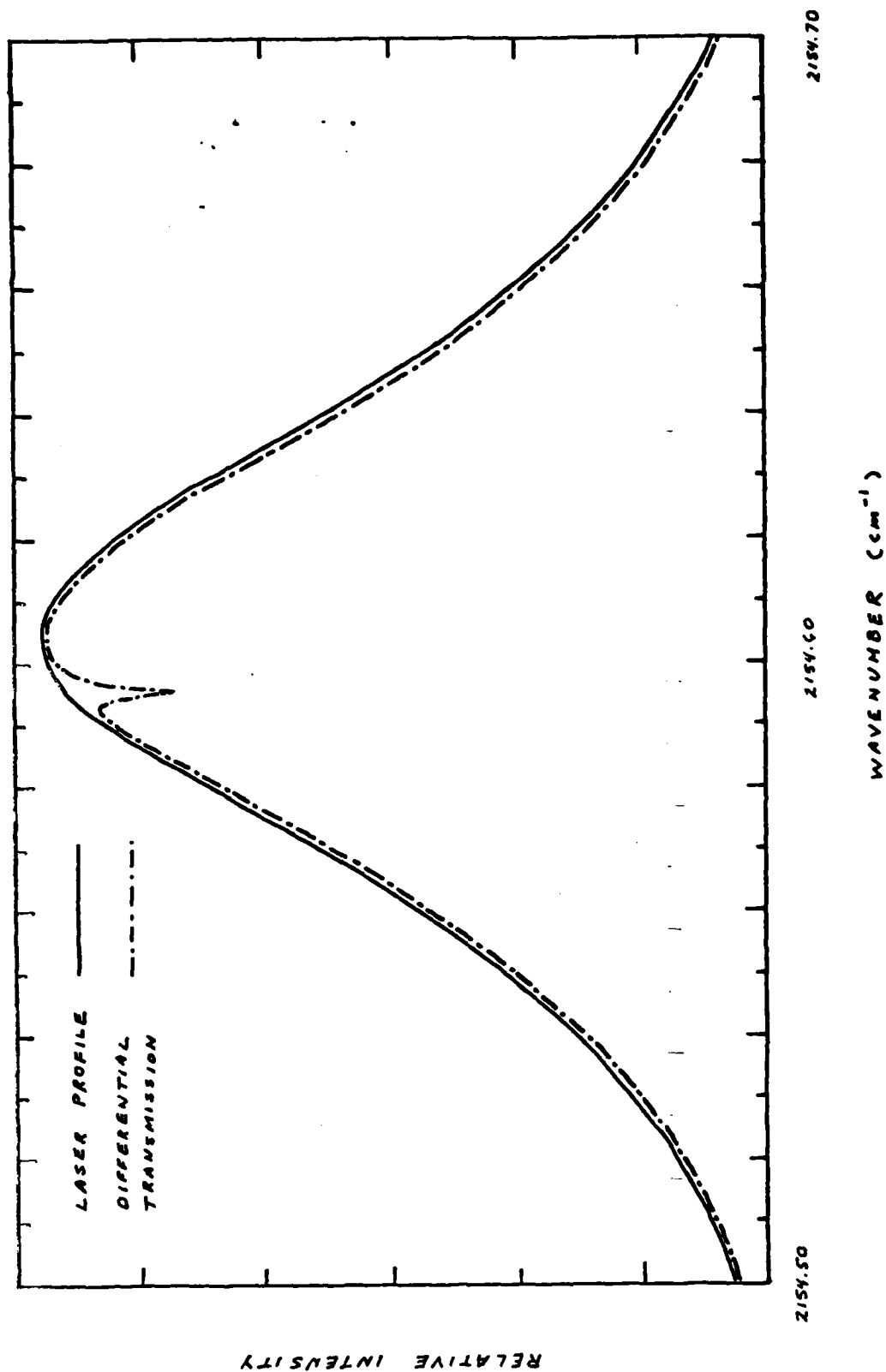


Figure 3. Atmospheric Transmission Averaged Over Laser Line-Width at 30 km.

V. Minimum Signal-to-Noise Requirements

The lidar equation gives the return signal power available to the signal processing portion of the receiver. The ratio of the return signal power level to the system noise power level is termed the power signal-to-noise ratio of the signal. Detection of the returning signal from a given range-cell implies that this ratio is at least one. Therefore, a basic requirement for system performance is that both the primary and the reference wavelength signal-to-noise ratios be greater than or equal to unity.

Another consideration for a DIAL lidar system is that the difference between the two signals must be measureable. In this study, the criterion that will be used is to require that the difference between the primary and reference signals be greater than or equal to the system noise level.

These signal-to-noise requirements can be formally stated as:

$$P_1 \geq P_N \quad (60)$$

$$P_2 \geq P_N \quad (61)$$

$$P_2 - P_1 \geq P_N \quad (62)$$

where

P_1 is the primary return signal power

P_2 is the reference return signal power

P_N is the receiver system noise power

These requirements can be written only in terms of the primary signal power by considering that P_1 and P_2 are related by equation (5). Since the transmission term T_{co}^2/R must always be less than or equal to one, equation (61) will be satisfied if equation (60) is. Therefore, using the definition $S_1 = P_1/P_N$, the two can be combined to require:

$$S_1 \geq 1 \quad (63)$$

Then, after solving equation (5) for P_2 and substituting the result into equation (62), equation (62) becomes:

$$S_1 \geq \frac{T_{co}^2/R}{1 - T_{co}^2/R} \quad (64)$$

An analysis shows that the right side of this inequality will be greater than or equal to one for all values of T_{co}^2/R greater than or equal to $1/2$. Therefore, the two signal-to-noise requirements can finally be restated as:

$$S_1 \geq 1 \quad \text{IF } T_{co}^2/R < 1/2 \quad (65)$$

$$S_1 \geq \frac{T_{co}^2/R}{1 - T_{co}^2/R} \quad \text{IF } T_{co}^2/R \geq 1/2 \quad (66)$$

These two inequalities determine the basic performance of the DIAL lidar system. Satisfaction of the first condition ensures that a measurement can be made over long paths where the absorption is high. Satisfaction of the second ensures that the ratio of the two signals is

measurable over paths where the absorption is low and the two signals are very nearly equal.

Equations (65) and (66) are formulated only in terms of quantities evaluated at the primary lidar wavelength. Therefore, the remainder of the study need only consider performance at this wavelength. If desired, reference wavelength parameters can easily be obtained using the relationship stated in equation (5).

The signal-to-noise requirements stated above can be reformulated into a set of required minimum signal-to-noise ratios as a function of altitude by evaluating the term T_{co}^2/R for each altitude (see Appendices L and M). The results are shown in Figure 4 for both the monochromatic source and the finite bandwidth source.

The results indicate that very large primary wavelength signal-to-noise ratios are necessary at the higher altitudes where the differential absorption is small.

An example here might serve to illuminate the situation. Consider the monochromatic source case at an altitude of 30 km ($R = 170$ km), where $T_{co}^2/R = 0.9972$. Suppose that the system noise level is 10^{-13} Watts. Then from Figure 4 the minimum required signal-to-noise ratio is 356. This equates to a primary return signal power of 356×10^{-13} Watts. From equation (5) the reference signal power is determined to be 357×10^{-13} Watts. The difference between the primary and reference signals is precisely 10^{-13} Watts, which is the system noise level. Thus, if the signal-to-noise ratio was anything less than 356, the difference between the two received signals would be less than

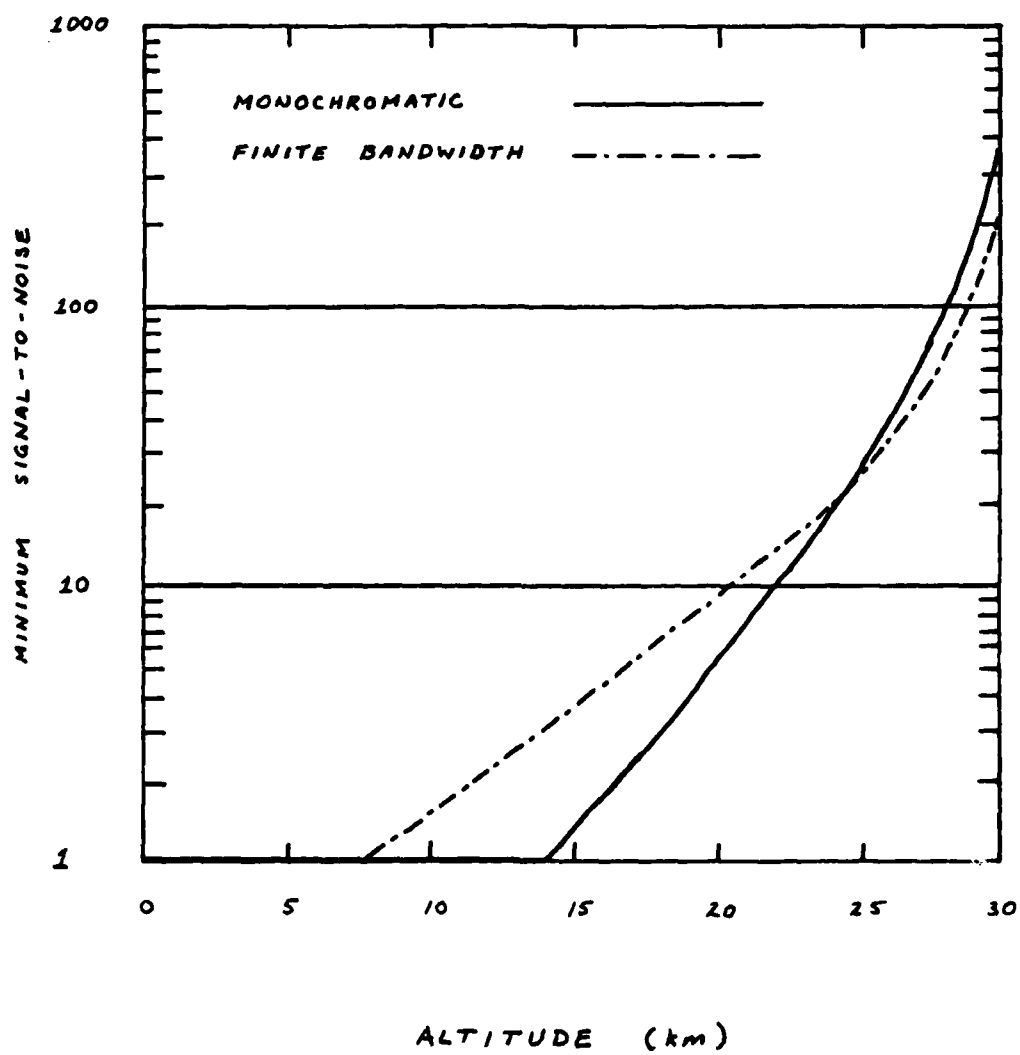


Figure 4. Minimum Signal-to-Noise Ratio Required.

the system noise level, and therefore the two would be indistinguishable.

This result is in agreement with what is generally stated for systems using the DIAL technique, namely that with current technology a signal difference ($\Delta P/P$) of the order of 1 percent is detectable (Ref 2:61).

VI. Detection of Lidar Return Signal

The measurement of carbon monoxide in the atmosphere using the differential absorption technique requires the sensitive detection of small amounts of infrared laser energy. There are two basic techniques that can be used: direct photon detection, and heterodyne detection. Direct photon detection is the most commonly used and also the simpler of the two to implement. Detection is achieved by directly converting incident photons into charge carriers. The amount of current produced by the device is then measured and related to the incident photon flux.

Heterodyne detection is generally much more sensitive than direct detection, but requires more complicated electronics and an additional laser source for the down-conversion process. The principle involved is identical to the more familiar heterodyne process used at microwave frequencies. Its implementation in the optical region is accomplished by combining the return signal with a laser local oscillator signal at the surface of a photomixer. The non-linear mixing process converts the incident signal to a lower frequency that can be amplified by conventional electronics.

On the surface it appears that heterodyne detection, with its superior sensitivity, should be chosen over direct detection. However, because of its relative simplicity, direct detection would be preferred if both techniques should provide adequate detection capability. Therefore, this study will address both direct and heterodyne detection schemes.

Direct Detection

Infrared detectors can be described by four main parameters: spectral coverage, response time, minimum detectable power, and operating temperature. For this study, the detector must provide adequate sensitivity at 4.64μ and have a response time of less than 6.67 microseconds, which is the integration time of the receiver. The detector which most nearly meets these requirements is the indium antimonide (InSb) photovoltaic infrared detector operating at a temperature of 77°K. Such detectors typically have a normalized detectivity of about $10^{11} \text{ cm Hz}^{1/2} \text{ W}^{-1}$ at 4.6μ with a response time of less than one microsecond (Ref 25:11-78). The detector parameters used in this study are given in the following table. They are for a commercially available Ford Aerospace and Communications InSb ISC-368 infrared detector, and are identical to those used in the study by Wank (Ref 4:60). The normalized detectivity quoted in the table is for an angular FOV of 120

Table IV

InSb ISC-368 Infrared Detector

| | |
|------------------------------|---|
| S_D (Sensitivity) | 2.0 A/W |
| D^* (Detectivity 120° FOV) | $8.6 \times 10^{10} \text{ cm Hz}^{1/2} \text{ W}^{-1}$ |
| A_D (Detector Area) | $2.827 \times 10^{-3} \text{ cm}^2$ |

degrees. The detectivity for a FOV of 10^{-4} radians can be calculated by considering a quantity called D^{**} , which is related to D^* , but is independent of the system FOV. For a flat-surfaced detector with circular

symmetry (Ref 30:45):

$$D^{**} = D^* \sin \theta_{1/2} \quad (67)$$

where $\theta_{1/2}$ is the half-angle FOV of the detector. Using this equation and the values in the table, $D^{**} = 7.448 \times 10^{10} \text{ cm Hz}^{1/2} \text{ sr}^{-1} \text{ W}^{-1}$. Then, D^* for a 10^{-4} radian FOV will be:

$$D^* = D^{**} / \sin \theta_{1/2} \quad (68)$$

where D^{**} is given above and $\theta_{1/2}$ is 5×10^{-5} radians. Therefore, the value of D^* corrected for FOV is $1.49 \times 10^{15} \text{ cm Hz}^{1/2} \text{ W}^{-1}$.

The power signal-to-noise ratio for a photovoltaic detector and amplifier combination is given by (Ref 31:69):

$$\frac{S}{N} = \frac{i_s^2}{2 e B (i_s + i_B + i_D) + \frac{4 k T_e B}{R_L}} \quad (69)$$

where

- i_s is the mean signal current
- i_B is the mean background current
- i_D is the mean dark-current
- e is the electron charge
- B is the electrical bandwidth of the system
- T_e is the effective temperature
- R_L is the load resistance
- k is the Boltzmann constant

The first three terms in the denominator are the mean-squared shot noise current from the signal, background, and dark-current, respectively.

The last term in the denominator is the mean-squared noise current due

to the amplifier electronics. Depending on which noise source gives the largest contribution, the detector is said to be photon, background, dark-current, or amplifier noise limited, respectively.

In order to address the performance of the detector, the background noise power must first be known.

Background Noise Power. There are three principle noise sources which contribute to the total background noise that will be seen by the detection system. They are:

1. Radiance from the earth
2. Radiance from the sun
3. Radiance from the sky

The thermal radiance from the earth can be estimated by assuming that the earth is a 300° blackbody with an emissivity of 0.85. Then, if the receiving telescope is pointed directly toward the earth, the background power will be:

$$P_B^e = W(\lambda) \Delta\lambda \Omega_{FOV} A_r T_\lambda K \quad (70)$$

| | | |
|-------|-----------------|---|
| where | $W(\lambda)$ | is the spectral radiance of the source in $W\text{ cm}^{-2}\text{ sr}^{-1}\text{ um}^{-1}$ |
| | $\Delta\lambda$ | is the wavelength interval under consideration in microns |
| | Ω_{FOV} | is the steradian FOV of the system |
| | A_r | is the area of the receiving optics in cm^2 |
| | T_λ | is the one-way atmospheric transmission |
| | K | is the efficiency of the receiving optics |

The wavelength interval is dependent upon the optical filtering used in the detection system. It must be wide enough to recover all of the laser energy, in this case about 3 GHz; yet small enough to provide adequate noise rejection. Commercially available interference filters can be used here, and a $\Delta\lambda$ of 0.01μ is reasonable (Ref 25:7-127). The wavelength interval used in the following calculations is centered at 4.640μ and extends from 4.635μ to 4.645μ . The one-way atmospheric transmission can be obtained from Appendices J, L, and M. For a monochromatic source $T_\lambda = 3.417 \times 10^{-2}$. For a finite source $T_\lambda = 1.783 \times 10^{-1}$. Using standard blackbody tables (Ref 32), $W(\lambda)\Delta\lambda$ is determined to be $1.535 \times 10^{-6} \text{ W cm}^{-2} \text{ sr}^{-1}$. Then using the values for A_r , K , and from Table I:

$$P_B^e = 9.706 \times 10^{-13} \text{ WATTS} \quad (\text{Monochromatic Source}) \quad (71)$$

$$P_B^e = 5.065 \times 10^{-12} \text{ WATTS} \quad (\text{Finite Bandwidth Source}) \quad (72)$$

The thermal radiance from the sun can be estimated by assuming that the sun is a blackbody source at 5900°K with an emissivity of 1.0. The receiving telescope is again assumed to be pointing directly at the earth. Energy from the sun must traverse the atmosphere, be reflected from the surface with some efficiency, and then traverse the atmosphere once more to enter the receiving optics. The background power from the sun will then be:

$$P_B^s = W(\lambda)\Delta\lambda \frac{A_s A_r \Omega_{rev}}{\pi R_{s-e}^2} \kappa r_e T_\lambda^2 \quad (73)$$

where

A_s is the projected area of the sun

R_{s-E} is the distance from the sun to the earth

r_e is the reflectivity of the earth

and all other parameters are as previously defined. The factor π^{-1} comes from the assumption that the earth is a lambertian reflector. Using the blackbody tables and the same $\Delta\lambda$ as before, $W(\lambda)\Delta\lambda = 4.302 \times 10^{-1} \text{ W cm}^{-2} \text{ sr}^{-1}$. Then, using the values from Table I; along with an $A_s = 1.52 \times 10^{18} \text{ m}^2$, $R_{s-E} = 1.49 \times 10^{11} \text{ m}$, and an $r_e = 0.15$; the background power from the sun is estimated to be:

$$P_B^s = 3.039 \times 10^{-14} \text{ WATTS} \quad (\text{Monochromatic Source}) \quad (74)$$

$$P_B^s = 8.275 \times 10^{-13} \text{ WATTS} \quad (\text{Finite Bandwidth Source}) \quad (75)$$

The thermal radiance from the sky can be estimated from experimental data by Bell (Ref 33:1316). He estimates that for a clear sky at 4.6μ and at an angle of 90° (vertical), $W(\lambda) = 2.0 \times 10^{-4} \text{ W cm}^{-2} \text{ sr}^{-1} \text{ u}^{-1}$. Using this information, the background power from the sky can be calculated from:

$$P_B^{sky} = W(\lambda) \Delta\lambda \Omega_{FOV} A_r K \quad (76)$$

where all quantities are as previously defined. Assuming that $W(\lambda)$ is constant over the small wavelength interval $\Delta\lambda$, $W(\lambda)\Delta\lambda = 2.0 \times 10^{-6} \text{ W cm}^{-2} \text{ sr}^{-1}$. The background power from the sky is then estimated to be:

$$P_B^{SKY} = 3.701 \times 10^{-11} \text{ WATTS} \quad (77)$$

The total background power can now be estimated, since:

$$P_B^{TOTAL} = P_B^e + P_B^s + P_B^{SKY} \quad (78)$$

The results are:

$$P_B^{TOTAL} = 3.801 \times 10^{-11} \text{ WATTS} \quad (\text{Monochromatic Source}) \quad (79)$$

$$P_B^{TOTAL} = 4.290 \times 10^{-11} \text{ WATTS} \quad (\text{Finite Bandwidth Source}) \quad (80)$$

Noise Equivalent Power. The purpose of this section is to calculate the noise equivalent power (NEP) for the direct detection case. The performance of the InSb direct photon detector is dependent upon the contributions of the various noise terms in the denominator of equation (69). One noise source, that associated with the background viewed by the detector, has already been estimated. It remains, then, to estimate the noise contributions due to signal current, dark-current, and the amplifier electronics.

The detector dark-current is related to the detector normalized detectivity by the following (Ref 34:1648):

$$D^* = \frac{S_D}{\sqrt{2 e (i_D / A_D)}} \quad (81)$$

Therefore, the dark-current will be:

$$i_D = \frac{S_D^2 A_D}{2 e D^{\#2}} \quad (82)$$

The dark-current calculated from this equation and the data in Table IV is 1.59×10^{-14} A.

The mean current associated with the background signal can be calculated from the product of the background noise power and the detector sensitivity. The mean background current is about 8.0×10^{-11} A. Since the background noise contribution is three orders of magnitude larger than that due to dark-current, the dark-current noise can be neglected in the following calculations.

The mean-squared noise current due to the amplifier and its associated electronics is given by the term $4kT_e B/R_L$, where: T_e is the effective temperature of the detector/amplifier combination, R_L is the load resistance, and B is the electrical bandwidth of the system. As stated earlier, this bandwidth must be adequate to support the 6.67 microsecond integration time of the receiver. For this study, a 1 MHz bandwidth is selected. This should provide the system with a conservatively chosen response time of about 1 microsecond, as well as adequate noise rejection.

A reasonable value for the effective temperature of a commercially available low-noise amplifier chain is $T_e = 250^\circ\text{K}$ (Ref 15:323).

The value of R_L is dependent upon the circuit capacitance and the electrical bandwidth of the system. A typical value for the circuit capacitance of a photodiode detector coupled with an amplifier is $C_d = 10$ picofarads. Then, since $B = 1/2 R_L C_d$, the load resistor must

have a value of about 10 k Ω in order to insure a bandwidth capability of 1 MHz.

Substitution of these values into the equation for the amplifier mean-squared noise current yields a value of $1.380 \times 10^{-18} \text{ A}^2$.

Equation (69) can now be written:

$$\frac{S}{N} = \frac{i_s^2}{2eB(i_s + i_B) + \frac{4kT_e B}{R_L}} \quad (83)$$

Then, incorporating the detector sensitivity into the equation with $i_s = P_S S_D$ and $i_B = P_B S_D$:

$$\frac{S}{N} = \frac{P_s^2 S_D^2}{2eB P_S S_D + 2eB P_B S_D + \frac{4kT_e B}{R_L}} \quad (84)$$

where P_S is the signal power, and P_B is the background noise power.

The system noise equivalent power is that value of signal power which will produce a power signal-to-noise ratio of unity. Equation (84) can then be solved to yield:

$$P_{NEP} = \frac{eB}{S_D} + \left[\frac{e^2 B^2}{S_D^2} + \frac{2eB P_B}{S_D} + \frac{4kT_e B}{R_L S_D^2} \right]^{1/2} \quad (85)$$

Since all of the required parameters are known or have been estimated, the system NEP for both the monochromatic laser source and the finite bandwidth laser source can be calculated. The results are:

$$P_{NEP} = 5.875 \times 10^{-10} \text{ WATTS} \quad (\text{Monochromatic Source}) \quad (86)$$

$$P_{NEP} = 5.875 \times 10^{-10} \text{ WATTS} \quad (\text{Finite Bandwidth Source}) \quad (87)$$

The results are the same for both cases because the dominant term in equation (85) is the one associated with the amplifier noise. Therefore, in the direct detection case, the system is shown to be amplifier noise limited.

Required Laser Power. Once the noise equivalent power of the system is known, the minimum signal-to-noise requirements developed earlier can be addressed to yield a performance assessment of the InSb detector. Consider that for any given range cell:

$$P_r(R) = (S/N)_{MIN} P_{NEP} \quad (88)$$

where $(S/N)_{MIN}$ is the required minimum signal-to-noise, and P_{NEP} is the system NEP. Then the basic lidar equation can be solved for the peak laser power required to achieve that minimum signal-to-noise ratio. That is, let:

$$P_o(R) = \frac{(S/N)_{MIN} P_{NEP}}{\epsilon K \left(\frac{c T_0}{2}\right) \beta(R) \left(\frac{A_r}{R^2}\right) T_A^2|_R \cdot T_{co}^2|_R} \quad (89)$$

The required laser power at each altitude is shown in Figure 5. Results are displayed for both the monochromatic source and the finite bandwidth source. The required laser energy (assuming a 100 ns pulse) is also shown.

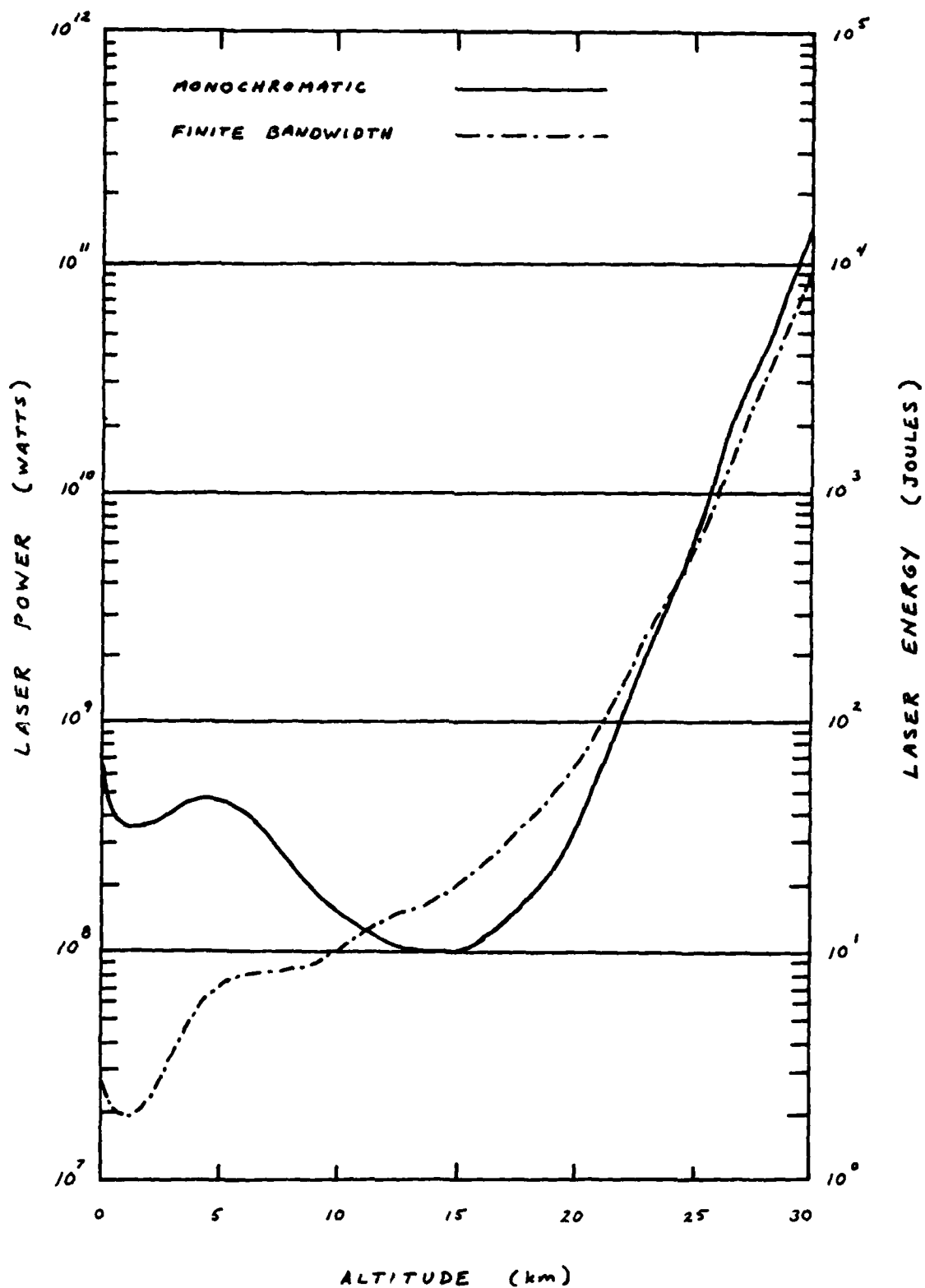


Figure 5. Laser Power Required - Direct Detection.

Heterodyne Detection

Heterodyne detection is the most sensitive technique for detecting low-power laser radiation in the infrared portion of the spectrum. However, the increase in sensitivity is not without its drawbacks, since heterodyne detection imposes stringent requirements on the system. These requirements are basically in the form of spatial and temporal coherence considerations that must be met in order to achieve the full benefits of the heterodyne process.

The basic heterodyne detection scheme is as follows (see Figure 6). Laser radiation is transmitted into the atmosphere and scattered off of molecules and particulates in a particular range cell. The returning photon flux is collected by the receiving optics and applied to the surface of a photomixer, where it is combined with the signal from a coherent laser local oscillator (L.O.). The local oscillator frequency is slightly offset from the signal frequency, and their difference is referred to as the intermediate frequency (IF) of the process. The IF signal contains the same information as the incoming optical signal, but at a frequency that is easily handled by conventional electronics. The IF or difference frequency is a product of the non-linear photomixing process, and the efficiency of this process determines, in large part, the sensitivity of the detector.

When the signal wavefront and the local oscillator wavefront arrive at the surface of the photomixer, they must be spatially coherent in order to achieve maximum conversion efficiency. This spatial coherence

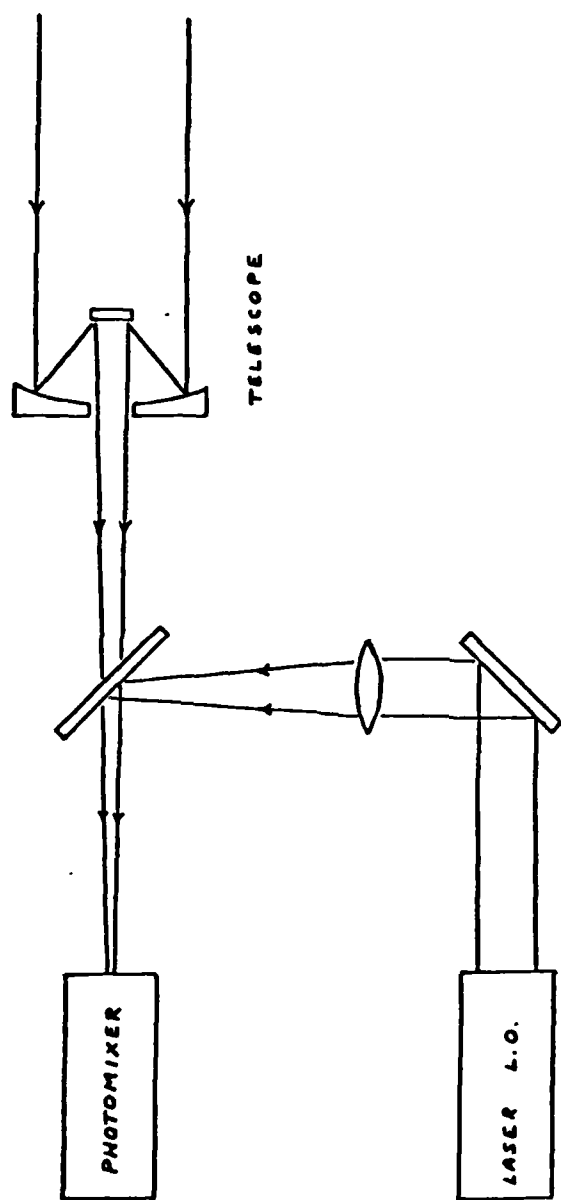


Figure 6. The Heterodyne Process.

requirement can be stated as (Ref 35:37-47):

$$\beta \leq \frac{\lambda}{\pi l} \quad (90)$$

where

β is the radian angle between the signal and local oscillator wavefronts

λ is the wavelength of the incoming signal

l is the distance over which the photo-mixing takes place, i.e. the diameter of the detector

This requirement may be interpreted as a basic limitation on the system FOV, where $\theta_{fov} \leq 2\beta$ if the L.O. signal is aligned with the optical axis of the system. For a wavelength of 4.64μ and a detector diameter of 1.0×10^{-3} m (Ref 35:37-47), β must be less than 1.48×10^{-3} radians. This leads to a system FOV requirement of less than 2.95×10^{-3} radians, which is easily met by the system under consideration.

There is one other spatial coherence requirement that must be addressed. The signal from a given scatter volume is constantly changing as the molecules and particles move about. It can be shown that the system receiving aperture must not be larger than the mean grain size in the scatter volume. For the system under consideration, the requirement is that the area of the receiving optics be less than or equal to the area of the transmit optics (Ref 2:67). Since the system in this study uses the same telescope for transmitting and receiving, this requirement is also met.

There are also temporal coherence criteria that must be met. They are addressed later in the study. At this point, it is convenient to

state that all the basic requirements for heterodyne detection can be satisfied by the system under consideration in this study.

Noise Equivalent Power. The basic limitation on the sensitivity of the direct photon detector was determined to be the amplifier noise. In heterodyne detection, amplifier noise and the other usual noise sources are not a problem because of the manner in which the signal is processed. For heterodyne detection, the power signal-to-noise ratio can be shown to be (Ref 35:37-37):

$$\frac{S}{N} = \frac{P_{Lo} P_s}{P_{Lo} P_N} \quad (91)$$

that is, the local oscillator signal raises both the signal level and the noise level. Therefore, amplifier noise and other noise sources can be overcome simply by raising the L.O. signal level.

The mean-squared shot-noise current due to the L.O. signal is:

$$i_s^2 = 2 e B \left[\frac{P_{Lo} \eta e}{h \nu} \right] \quad (92)$$

where η is the quantum efficiency of the photomixer. The quantity in brackets is just the mean L.O. signal current. If the L.O. is to be the dominant noise source, then:

$$i_s^2 > 2 e B (i_s + i_B) + \frac{4 k T_e B}{R_L} \quad (93)$$

The shot-noise current due to signal and background were determined to be much less than that due to the amplifier noise in the section on direct detection. Therefore, the first term can be neglected, and:

$$i_g^2 > \frac{4 k T e B}{R_L} \quad (94)$$

is all that is required. In practical terms, the required L.O. power is usually about 1 or 2 mW (Ref 15:314). Therefore, the requirement that the shot-noise from the L.O. be the dominant noise term is easily attained.

Assuming that the local oscillator power is sufficient, the signal-to-noise ratio can now be written:

$$\frac{S}{N} = \frac{i_s^2}{i_g^2} \quad (95)$$

where i_s^2 is the mean-squared signal current, which can be obtained from:

$$i_s = \frac{\sqrt{P_{Lo} P_s} \eta e}{h \nu} \quad (96)$$

Then, the signal-to-noise ratio becomes:

$$\frac{S}{N} = \frac{P_s}{2 h \nu B / \eta} \quad (97)$$

Equation (97) is the form in which the heterodyne signal-to-noise ratio is usually written. From this equation it is easy to see that the heterodyne noise equivalent power is given by:

$$P_{NEP} = \frac{2 h \nu B}{\eta} \quad (98)$$

The electrical bandwidth used in the heterodyne detection process is generally matched to the reciprocal of the laser output pulse duration (Ref 28:83). For a 100 nanosecond pulse, the bandwidth is 10^7 Hz. Using this figure for B, and a quantum efficiency of 0.5, the heterodyne NEP is calculated to be:

$$P_{NEP} = 1.714 \times 10^{-12} \text{ WATTS} \quad (99)$$

Heterodyne Signal-to-Noise Considerations. The signal-to-noise ratio given in equation (97) represents near quantum limited detection of the incoming signal. The large signal-to-noise ratios implied by this expression are attainable only if the received photon flux is totally coherent during the receiver integration time. In practice, the return signal will be coherent only over a time period equivalent to the laser pulse length. The system in this study is designed to integrate the return signal for much longer than this in order to achieve adequate sensitivity over very long ranges. This temporal coherence problem is referred to in the literature as "speckle noise", and is usually handled by considering the statistical nature of the return signal. The derivation used in this study follows closely that recommended by Rye (Ref 36: 3862).

Consider a system with an integration time that is long compared to the pulse duration. Then, the return signal may be thought of as being composed of a series of partially coherent pulses from various scatter points in the range cell being measured. If each such pulse is considered

to be an independent statistical sample, then the total number of such samples available during the integration process is just τ_a / τ_p , where τ_a is the receiver integration time, and τ_p is the laser pulse width. Rye shows that the mean-squared charge from the photomixer over one integration period is:

$$\langle g^2 \rangle = e^2 \eta \langle N_L \rangle (1 + 2 \eta \eta_N \delta h) \quad (100)$$

where $\delta h = \langle N_R \rangle / m$

Here; η is the quantum efficiency of the photomixer, η_N is the quantum efficiency of the heterodyne process, $\langle N_L \rangle$ is the photon count from the L.O. over the integration time, $\langle N_R \rangle$ is the received photon count over the same period, and m is the number of statistical samples τ_a / τ_p . He then defines the mean-squared charge due to the L.O. as $\langle g^2 \rangle_L = e^2 \eta \langle N_L \rangle$. Then, assuming that the sample values for q are Gaussian with zero mean, the signal-to-noise ratio available from a single sample can be shown to be:

$$\left(\frac{S}{N} \right)_1 = \frac{\langle g^2 \rangle - \langle g^2 \rangle_L}{[2 \langle g^2 \rangle^2 + 2 \langle g^2 \rangle_L^2]^{1/2}} = \frac{2 \eta \eta_N \delta h}{\{2 [1 + (1 + 2 \eta \eta_N \delta h)^2]\}^{1/2}} \quad (101)$$

This equation has the limiting values:

$$\left(\frac{S}{N} \right)_1 = \begin{cases} \frac{1}{\sqrt{2}} & \text{IF } 2 \eta \eta_N \delta h \gg 1 \\ \eta \eta_N \delta h & \text{IF } 2 \eta \eta_N \delta h \ll 1 \end{cases} \quad (102)$$

This shows that for any given sample, the achievable signal-to-noise ratio is less than one, so long as the photon count is sufficiently great. Note that the signal-to-noise ratio is proportional to the received photon flux only in the small signal regime. This leads to a concept of saturated signal-to-noise in the heterodyne process which can only be improved by increasing the number of samples m , or by averaging a number of laser shots. Then, the final heterodyne signal-to-noise ratio can be written:

$$\left(\frac{S}{N}\right)_H = (mM)^{1/2} \left(\frac{S}{N}\right)_1 \quad (103)$$

or:

$$\left(\frac{S}{N}\right)_H = \left[\frac{mM}{2} \right]^{1/2} \quad (104)$$

where m is the number of samples, and M is the number of laser shots averaged.

The requirement that $2\eta\eta_s S_h \gg 1$ is actually quite conservative. At a wavelength of 4.64μ one photon contains 4.3×10^{-20} joules, so over one pulse period the expected photon count at the system NEP is about four. Therefore, the system NEP remains a valid indicator of sensitivity.

Required Laser Power. In the heterodyne detection case, the attainable signal-to-noise ratio is independent of the laser transmitted power, so long as a sufficient photon count is maintained. As shown in the last section, the system NEP is an accurate indicator of photon

count. Therefore, the single-shot laser power required to meet the signal-to-noise criteria developed earlier can be calculated from:

$$P_i(R) = P_{NEP} \quad (105)$$

or:

$$P_o(R) = \frac{P_{NEP}}{\epsilon K \left(\frac{CT_0}{2} \right) \beta(R) \left(\frac{A_r}{R^2} \right) T_A / R \cdot T_{co} / R} \quad (106)$$

This equation is valid until the minimum signal-to-noise required exceeds that achievable with heterodyne detection of a single laser shot. Past this point, multiple laser shots must be averaged to make the measurement.

For the system under consideration, the value of $(S/N)_H$ is given by equation (104), where $M=1$ and $m=66.7$. The result is $(S/N)_H = 5.77$. Then, from Figure 4, the system can make single-shot measurements from sea-level to an altitude of 20 km for the monochromatic source assumption, and to an altitude of 17 km for the finite bandwidth source.

The required laser transmitter power levels for these altitudes are shown in Figure 7.

Error Analysis

Thus far, the criteria developed to assess the performance of the lidar system have been designed to insure that the primary and reference signals, and their difference, will be measureable. But it is not enough just to be able to make the measurement. The purpose of this

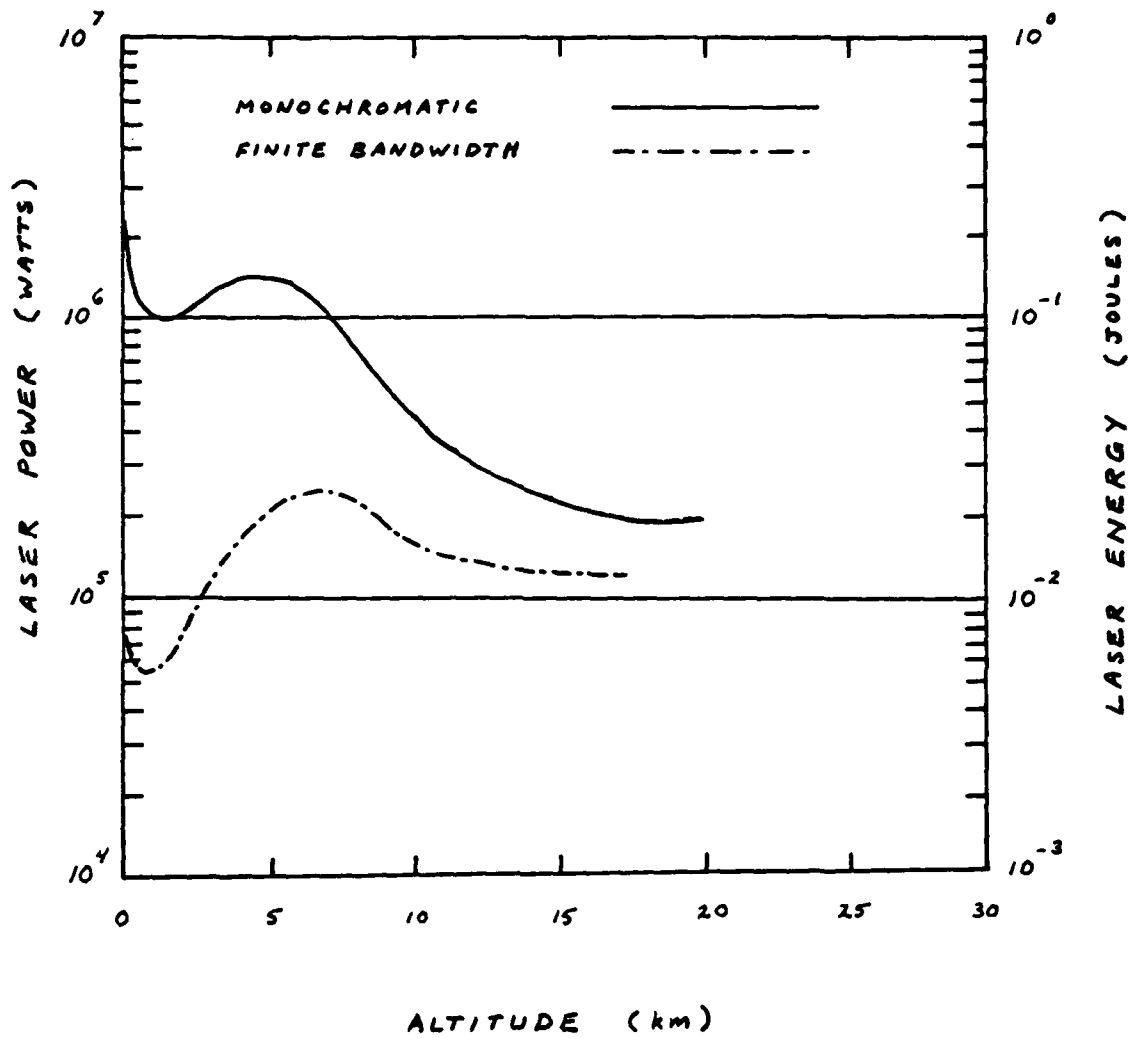


Figure 7. Laser Power Required - Heterodyne Detection.

section is to determine the accuracy with which the carbon monoxide number density can be measured.

Recall that the equation for the measured number density is:

$$\overline{N_{co}} = - \frac{1}{2 \Delta R \overline{\sigma_{co}}} \ln \left[\frac{P_1(R_2)}{P_2(R_2)} \cdot \frac{P_2(R_1)}{P_1(R_1)} \right] \quad (12)$$

The uncertainty in the measurement can be obtained, assuming independent error contributions, from the standard equation for propagation of errors:

$$[\Delta f(x_1, \dots, x_N)]^2 = \sum_{i=1}^N \left[\frac{\partial f}{\partial x_i} \Delta x_i \right]^2 \quad (107)$$

Then, assuming that the average absorption cross-section across the range cell is known exactly, the fractional uncertainty in the measurement can be shown to be:

$$\frac{\Delta N_{co}}{N_{co}} = \frac{\left\{ \left(\frac{\Delta P_2(R_2)}{P_2(R_2)} \right)^2 + \left(\frac{\Delta P_2(R_1)}{P_2(R_1)} \right)^2 + \left(\frac{\Delta P_1(R_2)}{P_1(R_2)} \right)^2 + \left(\frac{\Delta P_1(R_1)}{P_1(R_1)} \right)^2 \right\}^{1/2}}{- \ln \left[\frac{P_1(R_2)}{P_2(R_2)} \cdot \frac{P_2(R_1)}{P_1(R_1)} \right]} \quad (108)$$

A lower bound on the expected measurement error can be determined by assuming that the uncertainty in each individual power measurement is equal to the system noise level. Also, the equation's dependence on the

off-line measurements can be eliminated by using the relation $P_2(R) = P_1(R) / T_{co}^2 |_{R_1}$. Then the equation becomes:

$$\frac{\Delta N_{co}}{N_{co}} = \frac{\left\{ \left(\frac{T_{co}^2 |_{R_1}}{S_1} \right)^2 + \left(\frac{1}{S_2} \right)^2 + \left(\frac{1}{S_1} \right)^2 + \left(\frac{T_{co}^2 |_{R_2}}{S_2} \right)^2 \right\}^{1/2}}{-\ln \left[T_{co}^2 |_{R_2} / T_{co}^2 |_{R_1} \right]} \quad (109)$$

where

$S_{1,2}$ are the primary wavelength signal-to-noise ratios at ranges R_1 and R_2 , respectively

$T_{co}^2 |_{R_1}$ is the two-way atmospheric transmission to range R_1

$T_{co}^2 |_{R_2}$ is the two-way atmospheric transmission to range R_2

The above equation is exact, but can become tedious to work with because of the logarithmic dependence of the atmospheric transmission. The equation can be further simplified by using a few approximations. Consider that the two signal-to-noise ratios in the equation will be approximately equal, since they are for adjacent range cells. Also, the two transmission terms each must have a value between 0 and 1. Now, if $S_1 = S_2 = S$ and $T_{co}^2 |_{R_1} = T_{co}^2 |_{R_2} = 0$, the square-root term goes to $\sqrt{2}/S$. But, if $S_1 = S_2 = S$ and $T_{co}^2 |_{R_1} = T_{co}^2 |_{R_2} = 1$, then the square-root term goes to $2/S$. Finally, consider that the ratio $T_{co}^2 |_{R_2} / T_{co}^2 |_{R_1}$ is just $T_{co}^2(R_2)$. The above considerations suggest that, to a good approximation, the fractional uncertainty in the measurement at a range R can be written:

$$\frac{\Delta N_{co}}{N_{co}} = - \frac{1}{S \ln [T_{co}^2(R)]} \quad (110)$$

where

S is the power signal-to-noise at range R

$T_{co}^2(R)$ is the two-way atmospheric transmission through a 1 km vertical path at range R

This result is intuitively satisfying, since it takes into account the two limiting factors in any such measurement. First, the signal-to-noise ratio must be sufficiently high; and second, the absorption in the range cell must be great enough that the difference in transmission between adjacent cells can be accurately determined.

VII. Performance Analysis / 1 Joule Laser with Heterodyne Detection

The final system configuration selected for a performance analysis utilizes a 1 joule/pulse CO₂ TEA laser at each wavelength, and the heterodyne detection technique. A lidar system with these characteristics is well within the state-of-the-art and most of the components are commercially available. A summary of the major system parameters is given in the following table.

Table V

Lidar System Parameters

| | |
|------------------------------|-----------------------------|
| Primary (on-line) wavelength | 2154.6050 cm ⁻¹ |
| Reference wavelength | 2143.7674 cm ⁻¹ |
| Spectral linewidth | 0.10 cm ⁻¹ |
| Laser repetition rate | 100 Hz |
| Laser pulse duration | 100 ns |
| System NEP | 1.714 x 10 ⁻¹² W |
| Operational altitude | 200 km |

Assuming a 100 Hz repetition rate and a 20% overall efficiency for both the primary and reference lasers, the total average power required for the system should be on the order of 1 kilowatt. This is well within the limits set for the space shuttle (Ref 2:88).

Return Signal Power

The return signal power can be calculated using the basic lidar equation and the atmospheric data found in the various appendices. The value for P_0 can be calculated by dividing the laser pulse energy by the pulse duration. For this system the peak pulse power is 10^7 Watts. The atmospheric transmission term τ_{co}^2 / R should be obtained from Appendix M, since the laser source is assumed to have an output linewidth of about 3 GHz.

The results of these calculations are shown as a function of altitude above sea-level in Figure 8. As can be seen from the figure, the return signal power levels are well above the system NEP across the entire altitude spectrum.

Signal-to-Noise Ratio / Multiple Shots

Even though the return signal power levels are well above noise, the single-shot signal-to-noise ratio for the system is limited to 5.77 by the nature of the heterodyne process. This limits the altitude regime where measurements can be made to from sea-level to about 13 km. In order to meet the larger signal-to-noise requirements needed at the higher altitudes, successive laser shots must be averaged. The improvement in signal-to-noise goes as the square-root of the number of pulses averaged, as shown in equation (104). However, shot-averaging will also effect the spatial resolution of the measurements. At a 200 km orbital altitude the velocity of the space shuttle is about 7 km/s (Ref 2:78).

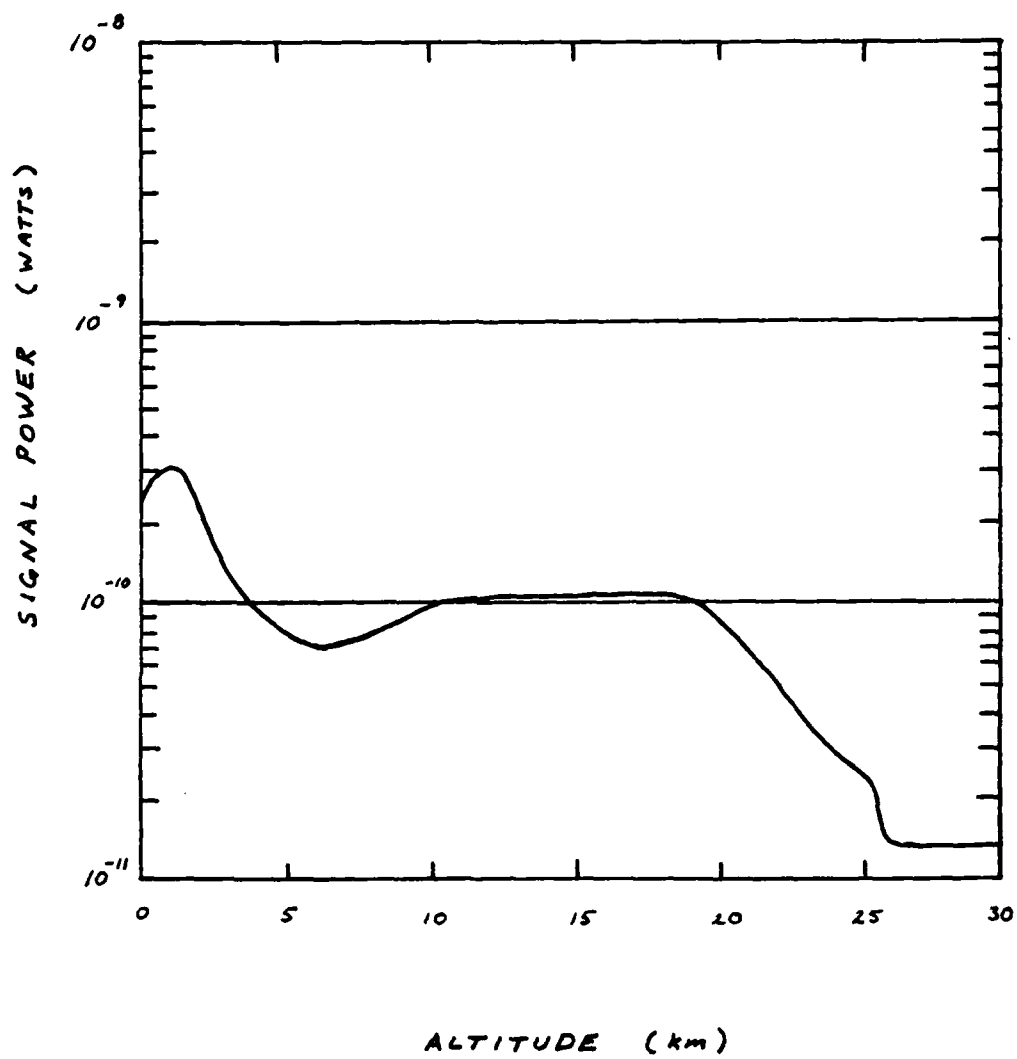


Figure 8. Return Signal Power - 1 Joule System.

Thus, if 100 pulses are averaged at a laser repetition rate of 100 Hz, the horizontal resolution is increased from about 70 meters to 7 km. Considering the large volume of the earth's atmosphere and the vertical resolution of 1 km, a horizontal resolution of 7 km is easily accommodated.

Assuming that 100 laser shots are averaged for each measurement, the heterodyne signal-to-noise ratio is increased by a factor of ten to 57.7. Then from Figure 4 the system should be able to make measurements from sea-level to an altitude of about 27 km.

The measurement accuracy is given by equation (110), and the results are shown as a function of altitude in Figure 9. They indicate that, although the system can make measurements to 27 km, the accuracy will not be good enough to provide useful data above an altitude of perhaps 15 km (50% error point). The reader is cautioned that the errors shown are approximate and should only be used as a general indication of system performance.

Performance Envelope

Thus far, the system performance has been measured against the a priori vertical profile of CO concentration established at the outset of the study. The atmospheric transmission parameters were all calculated based on this particular profile. Suppose the question is posed: how much or how little CO can be detected at any particular altitude? This question can be answered, but only within certain constraints. First of all, the measured concentration at a particular altitude depends on the

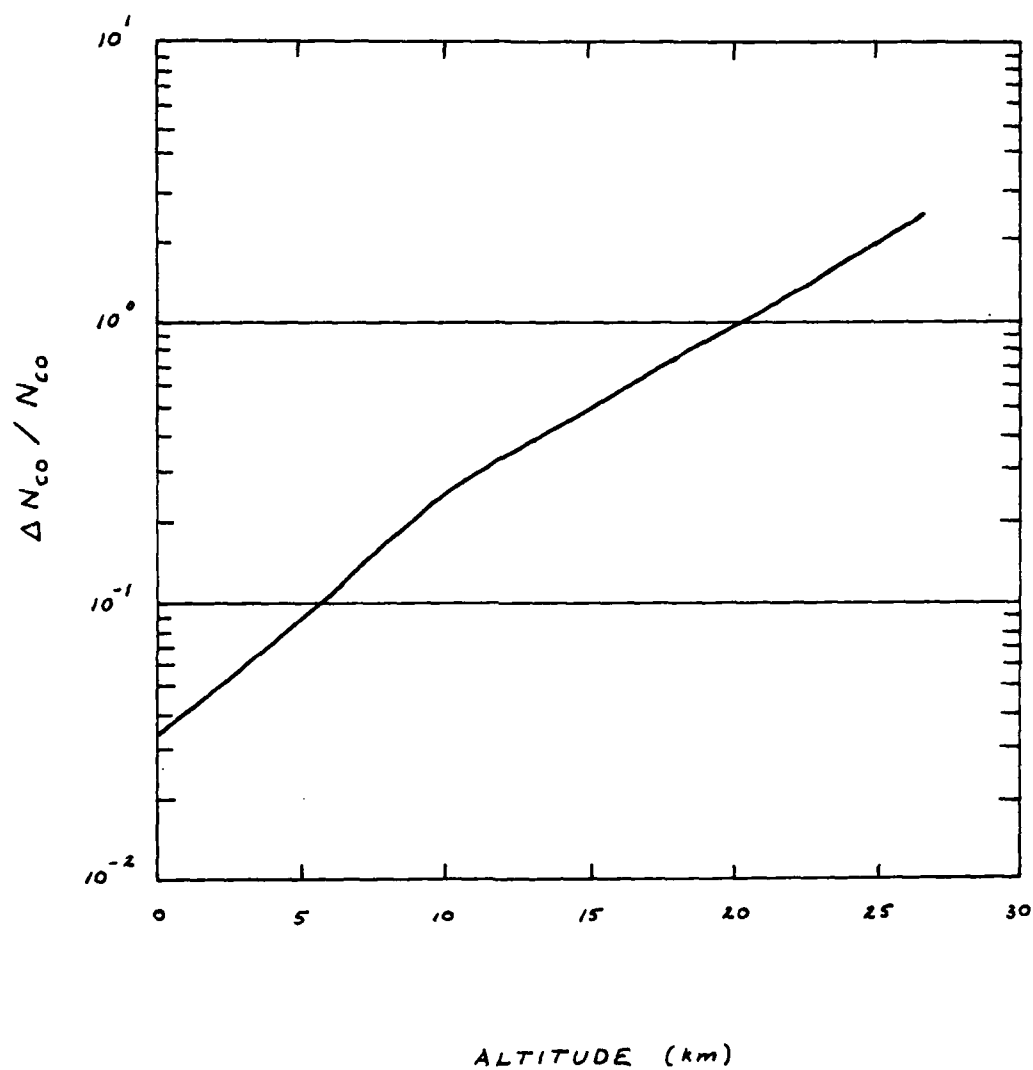


Figure 9. Measurement Error - 1 Joule System / 100 Shots.

CO concentration in the intervening layers. That is, the system obtains a measurement by comparing the returns from two adjacent range cells; and these returns are a function of the CO density along the entire vertical path from the shuttle to the range cell of interest. The approach that will be used here, is that the CO mixing ratio is fixed at 0.075 ppmv at all altitudes except in the range cell being analyzed. This corresponds to an assumption that a large gradient in the CO density profile exists at a certain altitude. The system capability to measure such a gradient is then of interest.

The maximum amount of CO that can be measured will be determined by "pump depletion"; that is, the CO number density is so great that most of the laser power is absorbed, and the return signal is reduced to the system noise level. Then the maximum amount of CO that can be detected can be calculated from the following:

$$P_i(R) = P_{NEP} \quad (111)$$

or:

$$T_{CO}^2 \Big|_R = \frac{P_{NEP}}{P_o \in K \left(\frac{cT_0}{2} \right) \beta(R) \left(\frac{A_r}{R^2} \right) T_A^2 \Big|_R} \quad (112)$$

and then, since:

$$T_{CO}^2 \Big|_R = T_{CO}^2 \Big|_{R-1} \cdot T_{CO}^2(R) \quad (113)$$

one finally obtains:

$$T_{CO}^2(R) = \frac{P_{NEP}}{P_o \in K \left(\frac{cT_0}{2} \right) \beta(R) \left(\frac{A_r}{R^2} \right) T_A^2 \Big|_R \cdot T_{CO}^2 \Big|_{R-1}} \quad (114)$$

AD-A164 271 DETECTION OF ATMOSPHERIC CARBON MONOXIDE FROM A

2/2

UNCLASSIFIED

SHUTTLE-BORNE LIDAR(U) AIR FORCE INST OF TECH
WRIGHT-PATTERSON AFB OH SCHOOL OF ENGINEERING

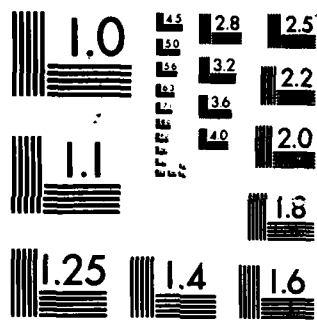
F/G 4/1

NL

END

FILMED

671C



MICROCOPY RESOLUTION TEST CHART
NATIONAL BUREAU OF STANDARDS-1963-A

Once the transmission in the range cell is calculated, it is a simple matter to obtain the maximum number density:

$$N_{co}^{MAX} = - \frac{1}{2 \nabla(R) \Delta R} \ln [T_{co}^2(R)] \quad (115)$$

where the argument of the natural logarithm is given by equation (114) above. Here, $\Delta R = 1$ km and $\nabla(R)$ is the effective cross-section given in Appendix M. An effective cross-section must be used because of the finite bandwidth of the laser. It should be noted that this analysis neglects the small change in T_A^2 due to the additional CO.

The minimum value of CO that can be detected depends on the difference in transmission between two adjacent range cells that can be accurately measured. Recall that the fractional uncertainty in the number density measurement is given approximately by:

$$\frac{\Delta N_{co}}{N_{co}} = - \frac{1}{S \ln [T_{co}^2(R)]} \quad (116)$$

then, for any given uncertainty, the transmission across the range cell must be:

$$T_{co}^2(R) = \exp \left\{ - \frac{1}{S (\Delta N_{co} / N_{co})} \right\} \quad (116)$$

A little thought will show that this value of $T_{co}^2(R)$ represents the maximum transmission (hence, the minimum absorption) that can be measured with the stated uncertainty. Then, the minimum number density that can be measured in the range cell becomes:

$$N_{co}^{MIN} = - \frac{1}{2 \Delta R \nabla(R)} \ln [T_{co}^2(R)] \quad (117)$$

where the argument of the natural logarithm is given by equation (116) above. This leads to:

$$N_{co}^{MIN} = \frac{1}{2 \nabla(R) \Delta R S (\Delta N_{co} / N_{co})} \quad (118)$$

The minimum number density that can be detected is then a function of how accurate the measurements must be.

Using equations (115) and (118), a performance envelope can be constructed for the system under consideration. Figure 10 shows the expected performance as a function of altitude. The standard atmosphere profile of CO number density is shown for reference. Once again, note that the minimum and maximum number densities that can be measured are based on the assumption that a standard CO density profile exists in the atmosphere between the shuttle and the range cell of interest.

Detection of "Hot" CO

Although the primary function of a lidar carbon monoxide detection system in space would be to measure and characterize the atmospheric CO budget, a secondary function might be the detection of carbon monoxide "hot" spots on or near the surface of the earth. Such "hot" CO emissions might be from a factory stack or perhaps from an area where

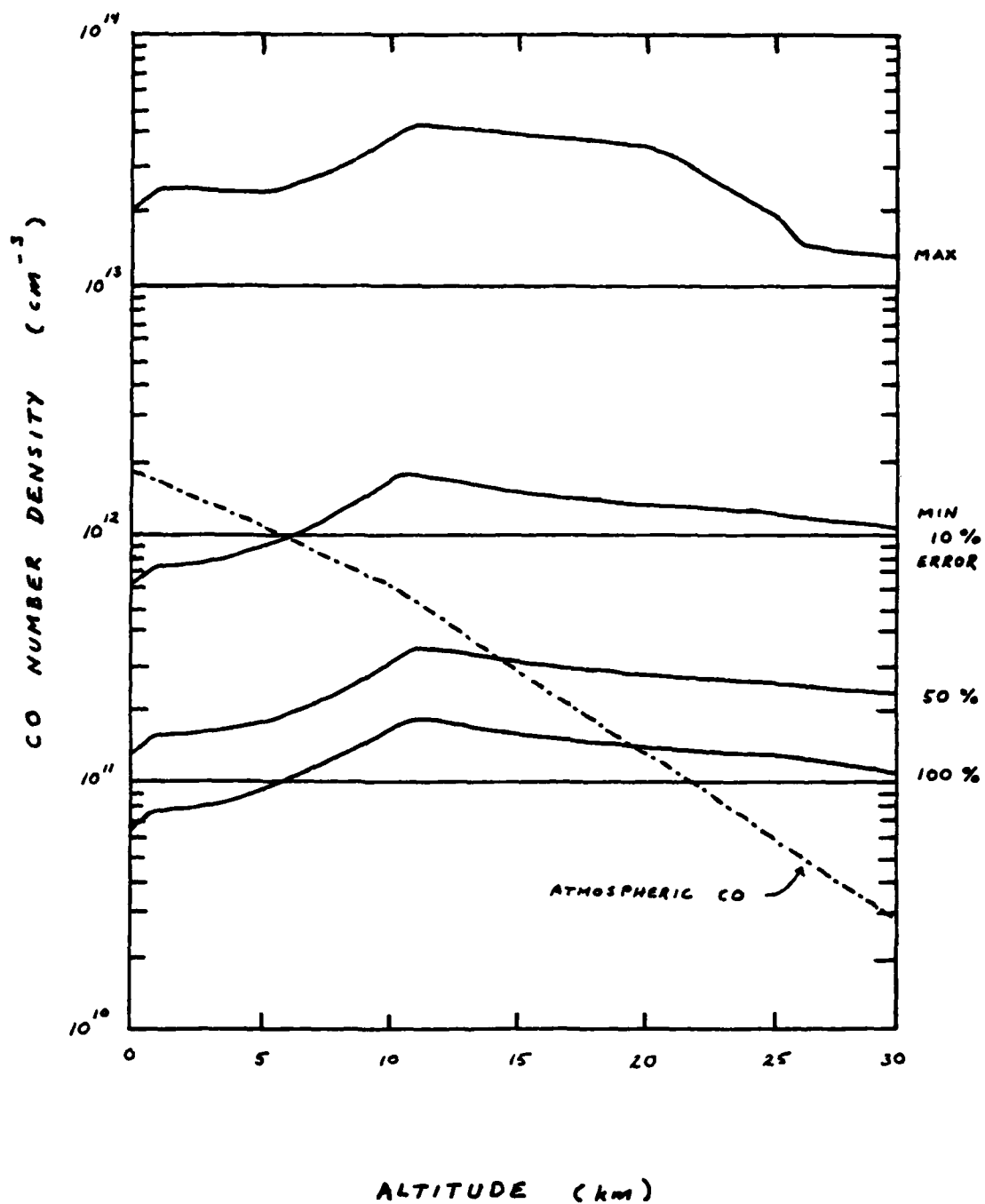


Figure 10. Performance Envelope - 1 Joule System.

the automobile density is extremely high. Another source might be the exhaust plumes from gas-turbine or rocket engines.

These emissions would differ from the standard atmospheric CO content in that the temperature of the molecules would be higher than ambient. The range of temperatures considered in this study is from 400°K to 1000°K. This range should be adequate to describe the phenomena of interest.

A detailed analysis of system capabilities in this area is beyond the scope of this thesis. However, a general idea of system performance can be obtained if several assumptions are made:

1. That the laser illuminates a uniform volume of "hot" CO .
2. That the "hot" CO has diffused to the point where the ambient pressure is valid.
3. That the "hot" CO is confined to an altitude of less than 2 km.
4. That the "hot" CO is present only in the range cell under consideration.

If these assumptions are made, then the maximum "hot" CO number density that can be detected will be that value of N_{HCO} which will reduce the return signal power to the system noise level. The return signal without the "hot" CO has already been calculated and is available from Figure 8. Then the return signal power with the "hot" CO will be:

$$P'_i(R) = P_i(R) T_{HCO}^2(R) \quad (119)$$

where: $P_i(R)$ is the return power without the "hot" CO
 $T_{HCO}^2(R)$ is the two-way atmospheric transmission due to "hot" CO

This equation can be solved for $T_{HCO}^2(R)$ for the case where $P_i(R)$ equals the system noise power:

$$T_{HCO}^2(R) = \frac{P_{NEP}}{P_i(R)} \quad (120)$$

but:

$$T_{HCO}^2(R) = \exp \left\{ -2 N_{HCO} \nabla_{HCO} \Delta R \right\} \quad (121)$$

then, the maximum "hot" CO number density can be written:

$$N_{HCO}^{MAX} = - \frac{1}{2 \nabla_{HCO} \Delta R} \ln \left[P_{NEP} / P_i(R) \right] \quad (122)$$

where ∇_{HCO} is the total absorption cross-section due to "hot" CO.

In order to calculate the maximum "hot" CO density that can be detected, the total absorption cross-section for the "hot" CO must be calculated. Because of the manner in which the Lidar equation was written, two separate cross-sections contribute to this total; the cross-section due to the R(2) line of CO, and the cross-section due to all other nearby CO lines. However, the cross-section due to the R(2) line will dominate by at least two orders of magnitude, and the other term can be neglected. Then, equations (26), (46), and (47) can be used to calculate the "hot" CO cross-section, which is tabulated as a function

of altitude and temperature in Table VI.

The maximum number density that can be detected can now be calculated from equation (122). These results are also given in Table VI.

It should be remembered that the calculated maximum number density is in addition to the existing CO number density at the altitude of interest. For this reason, it makes little sense to investigate the minimum number density, since the standard CO content is already well above the system threshold.

Table VI
Heterodyne Detection of Hot CO

| h | T (°K) | $\nabla_{HCO} \text{ (cm}^2\text{)}$ | $N_{HCO}^{MAX} \text{ (cm}^{-3}\text{)}$ |
|------|--------|--------------------------------------|--|
| 0 km | 400 | 7.949×10^{-18} | 3.040×10^{12} |
| | 500 | 1.544×10^{-17} | 1.565×10^{12} |
| | 600 | 2.381×10^{-17} | 1.015×10^{12} |
| | 700 | 3.148×10^{-17} | 7.677×10^{11} |
| | 800 | 3.882×10^{-17} | 6.226×10^{11} |
| | 900 | 4.585×10^{-17} | 5.271×10^{11} |
| | 1000 | 5.147×10^{-17} | 4.696×10^{11} |
| 1 km | 400 | 8.943×10^{-18} | 2.888×10^{12} |
| | 500 | 1.725×10^{-17} | 1.497×10^{12} |
| | 600 | 2.631×10^{-17} | 9.816×10^{11} |
| | 700 | 3.578×10^{-17} | 7.218×10^{11} |
| | 800 | 4.342×10^{-17} | 5.948×10^{11} |
| | 900 | 5.038×10^{-17} | 5.126×10^{11} |
| | 1000 | 5.677×10^{-17} | 4.549×10^{11} |
| 2 km | 400 | 1.001×10^{-17} | 2.426×10^{12} |
| | 500 | 1.951×10^{-17} | 1.245×10^{12} |
| | 600 | 2.936×10^{-17} | 8.270×10^{11} |
| | 700 | 3.931×10^{-17} | 6.177×10^{11} |
| | 800 | 4.915×10^{-17} | 4.940×10^{11} |
| | 900 | 5.733×10^{-17} | 4.235×10^{11} |
| | 1000 | 6.317×10^{-17} | 3.844×10^{11} |

VIII. Conclusions and Recommendations

Conclusions

On the basis of the analysis presented in this report, the following conclusions are made:

1. A range-resolved DIAL lidar system on board the Space Shuttle can be used to measure CO concentrations in the troposphere, but stratospheric measurements will be marginal due to large measurement errors.
2. Heterodyne detection of the return signal is required. Direct detection sensitivity was found to be unsatisfactory due to thermal noise in the detection system.
3. Of the major interfering species in the atmosphere at 4.64 (carbon dioxide, nitrous oxide, ozone, and water-vapor), only water-vapor provides a significant contribution to the extinction coefficient.
4. Addition of hot CO near the ground can be detected up to a maximum concentration of about 10^{12} cm^{-3} depending on the altitude and temperature.

Recommendations

Based on the results of this thesis the following recommendations are made:

1. A follow-on study be conducted to determine the sensitivity of the results presented herein to the atmosphere model used. In particular, the system sensitivity to changes in the water-vapor profile should be addressed, since the system will be required to make measurements over large ocean areas.
2. A follow-on study concerning detection of hot gases near the earth's surface should be conducted. This study and the one by Wank both conclude that a DIAL system in orbit can provide a detection capability for such gases. It would appear that such a system could be quite effective in locating and characterizing emissions from a large industrial complex or the exhaust plumes of gas turbine or rocket engines.

Bibliography

1. Browell, Edward V. et al. Shuttle Atmospheric Lidar Research Program. NASA SP-433. Washington, DC: Langley Research Center, NASA, 1979.
2. Englisch, W. et al. Multidisciplinary Lidar System in Spacelab for Application to Atmospheric Physics and Remote Sensing. Paris, France: European Space Agency, December 1977.
3. Kweder, Glen C. Remote Sensing of Gases Using Lidar Resonance Scattering Techniques from the Space Shuttle. MS Thesis. Wright-Patterson AFB, Ohio: School of Engineering, Air Force Institute of Technology, December 1981. (AD-A115-627)
4. Wank, Robert H. Detection of Atmospheric Carbon Dioxide from a Shuttle-Borne Lidar. MS Thesis. Wright-Patterson AFB, Ohio: School of Engineering, Air Force Institute of Technology, December 1982.
5. Ku, R.T., E.D. Hinkley, and J.O. Sample. "Long-Path Monitoring of Atmospheric Carbon Monoxide with a Tunable-Diode Laser System," Applied Optics, 14(4): 854-861 (1975).
6. Seiler, W. and C. Junge. "Carbon Monoxide in the Atmosphere," Journal of Geophysical Research, 75: 2217-2226 (1970).
7. Junge, C., W. Seiler, and P. Warneck. "The Atmospheric CO Budget," Journal of Geophysical Research, 76: 2866-2879 (1971).
8. Killinger, D.K., N. Menyuk, and W.E. DeFeo. "Remote Sensing of CO Using Frequency-Doubled CO₂ Laser Radiation," Applied Physics Letters, 36(6): 402-405 (1980).
9. United States Committee on Extension to the Standard Atmosphere. U.S. Standard Atmosphere, 1976. Washington, DC: NOAA, NASA, USAF, October 1976.
10. McClatchey, R.A. et al. Optical Properties of the Atmosphere, Third Edition. Air Force Cambridge Research Laboratories, August 1972. (AD-A753-075)
11. Byer, R.L. and Helge Kildal. "Comparison of Laser Methods for the Remote Detection of Atmospheric Pollutants," Proceedings of the IEEE, 59(12): 1644-1663 (1971).
12. Remsburg, E.E. and L.L. Gordley. "Analysis of Differential Absorption Lidar from the Space Shuttle," Applied Optics, 17(4): 624-630 (1978).

13. Pressley, R.J. ed. CRC Handbook of Lasers. Cleveland, Ohio: Chemical Rubber Company, 1971.
14. Kaminow, I.P. and A.E. Siegman, eds. Laser Devices and Applications. New York, N.Y.: IEEE Press, 1973.
15. Hinkley, E.D., ed. "Laser Monitoring of the Atmosphere," Topics in Applied Physics, Volume 14. Berlin, Heidelberg, New York: Springer Verlag, 1976.
16. McClatchey, R.A. Atmospheric Absorption Line Parameter Compilation. AFCRL-TR-73-0096. L.G. Hanscom Field, Bedford, Massachusetts: Air Force Cambridge Research Laboratories, January 1973.
17. Mantz, A.W. et al. "CO Laser Spectra Studied with a 10-meter Vacuum Infrared Grating Spectrograph," Journal of Molecular Spectroscopy, 35: 325-328 (1970).
18. Herzberg, G. Spectra of Diatomic Molecules, Second Edition. New York, N.Y.: Van Nostrand Reinhold Co., 1950.
19. Todd, T.R. et al. "Infrared Emission of CO," Journal of Molecular Spectroscopy, 62: 201-227 (1976).
20. Rothman, L.S. "AFGL Atmospheric Absorption Line Parameter Compilation: 1980 Version," Applied Optics, 20(5): 791-795 (1981).
21. McClatchey, R.A. "Optical Modelling of the Atmosphere," Agard Conference Proceedings, No. 183 on Optical Propagation in the Atmosphere. NATO, May 1976.
22. Shettle, E.P. and R.W. Fenn. "Models of the Atmospheric Aerosols and Their Optical Properties," Agard Conference Proceedings, No. 183 on Optical Propagation in the Atmosphere. NATO, May 1976.
23. Elterman, Louis. "Parameters for Attenuation in the Atmospheric Windows for Fifteen Wavelengths," Applied Optics, 3(6): 745-749 (1964).
24. Bouanich, J.P. and C. Haeusler. "Linewidths of Carbon Monoxide Self-Broadening and Broadened by Argon and Nitrogen," Journal of Quantitative Spectroscopy and Radiative Transfer, 12: 695-702 (1972).
25. Environmental Research Institute of Michigan. The Infrared Handbook, edited by W.L. Wolf and G.J. Zissis. Washington DC: Office of Naval Research, 1978.
26. Maki, A.G. "High-Resolution Infrared Spectrum of the $\nu_1 + \nu_3$ Band of Ozone," Journal of Molecular Spectroscopy, 57: 416-427 (1975).

27. Flaud, J.M. and C. Camy-Peyret. Water-vapour Line Parameters From Microwave to Medium Infrared: (And Intensities Between 0 and 4350 cm^{-1}). New York, NY: Pergamon Press, 1981.
28. Korb, C.L. and C.Y. Weng. "The Theory and Correction of Finite Laser Bandwidth Effects in DIAL Experiments," (abstract) in Eleventh International Laser Radar Conference, NASA Conference Publication 2228, June 1982.
29. Douglas-Hamilton, D.H. et al. Carbon Dioxide Electric Discharge Laser Kinetics Handbook. AFWL-TR-74-216. Kirtland AFB, New Mexico: USAF Weapons Laboratory, April 1975. (AD-A008-650)
30. Kruse, P.W. "Optical and Infrared Detectors," in Topics in Applied Physics, Volume 19, edited by R.J. Keyes. Berlin, Heidelberg, New York: Springer Verlag, 1980.
31. Kingston, R.H. Detection of Optical and Infrared Radiation, New York, NY: Springer Verlag, 1978.
32. Pivovonsky, M. and M.R. Nagel. Tables of Blackbody Radiation Functions, New York, NY: MacMillan Co., 1961.
33. Bell, E.E. et al. "Spectral Radiance of Sky and Terrain at Wavelengths Between 1 and 20 microns," Journal of the Optical Society of America, 50: 1313-1320 (1960).
34. Kildal, Helge and R.L. Byer. "Comparison of Laser Methods for the Remote Detection of Atmospheric Pollutants," Proceedings of the IEEE, 59(12): 1644-1663 (1971).
35. Skolnik, M.I. Radar Handbook. New York, NY: McGraw-Hill Book Co., 1970.
36. Rye, B.J. "Differential Absorption Lidar System Sensitivity With Heterodyne Reception," Applied Optics, 17(24): 3862-3864 (1978).

APPENDICES

Appendix A

CO Line Positions and Line Strengths

| <u>Rot. ID</u> | <u>ν (cm⁻¹)</u> | <u>S_m (cm² mol⁻¹ cm⁻¹)</u> |
|----------------|---|---|
| P(24) | 2041.6668 | 1.618 x 10 ⁻²⁰ |
| P(23) | 2046.2764 | 2.429 x 10 ⁻²⁰ |
| P(22) | 2050.8544 | 3.570 x 10 ⁻²⁰ |
| P(21) | 2055.4007 | 5.140 x 10 ⁻²⁰ |
| P(20) | 2059.9150 | 7.248 x 10 ⁻¹⁹ |
| P(19) | 2064.3973 | 1.001 x 10 ⁻¹⁹ |
| P(18) | 2068.8473 | 1.352 x 10 ⁻¹⁹ |
| P(17) | 2073.2650 | 1.787 x 10 ⁻¹⁹ |
| P(16) | 2077.6501 | 2.311 x 10 ⁻¹⁹ |
| P(15) | 2082.0026 | 2.922 x 10 ⁻¹⁹ |
| P(14) | 2086.3223 | 3.609 x 10 ⁻¹⁹ |
| P(13) | 2090.6091 | 4.353 x 10 ⁻¹⁹ |
| P(12) | 2094.8627 | 5.123 x 10 ⁻¹⁹ |
| P(11) | 2099.0831 | 5.877 x 10 ⁻¹⁹ |
| P(10) | 2103.2701 | 6.561 x 10 ⁻¹⁹ |
| P(9) | 2107.4236 | 7.118 x 10 ⁻¹⁹ |
| P(8) | 2111.5434 | 7.486 x 10 ⁻¹⁹ |
| P(7) | 2115.6294 | 7.607 x 10 ⁻¹⁹ |
| P(6) | 2119.6814 | 7.431 x 10 ⁻¹⁹ |
| P(5) | 2123.6992 | 6.927 x 10 ⁻¹⁹ |
| P(4) | 2127.6828 | 6.084 x 10 ⁻¹⁹ |

| | | |
|-------------|-----------|-------------------------|
| P(3) | 2131.6320 | 4.917×10^{-19} |
| P(2) | 2135.5466 | 3.467×10^{-19} |
| P(1) | 2139.4265 | 1.800×10^{-19} |
| Band Center | 2143.2715 | - |
| R(0) | 2147.0815 | 1.834×10^{-19} |
| R(1) | 2150.8564 | 3.599×10^{-19} |
| R(2) | 2154.5960 | 5.201×10^{-19} |
| R(3) | 2158.3001 | 6.557×10^{-19} |
| R(4) | 2161.9686 | 7.606×10^{-19} |
| R(5) | 2165.6014 | 8.313×10^{-19} |
| R(6) | 2169.1983 | 8.670×10^{-19} |
| R(7) | 2172.7592 | 8.693×10^{-19} |
| R(8) | 2176.2839 | 8.422×10^{-19} |
| R(9) | 2179.7723 | 7.909×10^{-19} |
| R(10) | 2183.2242 | 7.218×10^{-19} |
| R(11) | 2186.6394 | 6.411×10^{-19} |
| R(12) | 2190.0179 | 5.550×10^{-19} |
| R(13) | 2193.3595 | 4.688×10^{-19} |
| R(14) | 2196.6641 | 3.867×10^{-19} |
| R(15) | 2199.9314 | 3.116×10^{-19} |
| R(16) | 2203.1614 | 2.456×10^{-19} |
| R(17) | 2206.3539 | 1.892×10^{-19} |
| R(18) | 2209.5087 | 1.427×10^{-19} |
| R(19) | 2212.6257 | 1.053×10^{-19} |
| R(20) | 2215.7048 | 7.610×10^{-20} |

| | | |
|-------|-----------|-------------------------|
| R(21) | 2218.7459 | 5.385×10^{-20} |
| R(22) | 2221.7487 | 3.732×10^{-20} |
| R(23) | 2224.7131 | 2.534×10^{-20} |
| R(24) | 2227.6390 | 1.686×10^{-20} |

Appendix B

Atmospheric Parameters

| <u>h(km)</u> | <u>T(°K)</u> | <u>P/P_s</u> | <u>N_{TOT}(cm⁻³)</u> | <u>N_{CO}(cm⁻³)</u> |
|--------------|--------------|------------------------|---|--|
| 0 | 296.0 | 1.0000 | 2.547 x 10 ¹⁹ | 1.885 x 10 ¹² |
| 1 | 281.7 | 0.8870 | 2.311 x 10 ¹⁹ | 1.710 x 10 ¹² |
| 2 | 275.2 | 0.7846 | 2.093 x 10 ¹⁹ | 1.549 x 10 ¹² |
| 3 | 268.7 | 0.6920 | 1.891 x 10 ¹⁹ | 1.399 x 10 ¹² |
| 4 | 262.2 | 0.6085 | 1.704 x 10 ¹⁹ | 1.261 x 10 ¹² |
| 5 | 255.7 | 0.5334 | 1.531 x 10 ¹⁹ | 1.133 x 10 ¹² |
| 6 | 249.2 | 0.4660 | 1.373 x 10 ¹⁹ | 1.016 x 10 ¹² |
| 7 | 242.7 | 0.4057 | 1.227 x 10 ¹⁹ | 9.078 x 10 ¹¹ |
| 8 | 236.2 | 0.3519 | 1.093 x 10 ¹⁹ | 8.087 x 10 ¹¹ |
| 9 | 229.7 | 0.3040 | 9.711 x 10 ¹⁸ | 7.185 x 10 ¹¹ |
| 10 | 223.3 | 0.2615 | 8.598 x 10 ¹⁸ | 6.362 x 10 ¹¹ |
| 11 | 216.8 | 0.2240 | 7.585 x 10 ¹⁸ | 5.612 x 10 ¹¹ |
| 12 | 216.7 | 0.1915 | 6.486 x 10 ¹⁸ | 4.799 x 10 ¹¹ |
| 13 | 216.7 | 0.1636 | 5.543 x 10 ¹⁸ | 4.101 x 10 ¹¹ |
| 14 | 216.7 | 0.1399 | 4.738 x 10 ¹⁸ | 3.506 x 10 ¹¹ |
| 15 | 216.7 | 0.1195 | 4.049 x 10 ¹⁸ | 2.996 x 10 ¹¹ |
| 16 | 216.7 | 0.1022 | 3.461 x 10 ¹⁸ | 2.561 x 10 ¹¹ |
| 17 | 216.7 | 0.08734 | 2.959 x 10 ¹⁸ | 2.189 x 10 ¹¹ |
| 18 | 216.7 | 0.07466 | 2.529 x 10 ¹⁸ | 1.871 x 10 ¹¹ |
| 19 | 216.7 | 0.06383 | 2.162 x 10 ¹⁸ | 1.600 x 10 ¹¹ |
| 20 | 216.7 | 0.05457 | 1.849 x 10 ¹⁸ | 1.368 x 10 ¹¹ |

| | | | | |
|----|-------|---------|------------------------|------------------------|
| 21 | 217.6 | 0.04667 | 1.574×10^{18} | 1.165×10^{11} |
| 22 | 218.6 | 0.03995 | 1.341×10^{18} | 9.922×10^{10} |
| 23 | 219.6 | 0.03422 | 1.144×10^{18} | 8.464×10^{10} |
| 24 | 220.6 | 0.02933 | 9.759×10^{17} | 7.221×10^{10} |
| 25 | 221.5 | 0.02516 | 8.334×10^{17} | 6.166×10^{10} |
| 26 | 222.5 | 0.02160 | 7.123×10^{17} | 5.270×10^{10} |
| 27 | 223.5 | 0.01855 | 6.092×10^{17} | 4.507×10^{10} |
| 28 | 224.5 | 0.01595 | 5.214×10^{17} | 3.858×10^{10} |
| 29 | 225.5 | 0.01372 | 4.466×10^{17} | 3.304×10^{10} |
| 30 | 226.5 | 0.01181 | 3.828×10^{17} | 2.832×10^{10} |

Appendix C

Aerosol Extinction Coefficients for Clear Atmosphere

| h (km) | $\epsilon_{\text{aerosol}} (\text{km}^{-1})$ absorption | $\epsilon_{\text{aerosol}} (\text{km}^{-1})$ scattering | $\epsilon_M (\text{km}^{-1})$ |
|--------|--|--|-------------------------------|
| 0 | 1.40×10^{-2} | 1.44×10^{-2} | 2.84×10^{-2} |
| 1 | 9.31×10^{-3} | 9.54×10^{-3} | 1.89×10^{-2} |
| 2 | 4.05×10^{-3} | 4.17×10^{-3} | 8.22×10^{-3} |
| 3 | 1.73×10^{-3} | 1.78×10^{-3} | 3.51×10^{-3} |
| 4 | 8.14×10^{-4} | 8.38×10^{-4} | 1.65×10^{-3} |
| 5 | 5.13×10^{-4} | 5.29×10^{-4} | 1.04×10^{-3} |
| 6 | 3.74×10^{-4} | 3.85×10^{-4} | 7.59×10^{-4} |
| 7 | 3.03×10^{-4} | 3.12×10^{-4} | 6.15×10^{-4} |
| 8 | 2.97×10^{-4} | 3.06×10^{-4} | 6.03×10^{-4} |
| 9 | 2.95×10^{-4} | 3.04×10^{-4} | 5.99×10^{-4} |
| 10 | 2.85×10^{-4} | 2.93×10^{-4} | 5.78×10^{-4} |
| 11 | 2.72×10^{-4} | 2.81×10^{-4} | 5.53×10^{-4} |
| 12 | 2.70×10^{-4} | 2.78×10^{-4} | 5.48×10^{-4} |
| 13 | 2.66×10^{-4} | 2.74×10^{-4} | 5.40×10^{-4} |
| 14 | 2.54×10^{-4} | 2.61×10^{-4} | 5.15×10^{-4} |
| 15 | 2.43×10^{-4} | 2.50×10^{-4} | 4.93×10^{-4} |
| 16 | 2.30×10^{-4} | 2.36×10^{-4} | 4.66×10^{-4} |
| 17 | 2.23×10^{-4} | 2.29×10^{-4} | 4.52×10^{-4} |
| 18 | 2.17×10^{-4} | 2.24×10^{-4} | 4.41×10^{-4} |
| 19 | 1.97×10^{-4} | 2.02×10^{-4} | 3.99×10^{-4} |
| 20 | 1.54×10^{-4} | 1.59×10^{-4} | 3.13×10^{-4} |

| | | | |
|----|-----------------------|-----------------------|-----------------------|
| 21 | 1.13×10^{-4} | 1.16×10^{-4} | 2.29×10^{-4} |
| 22 | 8.32×10^{-5} | 8.57×10^{-5} | 1.69×10^{-4} |
| 23 | 6.31×10^{-5} | 6.50×10^{-5} | 1.28×10^{-4} |
| 24 | 4.92×10^{-5} | 5.07×10^{-5} | 9.99×10^{-5} |
| 25 | 4.02×10^{-5} | 4.14×10^{-5} | 8.16×10^{-5} |
| 26 | 2.02×10^{-5} | 2.08×10^{-5} | 4.10×10^{-5} |
| 27 | 2.02×10^{-5} | 2.08×10^{-5} | 4.10×10^{-5} |
| 28 | 2.02×10^{-5} | 2.08×10^{-5} | 4.10×10^{-5} |
| 29 | 2.02×10^{-5} | 2.08×10^{-5} | 4.10×10^{-5} |
| 30 | 2.02×10^{-5} | 2.08×10^{-5} | 4.10×10^{-5} |

Appendix D

Rayleigh Atmospheric Extinction Coefficient

| h (km) | ϵ_R (km ⁻¹) | h (km) | ϵ_R (km ⁻¹) |
|--------|----------------------------------|--------|----------------------------------|
| 0 | 2.290 x 10 ⁻⁶ | 21 | 1.415 x 10 ⁻⁷ |
| 1 | 2.078 x 10 ⁻⁶ | 22 | 1.206 x 10 ⁻⁷ |
| 2 | 1.882 x 10 ⁻⁶ | 23 | 1.029 x 10 ⁻⁷ |
| 3 | 1.700 x 10 ⁻⁶ | 24 | 8.776 x 10 ⁻⁸ |
| 4 | 1.532 x 10 ⁻⁶ | 25 | 7.494 x 10 ⁻⁸ |
| 5 | 1.377 x 10 ⁻⁶ | 26 | 6.405 x 10 ⁻⁸ |
| 6 | 1.235 x 10 ⁻⁶ | 27 | 5.478 x 10 ⁻⁸ |
| 7 | 1.103 x 10 ⁻⁶ | 28 | 4.689 x 10 ⁻⁸ |
| 8 | 9.829 x 10 ⁻⁷ | 29 | 4.016 x 10 ⁻⁸ |
| 9 | 8.733 x 10 ⁻⁷ | 30 | 3.422 x 10 ⁻⁸ |
| 10 | 7.732 x 10 ⁻⁷ | | |
| 11 | 6.821 x 10 ⁻⁷ | | |
| 12 | 5.833 x 10 ⁻⁷ | | |
| 13 | 4.985 x 10 ⁻⁷ | | |
| 14 | 4.261 x 10 ⁻⁷ | | |
| 15 | 3.641 x 10 ⁻⁷ | | |
| 16 | 3.112 x 10 ⁻⁷ | | |
| 17 | 2.661 x 10 ⁻⁷ | | |
| 18 | 2.274 x 10 ⁻⁷ | | |
| 19 | 1.944 x 10 ⁻⁷ | | |
| 20 | 1.663 x 10 ⁻⁷ | | |

Appendix E

Volumetric Scattering Coefficients

| h (km) | β_R (km ⁻¹ sr ⁻¹) | β_M (km ⁻¹ sr ⁻¹) | β (km ⁻¹ sr ⁻¹) |
|--------|--|--|--|
| 0 | 2.733 x 10 ⁻⁷ | 1.15 x 10 ⁻³ | 1.150 x 10 ⁻³ |
| 1 | 2.480 x 10 ⁻⁷ | 7.59 x 10 ⁻⁴ | 7.592 x 10 ⁻⁴ |
| 2 | 2.246 x 10 ⁻⁷ | 3.32 x 10 ⁻⁴ | 3.322 x 10 ⁻⁴ |
| 3 | 2.029 x 10 ⁻⁷ | 1.42 x 10 ⁻⁴ | 1.422 x 10 ⁻⁴ |
| 4 | 1.829 x 10 ⁻⁷ | 6.67 x 10 ⁻⁵ | 6.688 x 10 ⁻⁵ |
| 5 | 1.644 x 10 ⁻⁷ | 4.21 x 10 ⁻⁵ | 4.226 x 10 ⁻⁵ |
| 6 | 1.474 x 10 ⁻⁷ | 3.06 x 10 ⁻⁵ | 3.075 x 10 ⁻⁵ |
| 7 | 1.317 x 10 ⁻⁷ | 2.48 x 10 ⁻⁵ | 2.493 x 10 ⁻⁵ |
| 8 | 1.173 x 10 ⁻⁷ | 2.44 x 10 ⁻⁵ | 2.452 x 10 ⁻⁵ |
| 9 | 1.042 x 10 ⁻⁷ | 2.42 x 10 ⁻⁵ | 2.430 x 10 ⁻⁵ |
| 10 | 9.229 x 10 ⁻⁸ | 2.33 x 10 ⁻⁵ | 2.339 x 10 ⁻⁵ |
| 11 | 8.142 x 10 ⁻⁸ | 2.24 x 10 ⁻⁵ | 2.248 x 10 ⁻⁵ |
| 12 | 6.963 x 10 ⁻⁸ | 2.21 x 10 ⁻⁵ | 2.217 x 10 ⁻⁵ |
| 13 | 5.950 x 10 ⁻⁸ | 2.18 x 10 ⁻⁵ | 2.186 x 10 ⁻⁵ |
| 14 | 5.086 x 10 ⁻⁸ | 2.08 x 10 ⁻⁵ | 2.085 x 10 ⁻⁵ |
| 15 | 4.346 x 10 ⁻⁸ | 1.99 x 10 ⁻⁵ | 1.994 x 10 ⁻⁵ |
| 16 | 3.715 x 10 ⁻⁸ | 1.88 x 10 ⁻⁵ | 1.884 x 10 ⁻⁵ |
| 17 | 3.176 x 10 ⁻⁸ | 1.82 x 10 ⁻⁵ | 1.823 x 10 ⁻⁵ |
| 18 | 2.714 x 10 ⁻⁸ | 1.78 x 10 ⁻⁵ | 1.783 x 10 ⁻⁵ |
| 19 | 2.320 x 10 ⁻⁸ | 1.61 x 10 ⁻⁵ | 1.612 x 10 ⁻⁵ |
| 20 | 1.985 x 10 ⁻⁸ | 1.27 x 10 ⁻⁵ | 1.272 x 10 ⁻⁵ |

| | | | |
|----|------------------------|-----------------------|------------------------|
| 21 | 1.689×10^{-8} | 9.23×10^{-6} | 9.247×10^{-6} |
| 22 | 1.400×10^{-8} | 6.82×10^{-6} | 6.834×10^{-6} |
| 23 | 1.228×10^{-8} | 5.17×10^{-6} | 5.182×10^{-6} |
| 24 | 1.048×10^{-8} | 4.03×10^{-6} | 4.040×10^{-6} |
| 25 | 8.945×10^{-9} | 3.29×10^{-6} | 3.299×10^{-6} |
| 26 | 7.645×10^{-9} | 1.66×10^{-6} | 1.668×10^{-6} |
| 27 | 6.539×10^{-9} | 1.66×10^{-6} | 1.667×10^{-6} |
| 28 | 5.597×10^{-9} | 1.66×10^{-6} | 1.666×10^{-6} |
| 29 | 4.794×10^{-9} | 1.66×10^{-6} | 1.665×10^{-6} |
| 30 | 4.109×10^{-9} | 1.66×10^{-6} | 1.664×10^{-6} |

Appendix F

Absorption Cross-Section of CO Lines at Sea-Level

| <u>Rot. ID</u> | <u>ν_0 (cm⁻¹)</u> | <u>σ_{co} (cm²)</u> |
|----------------|---|--|
| P(10) | 2103.2701 | 5.547 x 10 ⁻²⁴ |
| P(9) | 2107.4236 | 7.125 x 10 ⁻²⁴ |
| P(8) | 2111.5434 | 8.995 x 10 ⁻²⁴ |
| P(7) | 2115.6294 | 1.116 x 10 ⁻²³ |
| P(6) | 2119.6814 | 1.358 x 10 ⁻²³ |
| P(5) | 2123.6992 | 1.616 x 10 ⁻²³ |
| P(4) | 2127.6828 | 1.870 x 10 ⁻²³ |
| P(3) | 2131.6320 | 2.076 x 10 ⁻²³ |
| P(2) | 2135.5466 | 2.127 x 10 ⁻²³ |
| P(1) | 2139.4265 | 1.741 x 10 ⁻²³ |
| R(0) | 2147.0815 | 7.219 x 10 ⁻²³ |
| R(1) | 2150.8564 | 5.705 x 10 ⁻²² |
| R(2) | 2154.5960 | - |
| R(3) | 2158.3001 | 1.070 x 10 ⁻²¹ |
| R(4) | 2161.9686 | 3.125 x 10 ⁻²² |
| R(5) | 2165.6014 | 1.532 x 10 ⁻²² |
| R(6) | 2169.1983 | 9.071 x 10 ⁻²³ |
| R(7) | 2172.7592 | 5.877 x 10 ⁻²³ |
| R(8) | 2176.2839 | 3.993 x 10 ⁻²³ |
| R(9) | 2179.7723 | 2.782 x 10 ⁻²³ |
| R(10) | 2183.2242 | 1.964 x 10 ⁻²³ |

| | | |
|-------|-----------|-------------------------|
| R(11) | 2186.6394 | 1.392×10^{-23} |
| R(12) | 2190.0179 | 9.861×10^{-24} |
| R(13) | 2193.3595 | 6.955×10^{-24} |
| R(14) | 2196.6641 | 4.871×10^{-24} |
| R(15) | 2199.9314 | 3.379×10^{-24} |

TOTAL $\nabla_{co-} = 2.595 \times 10^{-21}$

Appendix G

Absorption Cross-Section and Atmospheric Extinction Coefficient of CO

| <u>h (km)</u> | <u>σ_{co-} (cm²)</u> | <u>ϵ_{co-} (km⁻¹)</u> |
|---------------|---|--|
| 0 | 2.595 x 10 ⁻²¹ | 4.892 x 10 ⁻⁴ |
| 1 | 1.888 x 10 ⁻²¹ | 3.228 x 10 ⁻⁴ |
| 2 | 1.513 x 10 ⁻²¹ | 2.344 x 10 ⁻⁴ |
| 3 | 1.203 x 10 ⁻²¹ | 1.683 x 10 ⁻⁴ |
| 4 | 9.478 x 10 ⁻²² | 1.195 x 10 ⁻⁴ |
| 5 | 7.395 x 10 ⁻²² | 8.379 x 10 ⁻⁵ |
| 6 | 5.710 x 10 ⁻²² | 5.801 x 10 ⁻⁵ |
| 7 | 4.971 x 10 ⁻²² | 4.513 x 10 ⁻⁵ |
| 8 | 3.289 x 10 ⁻²² | 2.660 x 10 ⁻⁵ |
| 9 | 2.449 x 10 ⁻²² | 1.760 x 10 ⁻⁵ |
| 10 | 1.803 x 10 ⁻²² | 1.147 x 10 ⁻⁵ |
| 11 | 1.304 x 10 ⁻²² | 7.318 x 10 ⁻⁶ |
| 12 | 1.112 x 10 ⁻²² | 5.336 x 10 ⁻⁶ |
| 13 | 9.497 x 10 ⁻²³ | 3.895 x 10 ⁻⁶ |
| 14 | 8.121 x 10 ⁻²³ | 2.847 x 10 ⁻⁶ |
| 15 | 6.937 x 10 ⁻²³ | 2.078 x 10 ⁻⁶ |
| 16 | 5.933 x 10 ⁻²³ | 1.519 x 10 ⁻⁶ |
| 17 | 5.070 x 10 ⁻²³ | 1.110 x 10 ⁻⁶ |
| 18 | 4.334 x 10 ⁻²³ | 8.109 x 10 ⁻⁷ |
| 19 | 3.705 x 10 ⁻²³ | 5.928 x 10 ⁻⁷ |
| 20 | 3.168 x 10 ⁻²³ | 4.334 x 10 ⁻⁷ |

| | | |
|----|-------------------------|------------------------|
| 21 | 2.775×10^{-23} | 3.233×10^{-7} |
| 22 | 2.440×10^{-23} | 2.421×10^{-7} |
| 23 | 2.145×10^{-23} | 1.816×10^{-7} |
| 24 | 1.887×10^{-23} | 1.363×10^{-7} |
| 25 | 1.657×10^{-23} | 1.022×10^{-7} |
| 26 | 1.459×10^{-23} | 7.689×10^{-8} |
| 27 | 1.285×10^{-23} | 5.791×10^{-8} |
| 28 | 1.133×10^{-23} | 4.371×10^{-8} |
| 29 | 9.990×10^{-24} | 3.301×10^{-8} |
| 30 | 8.812×10^{-24} | 2.496×10^{-8} |

Appendix H

Absorption Cross-Section of Water-Vapor at Sea-Level

| ν_0 (cm ⁻¹) | S_m (cm ⁻¹ mol ⁻¹ cm ²) | σ_{H_2O} (cm ²) |
|-----------------------------|---|------------------------------------|
| 2141.508 | 0.235 x 10 ⁻²⁵ | 1.395 x 10 ⁻³⁰ |
| 2141.519 | 0.145 x 10 ⁻²³ | 8.625 x 10 ⁻²⁹ |
| 2142.246 | 0.247 x 10 ⁻²³ | 1.647 x 10 ⁻²⁸ |
| 2142.301 | 0.336 x 10 ⁻²⁴ | 2.261 x 10 ⁻²⁹ |
| 2142.495 | 0.228 x 10 ⁻²⁵ | 1.584 x 10 ⁻³⁰ |
| 2143.369 | 0.129 x 10 ⁻²⁵ | 1.041 x 10 ⁻³⁰ |
| 2143.982 | 0.162 x 10 ⁻²⁵ | 1.462 x 10 ⁻³⁰ |
| 2144.708 | 0.101 x 10 ⁻²³ | 1.050 x 10 ⁻²⁸ |
| 2144.808 | 0.742 x 10 ⁻²³ | 7.874 x 10 ⁻²⁸ |
| 2145.468 | 0.579 x 10 ⁻²² | 7.064 x 10 ⁻²⁷ |
| 2145.639 | 0.366 x 10 ⁻²⁵ | 4.637 x 10 ⁻³⁰ |
| 2145.678 | 0.534 x 10 ⁻²³ | 6.825 x 10 ⁻²⁸ |
| 2146.727 | 0.157 x 10 ⁻²⁵ | 2.577 x 10 ⁻³⁰ |
| 2147.337 | 0.215 x 10 ⁻²⁵ | 4.146 x 10 ⁻³⁰ |
| 2147.406 | 0.304 x 10 ⁻²² | 5.975 x 10 ⁻²⁷ |
| 2148.187 | 0.368 x 10 ⁻²³ | 9.100 x 10 ⁻²⁸ |
| 2148.342 | 0.448 x 10 ⁻²³ | 1.163 x 10 ⁻²⁷ |
| 2148.479 | 0.208 x 10 ⁻²⁴ | 5.645 x 10 ⁻²⁹ |
| 2148.831 | 0.130 x 10 ⁻²⁴ | 3.972 x 10 ⁻²⁹ |
| 2148.962 | 0.726 x 10 ⁻²⁵ | 2.322 x 10 ⁻²⁹ |
| 2149.130 | 0.103 x 10 ⁻²³ | 3.500 x 10 ⁻²⁸ |
| 2149.620 | 0.561 x 10 ⁻²⁵ | 2.299 x 10 ⁻²⁹ |

| | | |
|----------|-------------------------|-------------------------|
| 2151.194 | 0.563×10^{-23} | 4.928×10^{-27} |
| 2151.423 | 0.438×10^{-25} | 4.406×10^{-29} |
| 2151.528 | 0.219×10^{-25} | 2.356×10^{-29} |
| 2151.529 | 0.656×10^{-25} | 7.061×10^{-29} |
| 2152.559 | 0.451×10^{-22} | 1.097×10^{-25} |
| 2152.773 | 0.503×10^{-25} | 1.526×10^{-28} |
| 2152.861 | 0.168×10^{-25} | 5.624×10^{-29} |
| 2152.922 | 0.113×10^{-25} | 4.062×10^{-29} |
| 2153.241 | 0.189×10^{-25} | 1.034×10^{-28} |
| 2153.537 | 0.366×10^{-25} | 3.265×10^{-28} |
| 2154.056 | 0.981×10^{-25} | 3.304×10^{-27} |
| 2154.355 | 0.299×10^{-24} | 4.794×10^{-26} |
| 2154.710 | 0.488×10^{-23} | 4.125×10^{-24} |
| 2155.000 | 0.101×10^{-23} | 6.551×10^{-26} |
| 2155.217 | 0.152×10^{-25} | 4.122×10^{-28} |
| 2155.295 | 0.908×10^{-25} | 1.938×10^{-27} |
| 2156.565 | 0.107×10^{-22} | 2.836×10^{-26} |
| 2156.636 | 0.582×10^{-24} | 1.437×10^{-27} |
| 2157.454 | 0.108×10^{-24} | 1.355×10^{-28} |
| 2158.105 | 0.127×10^{-23} | 1.056×10^{-27} |
| 2159.842 | 0.170×10^{-25} | 6.313×10^{-30} |
| 2160.006 | 0.165×10^{-23} | 5.761×10^{-28} |
| 2160.263 | 0.557×10^{-25} | 1.772×10^{-29} |
| 2160.697 | 0.429×10^{-23} | 1.177×10^{-27} |
| 2161.427 | 0.140×10^{-25} | 3.064×10^{-30} |
| 2161.726 | 0.253×10^{-22} | 5.082×10^{-27} |

| | | |
|----------|-------------------------|-------------------------|
| 2161.727 | 0.759×10^{-22} | 1.524×10^{-26} |
| 2162.012 | 0.195×10^{-23} | 3.620×10^{-28} |
| 2162.147 | 0.205×10^{-25} | 3.671×10^{-30} |
| 2162.891 | 0.810×10^{-23} | 1.202×10^{-27} |
| 2163.430 | 0.242×10^{-22} | 3.165×10^{-27} |
| 2165.223 | 0.110×10^{-23} | 9.938×10^{-29} |
| 2166.112 | 0.472×10^{-24} | 3.631×10^{-29} |
| 2166.380 | 0.117×10^{-25} | 8.595×10^{-31} |
| 2167.346 | 0.378×10^{-23} | 2.372×10^{-28} |
| 2167.771 | 0.310×10^{-24} | 1.822×10^{-29} |

TOTAL $\nabla_{H_2O} = 4.435 \times 10^{-24}$

Appendix I

Atmospheric Extinction Coefficient of Water-Vapor

| <u>h (km)</u> | | <u>N_{H₂O} (cm⁻³)</u> | <u>σ_{N₂O} (cm²)</u> | <u>ε_{N₂O} (km⁻¹)</u> |
|---------------|---|---|--|---|
| 0 | | 1.919 x 10 ¹⁷ | 4.435 x 10 ⁻²⁴ | 8.511 x 10 ⁻² |
| 1 | | 1.375 x 10 ¹⁷ | 2.703 x 10 ⁻²⁴ | 3.717 x 10 ⁻² |
| 2 | | 9.567 x 10 ¹⁶ | 1.988 x 10 ⁻²⁴ | 1.902 x 10 ⁻² |
| 3 | * | 6.521 x 10 ¹⁶ | 1.443 x 10 ⁻²⁴ | 9.410 x 10 ⁻³ |
| 4 | | 3.474 x 10 ¹⁶ | 1.034 x 10 ⁻²⁴ | 3.592 x 10 ⁻³ |
| 5 | * | 2.349 x 10 ¹⁶ | 7.297 x 10 ⁻²⁵ | 1.714 x 10 ⁻³ |
| 6 | | 1.223 x 10 ¹⁶ | 5.071 x 10 ⁻²⁵ | 6.202 x 10 ⁻⁴ |
| 7 | * | 8.013 x 10 ¹⁵ | 3.466 x 10 ⁻²⁵ | 2.777 x 10 ⁻⁴ |
| 8 | | 3.796 x 10 ¹⁵ | 2.326 x 10 ⁻²⁵ | 8.829 x 10 ⁻⁵ |
| 9 | * | 2.197 x 10 ¹⁵ | 1.531 x 10 ⁻²⁵ | 3.364 x 10 ⁻⁵ |
| 10 | | 5.972 x 10 ¹⁴ | 9.905 x 10 ⁻²⁶ | 5.915 x 10 ⁻⁶ |
| 11 | * | 3.575 x 10 ¹⁴ | 6.237 x 10 ⁻²⁶ | 2.230 x 10 ⁻⁶ |
| 12 | | 1.178 x 10 ¹⁴ | 5.306 x 10 ⁻²⁶ | 6.250 x 10 ⁻⁷ |
| 13 | * | 7.147 x 10 ¹³ | 4.533 x 10 ⁻²⁶ | 3.240 x 10 ⁻⁷ |
| 14 | | 2.514 x 10 ¹³ | 3.877 x 10 ⁻²⁶ | 9.747 x 10 ⁻⁸ |
| 15 | * | 2.175 x 10 ¹³ | 3.311 x 10 ⁻²⁶ | 7.201 x 10 ⁻⁸ |
| 16 | | 1.836 x 10 ¹³ | 2.832 x 10 ⁻²⁶ | 5.200 x 10 ⁻⁸ |
| 17 | * | 1.589 x 10 ¹³ | 2.420 x 10 ⁻²⁶ | 3.845 x 10 ⁻⁸ |
| 18 | | 1.342 x 10 ¹³ | 2.069 x 10 ⁻²⁶ | 2.777 x 10 ⁻⁸ |
| 19 | * | 1.340 x 10 ¹³ | 1.769 x 10 ⁻²⁶ | 2.370 x 10 ⁻⁸ |
| 20 | | 1.338 x 10 ¹³ | 1.512 x 10 ⁻²⁶ | 2.023 x 10 ⁻⁸ |

* Indicates a linearly interpolated value of number density

| | | | | |
|----|---|------------------------|-------------------------|------------------------|
| 21 | * | 1.445×10^{13} | 1.351×10^{-26} | 1.952×10^{-8} |
| 22 | | 1.552×10^{13} | 1.214×10^{-26} | 1.884×10^{-8} |
| 23 | * | 1.686×10^{13} | 1.091×10^{-26} | 1.839×10^{-8} |
| 24 | | 1.820×10^{13} | 9.799×10^{-27} | 1.783×10^{-8} |
| 25 | * | 1.975×10^{13} | 8.768×10^{-27} | 1.732×10^{-8} |
| 26 | | 2.130×10^{13} | 7.885×10^{-27} | 1.680×10^{-8} |
| 27 | * | 1.828×10^{13} | 7.091×10^{-27} | 1.296×10^{-8} |
| 28 | | 1.526×10^{13} | 6.381×10^{-27} | 9.737×10^{-9} |
| 29 | * | 1.305×10^{13} | 5.742×10^{-27} | 7.493×10^{-9} |
| 30 | | 1.083×10^{13} | 5.169×10^{-27} | 5.598×10^{-9} |

* Indicates a linearly interpolated value of number density

Appendix J

Atmospheric Transmission at 2154.6050 cm⁻¹

| <u>h (km)</u> | <u>$T_A^2(R)$</u> | <u>T_A^2 / R</u> |
|---------------|------------------------------|-------------------------------|
| 0 | 0.7961 | 0.6322 |
| 1 | 0.8933 | 0.7941 |
| 2 | 0.9465 | 0.8890 |
| 3 | 0.9742 | 0.9392 |
| 4 | 0.9893 | 0.9641 |
| 5 | 0.9943 | 0.9745 |
| 6 | 0.9971 | 0.9801 |
| 7 | 0.9981 | 0.9829 |
| 8 | 0.9986 | 0.9848 |
| 9 | 0.9987 | 0.9862 |
| 10 | 0.9988 | 0.9875 |
| 11 | 0.9989 | 0.9887 |
| 12 | 0.9989 | 0.9897 |
| 13 | 0.9989 | 0.9908 |
| 14 | 0.9990 | 0.9919 |
| 15 | 0.9990 | 0.9929 |
| 16 | 0.9991 | 0.9939 |
| 17 | 0.9991 | 0.9948 |
| 18 | 0.9991 | 0.9957 |
| 19 | 0.9992 | 0.9966 |
| 20 | 0.9994 | 0.9974 |

| | | |
|----|--------|--------|
| 21 | 0.9995 | 0.9980 |
| 22 | 0.9997 | 0.9985 |
| 23 | 0.9997 | 0.9988 |
| 24 | 0.9998 | 0.9991 |
| 25 | 0.9998 | 0.9993 |
| 26 | 0.9999 | 0.9995 |
| 27 | 0.9999 | 0.9996 |
| 28 | 0.9999 | 0.9997 |
| 29 | 0.9999 | 0.9998 |
| 30 | 0.9999 | 0.9999 |

Appendix K

Absorption Cross-Section of CO R(2) Line at 2154.6050 cm⁻¹

| <u>h (km)</u> | <u>S_m (cm⁻¹mol⁻¹cm²)</u> | <u>α (cm⁻¹)</u> | <u>τ_{co} (cm²)</u> |
|---------------|--|----------------------------|--|
| 0 | 5.201 x 10 ⁻¹⁹ | 7.0 x 10 ⁻² | 2.327 x 10 ⁻¹⁸ |
| 1 | 4.173 x 10 ⁻¹⁹ | 6.4 x 10 ⁻² | 2.035 x 10 ⁻¹⁸ |
| 2 | 3.744 x 10 ⁻¹⁹ | 5.7 x 10 ⁻² | 2.040 x 10 ⁻¹⁸ |
| 3 | 3.339 x 10 ⁻¹⁹ | 5.1 x 10 ⁻² | 2.021 x 10 ⁻¹⁸ |
| 4 | 2.960 x 10 ⁻¹⁹ | 4.5 x 10 ⁻² | 2.013 x 10 ⁻¹⁸ |
| 5 | 2.606 x 10 ⁻¹⁹ | 4.0 x 10 ⁻² | 1.974 x 10 ⁻¹⁸ |
| 6 | 2.277 x 10 ⁻¹⁹ | 3.6 x 10 ⁻² | 1.895 x 10 ⁻¹⁸ |
| 7 | 1.975 x 10 ⁻¹⁹ | 3.1 x 10 ⁻² | 1.870 x 10 ⁻¹⁸ |
| 8 | 1.697 x 10 ⁻¹⁹ | 2.8 x 10 ⁻² | 1.749 x 10 ⁻¹⁸ |
| 9 | 1.446 x 10 ⁻¹⁹ | 2.4 x 10 ⁻² | 1.681 x 10 ⁻¹⁸ |
| 10 | 1.222 x 10 ⁻¹⁹ | 2.1 x 10 ⁻² | 1.565 x 10 ⁻¹⁸ |
| 11 | 1.019 x 10 ⁻¹⁹ | 1.8 x 10 ⁻² | 1.442 x 10 ⁻¹⁸ |
| 12 | 1.016 x 10 ⁻¹⁹ | 1.6 x 10 ⁻² | 1.535 x 10 ⁻¹⁸ |
| 13 | 1.016 x 10 ⁻¹⁹ | 1.3 x 10 ⁻² | 1.682 x 10 ⁻¹⁸ |
| 14 | 1.016 x 10 ⁻¹⁹ | 1.1 x 10 ⁻² | 1.761 x 10 ⁻¹⁸ |
| 15 | 1.016 x 10 ⁻¹⁹ | 9.8 x 10 ⁻³ | 1.790 x 10 ⁻¹⁸ |
| 16 | 1.016 x 10 ⁻¹⁹ | 8.4 x 10 ⁻³ | 1.792 x 10 ⁻¹⁸ |
| 17 | 1.016 x 10 ⁻¹⁹ | 7.1 x 10 ⁻³ | 1.747 x 10 ⁻¹⁸ |
| 18 | 1.016 x 10 ⁻¹⁹ | 6.1 x 10 ⁻³ | 1.669 x 10 ⁻¹⁸ |
| 19 | 1.016 x 10 ⁻¹⁹ | 5.2 x 10 ⁻³ | 1.557 x 10 ⁻¹⁸ |
| 20 | 1.016 x 10 ⁻¹⁹ | 4.5 x 10 ⁻³ | 1.437 x 10 ⁻¹⁸ |

| | | | |
|----|-------------------------|----------------------|-------------------------|
| 21 | 1.043×10^{-19} | 3.8×10^{-3} | 1.322×10^{-18} |
| 22 | 1.073×10^{-19} | 3.3×10^{-3} | 1.227×10^{-18} |
| 23 | 1.104×10^{-19} | 2.8×10^{-3} | 1.108×10^{-18} |
| 24 | 1.135×10^{-19} | 2.4×10^{-3} | 9.994×10^{-19} |
| 25 | 1.163×10^{-19} | 2.0×10^{-3} | 8.710×10^{-19} |
| 26 | 1.196×10^{-19} | 1.7×10^{-3} | 7.715×10^{-19} |
| 27 | 1.229×10^{-19} | 1.5×10^{-3} | 7.049×10^{-19} |
| 28 | 1.262×10^{-19} | 1.3×10^{-3} | 6.315×10^{-19} |
| 29 | 1.296×10^{-19} | 1.1×10^{-3} | 5.520×10^{-19} |
| 30 | 1.331×10^{-19} | 9.5×10^{-4} | 4.914×10^{-19} |

Appendix L

Atmospheric Transmission at 2154.6050 cm⁻¹ Due to R(2) Line of CO

| <u>h (km)</u> | <u>$T_{co}^2 (R)$</u> | <u>T_{co}^2 / R</u> |
|---------------|----------------------------------|----------------------------------|
| 0 | 0.4159 | 0.001847 |
| 1 | 0.4986 | 0.004441 |
| 2 | 0.5315 | 0.008907 |
| 3 | 0.5681 | 0.01676 |
| 4 | 0.6019 | 0.02950 |
| 5 | 0.6393 | 0.04901 |
| 6 | 0.6804 | 0.07666 |
| 7 | 0.7121 | 0.1127 |
| 8 | 0.7536 | 0.1582 |
| 9 | 0.7854 | 0.2099 |
| 10 | 0.8194 | 0.2673 |
| 11 | 0.8527 | 0.3262 |
| 12 | 0.8630 | 0.3826 |
| 13 | 0.8711 | 0.4433 |
| 14 | 0.8838 | 0.5089 |
| 15 | 0.8983 | 0.5758 |
| 16 | 0.9123 | 0.6410 |
| 17 | 0.9264 | 0.7026 |
| 18 | 0.9395 | 0.7585 |
| 19 | 0.9514 | 0.8073 |
| 20 | 0.9614 | 0.8485 |

| | | |
|----|--------|--------|
| 21 | 0.9697 | 0.8826 |
| 22 | 0.9759 | 0.9102 |
| 23 | 0.9814 | 0.9327 |
| 24 | 0.9857 | 0.9503 |
| 25 | 0.9893 | 0.9641 |
| 26 | 0.9919 | 0.9746 |
| 27 | 0.9937 | 0.9825 |
| 28 | 0.9951 | 0.9887 |
| 29 | 0.9964 | 0.9936 |
| 30 | 0.9972 | 0.9972 |

Appendix M

Atmospheric Transmission Averaged Over the Laser Line-Width

| h (km) | ∇_{EFF} (cm ²) | $\overline{T_{co}^2}(R)$ | $\overline{T_{co}^2} _R$ |
|--------|-----------------------------------|--------------------------|--------------------------|
| 0 | 1.349 x 10 ⁻¹⁸ | 0.6013 | 0.05030 |
| 1 | 1.154 x 10 ⁻¹⁸ | 0.6739 | 0.08365 |
| 2 | 1.104 x 10 ⁻¹⁸ | 0.7104 | 0.1241 |
| 3 | 1.044 x 10 ⁻¹⁸ | 0.7466 | 0.1747 |
| 4 | 9.852 x 10 ⁻¹⁹ | 0.7800 | 0.2340 |
| 5 | 9.180 x 10 ⁻¹⁹ | 0.8122 | 0.3000 |
| 6 | 8.428 x 10 ⁻¹⁹ | 0.8426 | 0.3694 |
| 7 | 7.765 x 10 ⁻¹⁹ | 0.8685 | 0.4384 |
| 8 | 6.962 x 10 ⁻¹⁹ | 0.8935 | 0.5048 |
| 9 | 6.265 x 10 ⁻¹⁹ | 0.9139 | 0.5650 |
| 10 | 5.535 x 10 ⁻¹⁹ | 0.9320 | 0.6182 |
| 11 | 4.833 x 10 ⁻¹⁹ | 0.9472 | 0.6633 |
| 12 | 4.961 x 10 ⁻¹⁹ | 0.9535 | 0.7003 |
| 13 | 5.168 x 10 ⁻¹⁹ | 0.9585 | 0.7344 |
| 14 | 5.332 x 10 ⁻¹⁹ | 0.9633 | 0.7662 |
| 15 | 5.428 x 10 ⁻¹⁹ | 0.9680 | 0.7954 |
| 16 | 5.545 x 10 ⁻¹⁹ | 0.9720 | 0.8217 |
| 17 | 5.666 x 10 ⁻¹⁹ | 0.9755 | 0.8454 |
| 18 | 5.754 x 10 ⁻¹⁹ | 0.9787 | 0.8666 |
| 19 | 5.835 x 10 ⁻¹⁹ | 0.9815 | 0.8855 |
| 20 | 5.932 x 10 ⁻¹⁹ | 0.9839 | 0.9022 |

| | | | |
|----|-------------------------|--------|--------|
| 21 | 6.138×10^{-19} | 0.9858 | 0.9169 |
| 22 | 6.390×10^{-19} | 0.9874 | 0.9301 |
| 23 | 6.594×10^{-19} | 0.9889 | 0.9420 |
| 24 | 6.819×10^{-19} | 0.9902 | 0.9526 |
| 25 | 7.004×10^{-19} | 0.9914 | 0.9620 |
| 26 | 7.238×10^{-19} | 0.9924 | 0.9704 |
| 27 | 7.458×10^{-19} | 0.9933 | 0.9778 |
| 28 | 7.669×10^{-19} | 0.9941 | 0.9844 |
| 29 | 7.890×10^{-19} | 0.9948 | 0.9902 |
| 30 | 8.140×10^{-19} | 0.9954 | 0.9954 |

Vita

Wesley Robert Hertel was born on 18 June 1948 in Hays, Kansas. He attended high school at St. Joseph's Military Academy where he graduated in 1966. He then attended Ft. Hays Kansas State University for two years prior to his enlistment in the United States Air Force in 1968 as a flight simulator tactics specialist. After a four year term in the Air Force he was employed at General Dynamics, Convair Division, in Ft. Worth Texas for two years as a test analyst at the Air Force Electronic Warfare Evaluation Simulator (AFEWES). He then returned to Ft. Hays Kansas State University where he received the degree of Bachelor of Science in Physics in 1977. In 1978 he began his career in the United States Government as a civilian employee at Wright-Patterson Air Force Base, Foreign Technology Division (FTD). In May 1982, he entered the School of Engineering, Air Force Institute of Technology under the Long Term education program sponsored by FTD.

He is married to the former Margaret Ann Bunnell and they currently reside at 4276 Green Meadows Drive in Enon, Ohio.

UNCLASSIFIED

SECURITY CLASSIFICATION OF THIS PAGE

REPORT DOCUMENTATION PAGE

| | | | | | | |
|---|-------|--|--|---|--|--|
| 1. REPORT SECURITY CLASSIFICATION UNCLASSIFIED | | | 1b. RESTRICTIVE MARKINGS | | | |
| 2. SECURITY CLASSIFICATION AUTHORITY | | | 3. DISTRIBUTION/AVAILABILITY OF REPORT Approved for public release; distribution unlimited | | | |
| 2b. DECLASSIFICATION/DOWNGRADING SCHEDULE | | | 5. MONITORING ORGANIZATION REPORT NUMBER(S) | | | |
| 4. PERFORMING ORGANIZATION REPORT NUMBER(S) AFIT/GEP/PH-83D-4 | | | 5. MONITORING ORGANIZATION REPORT NUMBER(S) | | | |
| 6a. NAME OF PERFORMING ORGANIZATION School of Engineering | | 6b. OFFICE SYMBOL (If applicable) AFIT/ENP | | 7a. NAME OF MONITORING ORGANIZATION | | |
| 6c. ADDRESS (City, State and ZIP Code) Air Force Institute of Technology Wright-Patterson AFB, Ohio 45433 | | | | 7b. ADDRESS (City, State and ZIP Code) | | |
| 8a. NAME OF FUNDING/SPONSORING ORGANIZATION | | 8b. OFFICE SYMBOL (If applicable) | | 9. PROCUREMENT INSTRUMENT IDENTIFICATION NUMBER | | |
| 8c. ADDRESS (City, State and ZIP Code) | | | | 10. SOURCE OF FUNDING NOS. | | |
| 11. TITLE (Include Security Classification) See Box 19 | | | | PROGRAM ELEMENT NO. | | |
| | | | | PROJECT NO. | | |
| | | | | TASK NO. | | |
| | | | | WORK UNIT NO. | | |
| 12. PERSONAL AUTHOR(S) Wesley R. Hertel Civ. GS-12 | | | | | | |
| 13. TYPE OF REPORT MS Thesis | | 13b. TIME COVERED FROM TO | | 14. DATE OF REPORT (Yr., Mo., Day) 1983 December | | |
| | | | | 15. PAGE COUNT 136 | | |
| 16. SUPPLEMENTARY NOTATION Approved for Public Release, IAW AFR 190-17 | | | | | | |
| 17. COSATI CODES | | | 18. SUBJECT TERMS (Continue on reverse if necessary and identify by block number) | | | |
| FIELD | GROUP | SUB. GR. | Differential Absorption Lidar | | | |
| 17 | 05 | | DIAL | | | |
| 04 | 01 | | Atmospheric Carbon Monoxide LIDAR | | | |
| 19. ABSTRACT (Continue on reverse if necessary and identify by block number) | | | | | | |
| Title: Detection of Atmospheric Carbon Monoxide From A Shuttle-Borne Lidar | | | | | | |
| Thesis Chairman: James J. Lange, Major USAF Associate Professor of Engineering Physics | | | | | | |
| Approved for public release IAW AFR 190-17. LYON E. WOLAVER 16 JAN 86 Dean for Research and Professional Development Air Force Institute of Technology (AFIT) Wright-Patterson AFB OH 45433 | | | | | | |
| 20. DISTRIBUTION/AVAILABILITY OF ABSTRACT UNCLASSIFIED/UNLIMITED <input checked="" type="checkbox"/> SAME AS RPT <input type="checkbox"/> DTIC USERS <input type="checkbox"/> | | | 21. ABSTRACT SECURITY CLASSIFICATION UNCLASSIFIED | | | |
| 22a. NAME OF RESPONSIBLE INDIVIDUAL James J. Lange, Major, USAF | | 22b. TELEPHONE NUMBER (Include Area Code) 513-255-4498 | | 22c. OFFICE SYMBOL AFIT/ENP | | |

UNCLASSIFIED

SECURITY CLASSIFICATION OF THIS PAGE

Remote sensing of carbon monoxide from a shuttle-borne differential absorption lidar (DIAL) was investigated. The primary lidar wavelength is in the infrared at 4.64μ and takes advantage of a spectral coincidence between the R(2) line in the fundamental absorption band of CO and the frequency-doubled R(18) emission line of the CO₂ laser. Extinction coefficients for CO, H₂O, Rayleigh, and MIE scattering were determined in order to compute the return signal strength from various altitudes. Direct detection was found to be unsatisfactory, but heterodyne detection was found to be suitable if shotaveraging is used. With heterodyne detection the system was determined to be capable of making accurate measurements of CO in the troposphere, but performance in the stratosphere was found to be marginal.

UNCLASSIFIED

SECURITY CLASSIFICATION OF THIS PAGE

END

FILMED

386

DTIC